**Title**

Biochemical Characterization of Mammalian Formin FHOD3 in Cardiomyocyte Development

**Author**

Valencia, Dylan Andrew

**Publication Date**

2024

UNIVERSITY OF CALIFORNIA

Los Angeles

# Biochemical Characterization of Mammalian Formin FHOD3 in Cardiomyocyte Development

A dissertation submitted in partial satisfaction of the requirements for the degree Doctor of Philosophy in Biochemistry, Molecular, and Structural Biology

by

Dylan Andrew Valencia

2024

# ABSTRACT OF THE DISSERTATION

## Biochemical Characterization of Mammalian Formin FHOD3 in Cardiomyocyte Development

by

Dylan Andrew Valencia
Doctor of Philosophy in Biochemistry, Molecular, and Structural Biology
University of California, Los Angeles, 2024
Professor Margot Elizabeth Quinlan, Co-Chair
Professor Atsushi “Austin” Nakano, Co-Chair

Muscle contractions, among other cellular functions, are driven by highly ordered structures composed of actin and myosin. For cells to properly execute these functions, actin filaments must be specifically organized, assembled, and maintained throughout the cell. The precise timing of actin assembly required for these functions is helped by actin nucleators, such as formins. Formins assemble many actin-based structures through their formin homology (FH) domains, FH1 and FH2. The FH2 domain helps form new filaments in a process called nucleation, while the FH1 domain helps to elongate actin filaments in a processive manner while the FH2 domain “walks” along the growing barbed ends of filaments. The formin homology domain-containing protein (Fhod) family of formins are important for building several contractile actin structures, including sarcomeres in muscle cells and stress fibers in various non-muscle cells. Despite Fhod family formins being required for structures *in vivo*, mammalian Fhods were initially reported to instead inhibit actin assembly *in vitro*. Here, we establish that mammalian formin FHOD3 (both isoforms FHOD3S and FHOD3L) nucleate and elongate actin filaments *in vitro*. Human FHOD3S/L elongate actin filaments quite differently than other formins, where we observe brief, rapid moments of elongation after elongation is paused. We performed rescue experiments for FHOD3L in neonatal rat ventricular myocytes (NRVMs) with mutants that separated its actin assembly activities to better understand whether nucleation or elongation is more important for sarcomere formation. We found that elongation activity by FHOD3L is necessary and sufficient for proper sarcomere formation and maintenance, whereas reducing its nucleation or bundling activity is tolerated in NRVMs. Further, mutations in FHOD3 have been implicated in 1-2% of cases of hypertrophic cardiomyopathy (HCM), a heart disease which results in the thickening of the septal muscle, eventually leading to arrhythmias and heart failure. Interestingly, the likely pathogenic R1386Q mutation for HCM results in a 37% increase in nucleation ability *in vitro*, leading to thinner sarcomeres in NRVM rescue experiments. We establish NRVMs as a model system to observe sarcomere structure and function and to understand which actin assembly activities are most crucial to the formation and maintenance of the sarcomere.

The dissertation of Dylan Andrew Valencia is approved.

Steven Gerard Clarke

Emil Reisler

Atsushi “Austin” Nakano, Co-Chair

Margot Elizabeth Quinlan, Co-Chair

University of California, Los Angeles

2024

I dedicate this dissertation to my mom, Theresa Valencia, and my cousin, Lauren Valencia, who saw me start this arduous journey of the PhD, but did not see me finish. All the unwavering love and support has allowed me to attain my PhD and be able to start discovering and developing cures for cancers and other diseases to help our loved ones live longer, and for that I thank you both from the bottom of my heart.

## Table of Contents

## List of figures

## List of tables

## Acknowledgements

First and foremost, I would like to thank my mentors Dr. Margot Quinlan and Dr. Austin Nakano for their years of mentorship in both my scientific and personal pursuits. Their unwavering support and dedication to training made me feel like a colleague and I have learned much from their guidance. I have learned so much from you two and will carry on those valuable lessons into my future career. I would like to thank my family for all their love and support throughout these past six years and throughout my entire life. They've taught me how to always pursue my dreams in my life and to never give up in doing so, and I sincerely thank them for that.

Thanks to my best friend, Bijan, who has supported me in everything that I do and has always been there for me. Thanks to all my close friends from high school and college: Ryan Chase, Justin Ogihara, Jason Lauckner, Ed Chong, Brian Vollaire, Andrew Romero, Kevin Do, Sara Do, Phillip Chen, Jeanie Garcia, Stella Ho, and Rowan Forrester. I'm so lucky to have met all of you and am grateful for all the support and advice you've given these past six years and beyond.

To my high school AP Biology teacher, Mr. Thomas Velekei, who ignited my passion for biochemistry and molecular biology. I'm so grateful to have had such a wonderful educator as him. The appendix to Chapter 1 is a reprint of Valencia et al, *Curr. Biol.* 2021. I thank Margot again for her help with this primer as principal investigator. Thanks to my former undergraduate researcher, Vicente Velazquez, who cloned, expressed, and purified proteins in our collaborative project with the Steven G. Clarke lab at UCLA with graduate student Troy Lowe, resulting in a manuscript under review in *J. Biol. Chem.*. Related work to this collaborative project is done in Chapter 3.

## Vita

### Education

B.S., Biochemistry and Molecular Biology
June 2018
University of California, Davis

### Research Experience

Graduate Student Researcher July 2018-June 2024
Laboratories of Drs. Margot E. Quinlan and Atsushi "Austin" Nakano
Departments of Chemistry and Biochemistry and Molecular, Cell, and Developmental Biology
University of California, Los Angeles

Graduate Intern- Research & Development May 2022-August 2022
Laboratory of Dr. Paul Hughes
Oncology Department
Amgen, Thousand Oaks

Undergraduate Researcher June 2016-July 2018
Laboratory of Dr. Stephen C. Kowalczykowski
Department of Microbiology and Molecular Genetics
University of California, Davis

Laboratory Assistant September 2015-July 2018
UCDNA Sequencing
Department of Evolution and Ecology
University of California, Davis

Intern June 2014-August 2014
Oak Crest Institute of Science
Pasadena, CA

### Publications

Valencia DA, Quinlan ME. Formins. *Curr. Biol.*, 2021 May 24;31:R517-R522.

Valencia DA, Koeberlein AN, Harui A, Nakano H, Rudas A, Spencer C, Nakano A, Quinlan ME. Human formin FHOD3-mediated elongation is required for sarcomere integrity in cardiomyocytes. Manuscript in preparation.

Lowe TL, Valencia DA, Velazquez VE, Quinlan ME, Clarke, SG. Methylation and phosphorylation of formin homology domain proteins (Fhod1 and Fhod3) by protein arginine methyltransferase 7 (PRMT7) and Rho Kinase (ROCK1). Manuscript under review.

### Abstracts and Presentations

Valencia DA. Determining the role of mammalian formin FHOD3L in cardiomyocyte development. Technical talk. Dissertation Seminar. UCLA, Los Angeles, CA 2024.

Valencia DA, Koeberlein AN, Quinlan ME, and Nakano AN. “Human Formin FHOD3 is Formin’ Sarcomeres Primarily by Elongation.” Poster, 20th Annual Stem Cell Symposium. UCLA, Los Angeles, CA, 2024.

Valencia DA, Koeberlein AN, Quinlan ME, and Nakano AN. “Human Formin FHOD3 is Formin’ Sarcomeres Primarily by Elongation.” Poster, American Society for Cell Biology (ASCB) conference. Boston Convention and Exhibition Center, Boston, M.A. 2023.

Valencia DA, Koeberlein AN, Quinlan ME, and Nakano AN. “Human Formin FHOD3 is Formin’ Sarcomeres Primarily by Elongation.” Poster, Molecular, Cellular, and Developmental Biology Departmental Retreat. Annenberg Community Beach House, Santa Monica, CA 2023.

Valencia DA, Koeberlein AN, Quinlan ME, and Nakano AN. “Is Human Formin FHOD3 Formin’ Sarcomeres Primarily by Nucleation or Elongation?” Poster, Cardiovascular Theme Retreat. UCLA, Los Angeles, CA, 2023.

Valencia DA, Quinlan ME, and Nakano AN. “Determining the Role of Mammalian Formin Homology Domain-Containing 3 (FHOD3) in Cardiomyocytes.” Poster, American Society for Cell Biology (ASCB) conference. Walter E. Washington Convention Center, Washington, D.C. 2022.

Valencia DA, Quinlan ME, and Nakano AN. “Determining the Role of Mammalian Formin, Formin Homology Domain-Containing 3 (FHOD3), in Cardiomyocytes.” Poster, American Society for Cell Biology (ASCB) conference. Online, 2021.

Valencia DA, Quinlan ME, and Nakano AN. “Determining the Role of Mammalian Formin, Formin Homology Domain-Containing 3 (FHOD3), in Cardiomyocytes.” Poster, Molecular, Cellular, and Developmental Biology Departmental Retreat. Annenberg Community Beach House, Santa Monica, CA 2021.

Bailey HM, Valencia DA, Quinlan ME et al.. “Biochemistry of Developmental Biology in the Quinlan Lab.” Poster, Biochemistry, Molecular, and Structural Biology recruitment weekend. UCLA, Los Angeles, CA 2020.

### Awards
Cellular and Molecular Biology Training Grant (2019-2021)
American Society for Cell Biology travel award for U.S. Underrepresented Minorities (September 2023)

### Mentorship
Angela Koeberlein — Winter 2023
Rotation student in Biochemistry, Molecular, and Structural Biology

Jack Scully — Winter 2023
Rotation student in Biochemistry, Molecular, and Structural Biology

Daiana Ahissou — Summer 2021-Spring 2022
Undergraduate

Carolyn Wu — Winter 2021
Rotation student in Biochemistry, Molecular, and Structural Biology

Connor Short — Winter 2021

Rotation student in Biochemistry, Molecular, and Structural Biology

Vicente Velazquez Winter 2020-Fall 2021
Undergraduate

Ananya Kepper Summer 2019
SMC-UCLA / Undergraduate

Teaching
TA – CHEM154 (Biochemical Methods II) Spring 2024
TA – CHEM154 (Biochemical Methods II) Spring 2019
TA – CHEM154 (Biochemical Methods II) Winter 2019

Professional Courses
ASCB, KGI and Manning School of Business Virtual Biotech course July 2020

Service
Volunteer October 2018-2024
California NanoSystems Institute (CNSI) Nanoscience Outreach

Volunteer/Treasurer/President September 2018-2024
Graduate Biochemistry Student Association (gBSA)

# Chapter 1: Introduction

### *Actin cytoskeleton*

Actin is one of the most evolutionarily conserved proteins in eukaryotes and self-assembles into filaments of varying lengths. The spontaneous formation of new actin filaments (F-actin), in a process called nucleation, is both thermodynamically and kinetically unfavorable, and thus occurs very slowly with an initial lag phase due to unstable actin dimers and trimers. However, the addition of a fourth subunit results in a much more stable structure, known as the nucleus (Pollard, 2016). Once an actin filament is nucleated, it will freely elongate at either end if the concentration of free globular actin monomers (G-actin) exceeds 0.16 $\mu$M, the critical concentration for Mg-ATP-actin. Actin filaments can elongate at either end, with the more dynamic barbed end growing approximately ten-fold faster than the pointed end (Pollard, 1986).

Actin filaments can generate and direct forces by polymerizing to push a surface, providing structural rigidity to resist forces, or acting as part of a contractile structure with the help of myosin, such as the sarcomere in striated muscle cells. For the cell to properly carry out these functions, actin filaments must be assembled and disassembled precisely at the correct time and location. Since spontaneous actin assembly is only mildly controlled by kinetics, cells rely on over a hundred actin-binding proteins to control the assembly, organization, and disassembly of each actin-based structure.

Mammals have six closely related actin isoforms that help perform different functions. There are four muscle-specific isoforms and two more widely expressed cytoplasmic isoforms. These six mammalian isoforms are at least 93% identical to each other and up to 98% identical (Perrin & Ervasti, 2010). Despite the strong similarity between actin isoforms, each isoform differs in abundance and function within many different cell types (Müller et al., 2013). For example, cardiomyocytes primarily express $\alpha$-cardiac muscle actin to help form the thin actin filaments within sarcomeres, a highly organized, proteinaceous structure required for contractility (Fenix et al., 2018; Littlefield & Fowler, 2008). In contrast, cytoplasmic $\beta$- and $\gamma$-actin isoforms are widely expressed in many cell types and contribute to the migration abilities of certain cells, such as neutrophils or colon cancer cells (Mitchison & Cramer, 1996; Simiczyjew et al., 2017). Moreover, a fraction of actin-binding proteins, such as actin nucleators, exhibit different affinities for some actin isoforms in various cell types (Herman, 1993; Müller et al., 2013; Perrin & Ervasti, 2010).

### *Formins*

Actin nucleators help with the precise regulation of actin assembly and organization in cells for many different actin-based structures, which ultimately give rise to important cellular processes (Courtemanche, 2018; Valencia, DA, Quinlan, 2021). One class of actin nucleators is known as formins, which are separated into nine distinct classes. Seven of these nine classes are found in humans (Valencia, DA, Quinlan, 2021). Formins are defined by two Formin Homology (FH) domains, the FH1 and FH2 domains. The FH2 domain is central to the formins actin nucleator ability and forms a donut-shaped homodimer. Further, this FH2 domain is highly conserved between species. In addition to aiding in actin nucleation, the FH2 domain also remains processively bound to the barbed end of the actin filament during elongation.

The FH1 domain is located N-terminal to the FH2 domain. The FH1 domain also modulates the elongation rate of actin filaments, but is much less conserved and thus varies in length (Courtemanche, 2018). The FH1 domain is a highly unstructured, proline-rich domain, which helps elongate actin filaments by indirectly binding actin via the actin-monomer binding protein profilin. The widely accepted model for formin-mediated elongation of actin filaments is known as the “capture and delivery” model: the FH1 domain binds (captures) profilin-bound actin and rapidly delivers it to the growing end of the actin filament (Courtemanche, 2018).

Both FH domains are flanked by various regulatory domains that alter overall formin activity. The C-terminal “tail”, or Diaphanous Autoinhibitory Domain (DAD), interacts with actin monomers and polymers via electrostatic interactions, which increases the formins nucleation and processive ability (Gould et al., 2011; Vizcarra et al., 2014). This DAD interacts with the Diaphanous Inhibitory Domain (DID) in the N-terminus of the formin to autoinhibit its function, although the exact mechanism remains unclear (Gould et al., 2011). This autoinhibitory interaction is partially relieved by the binding of a Rho GTPase to the N-terminal GTPase Binding Domain (GBD) (Courtemanche, 2018). In addition to this, some formins dimerize at an N-terminal dimerization domain and how this mechanistically alters formin activity remains unclear.

*FHOD-family formins*

One of the nine classes of formins is known as the Formin HOmology Domain (FHOD)-containing-family of proteins (Campellone & Welch, 2010)(**Fig. 1-1A**). There are two FHOD-family formin genes in mammals, *FHOD1* and *FHOD3*. *FHOD3* encodes two splice isoforms. The longer isoform, FHOD3L, is distinguished from FHOD3S by five additional exons. FHOD1 was initially thought to cap barbed-ends and bundle actin filaments, rather than accelerate actin assembly, in contrast to all other formins studied to date (Schönichen et al., 2013). However, the Quinlan lab showed that FHOD1 is, in fact, a nucleator (Patel et al., 2018). Interestingly, FHOD1 nucleates *Acanthamoeba* actin, but not rabbit skeletal muscle actin, which is one of the first examples of actin isoform specificity (Patel et al., 2018). Similar to the refuted models for FHOD1, *in vitro* biochemistry for

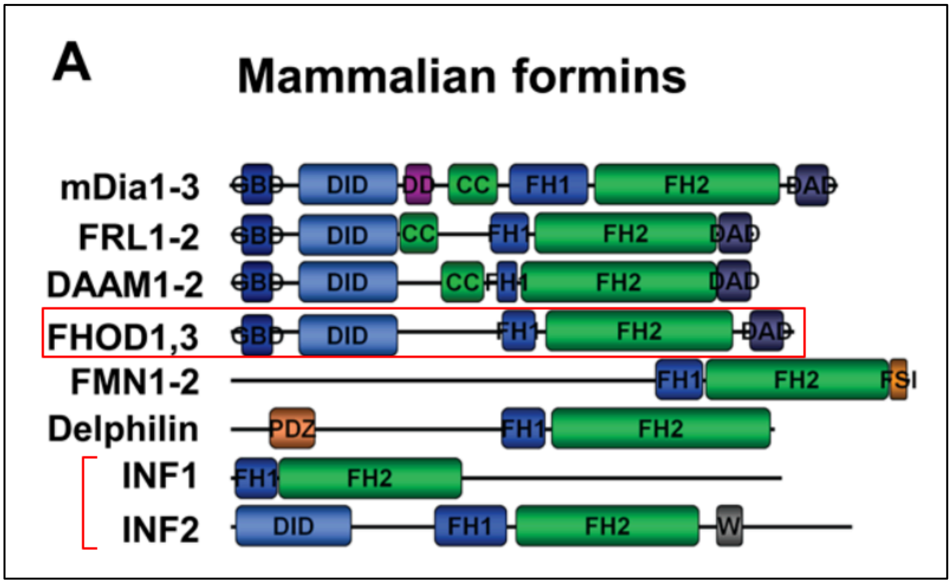

**Figure 1-1** – *Mammalian formin families possess distinct domain organizations*

Modified from Campellone et al. (2010) (**A**) The seven mammalian formin classes share conserved FH1 and FH2 domains for actin assembly along with diverse regulatory motifs. INF family formins are grouped as one class and FHOD1/3 is boxed in red. CC, coiled-coil; DAD, diaphanous autoregulatory domain; DID, diaphanous inhibitory domain; DD, dimerization domain; FH, formin homology; FSI, formin-spire-interaction; GBD, GTPase-binding-domain; PDZ, PSD95-DlgA-ZO1; W, WH2 domain.

FHOD3 continues to be questioned. One group reported that FHOD3 inhibits actin assembly (Taniguchi et al., 2009). However, preliminary data that will be further elaborated on here strongly suggests that both FHOD3S and FHOD3L are potent nucleators. Moreover, all *Drosophila* Fhod formins have been shown to be potent nucleators, but weak elongators (Patel et al., 2018).

### *Cardiomyocyte Mechanobiology*

Within striated muscle cells, such as cardiomyocytes, the sarcomere is a highly proteinaceous structure required for proper contractions. It is well-established that sarcomeres contract by a sliding mechanism (A. F. Huxley & Niedergerke, 1954; H. Huxley & Hanson, 1954; Palmer et al., 2020). The thick myosin filaments, which are anchored to the central M-band, pull on the interdigitated thin actin filaments, which are anchored to the sarcomeric Z-discs that border the sarcomeres (**Fig. 1-2A**). Thus, during what is known as the power stroke, the myosin motors slide towards the Z-discs as they pull on the actin filaments, which shortens the sarcomere and the overall muscle fiber (**Fig.1-2A**) . Conversely, regulatory proteins, such as troponin and tropomyosin that decorate the thin actin filaments, help keep actin and myosin separated from each other during the muscles resting state (Pirani et al., 2006). Further, sarcomere length is tightly controlled by titin, whose N-terminus is bound to the Z-disc, whereas its C-terminus is bound to the central myosin thick filaments (**Fig.1-1A**) (Fürst et al., 1988;

Gautel & Goulding, 1996; Linke et al., 1996; Maruyama et al., 1976). The stability of the highly organized sarcomere is due in part to proximal transcription and translation of sarcomere genes, as evidenced by fluorescent *in situ* hybridization (FISH) and the Sun-tagging system where mRNA localization is nearly identical to the corresponding protein localization (Denes et al., 2021; Lewis et al., 2018).

Three complementary methods to evaluate mechanical changes in cardiomyocytes are measurements of calcium transients, Digital Image Correlation (DIC), and Multi-Electrode Arrays (MEA) (Dunham et al., 2022; Guatimosim et al., 2011; Huebsch et al., 2015; Psaras et al., 2021). During excitation-contraction coupling (ECC) depolarization, calcium channels are opened and lead to calcium-induced calcium release from the sarcoplasmic reticulum (SR) via ryanodine receptor (RyR) channels (Bers, 2001). These dynamic calcium transients are reliable indicators of cardiomyocyte contractility (Ahola et al., 2018). DIC is a

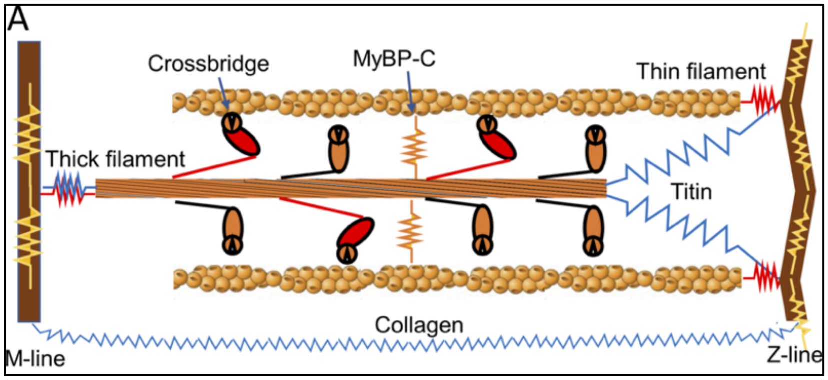

**Figure 1-2** – *Cartoon illustration of the half sarcomere and myosin crossbridges*

Modified from Palmer, et al. (2020). (**A**) Protein connections that span the half sarcomere and are responsible for crossbridge-independent viscoelasticity include most notably titin and collagen (blue). Protein connections responsible for crossbridge-dependent viscoelasticity include myosin and other proteins of the thick and thin filaments and the M- and Z-lines such as actin, α-actinin, etc. (red). Myosin-binding protein C contributes to a transverse stiffness that can play indirect roles in longitudinal viscoelasticity (orange and yellow).

high-resolution, optical approach to measuring displacement of pixels in real-time and in three dimensions, allowing for indirect measurements of contracting cardiomyocytes (Dolan et al., 2018; Nakano et al., 2017). In addition to DIC, other user-friendly imaging softwares have been released that track contractility over time for cardiomyocytes at any developmental stage (Boudaoud et al., 2014; Grune et al., 2019; Sala et al., 2018). Further, the MEA platform enables examination of cardiomyocyte maturation at the electrophysiological level by monitoring their steady and consistent beat signatures over time (Dunham et al., 2022; Zhu et al., 2017).

### *FHOD3 in Cardiomyocyte Development and Disease*

The FHOD-family of formins are important for cell spreading, motility, and sarcomere formation (Fenix et al., 2018; Gasteier et al., 2003; Iskratsch et al., 2013; Schönichen et al., 2013; Taniguchi et al., 2009). FHOD3L is primarily expressed in striated muscle, including cardiomyocytes (Kan-o, Takeya, Taniguchi, et al., 2012). Within cardiomyocytes, FHOD3L localizes to the sarcomeres – its localization within the sarcomere may be developmentally-specific (Fenix et al., 2018; Kan-o, Takeya, Abe, et al., 2012; Taniguchi et al., 2009; Ushijima et al., 2018). In line with this finding, FHOD3L is required for proper sarcomere assembly *de novo* and sarcomere maintenance at the embryonic and perinatal stages of development (Fenix et al., 2018; Kan-o, Takeya, Taniguchi, et al., 2012; Ushijima et al., 2018). Despite this knowledge, the specific actin assembly activities that are necessary or sufficient for these FHOD3L functions in cardiomyocytes are not well understood (Fujimoto et al., 2016; Kan-o, Takeya, Abe, et al., 2012; Taniguchi et al., 2009; Ushijima et al., 2018). Thus, understanding FHOD3 at the biochemical level is essential to clarifying its role *in vivo*.

Both FHOD1 and FHOD3 are involved in cardiomyopathies (Arimura et al., 2013; Ochoa et al., 2018; Perriard et al., 2003). Cardiomyopathies are diseases of the heart muscle that eventually lead to heart failure because of improper blood flow. During dilated cardiomyopathy, FHOD1 expression levels increase, while FHOD3 expression levels decrease, suggesting that the two mammalian formins play distinct roles in cardiac tissue (Perriard et al., 2003). Further, mutations in the *FHOD3* gene have been shown to contribute to 1-2% of cases of hypertrophic cardiomyopathy (HCM) (**Fig.1-3A**) (Ochoa et al., 2018). Some of these mutations are within the FH1 and FH2 domains, but most are primarily in a predicted coiled-coil domain in the N-terminus, suggesting that disrupting the regulation of FHOD3 activity promotes this diseased state (**Fig.1-3A**) (Gould et al., 2011; Ochoa et al., 2018). Further, some of these pathogenic mutations are also confirmed on the Genome Aggregation Database (gnomAD). Interestingly, more newly discovered mutations on gnomAD of uncertain significance in the N-terminal half of FHOD3 appear at splice donor and acceptor sites, suggesting that truncations of FHOD3 from disrupted alternative splicing of mRNA could also lead to this disease. Despite this information, there is currently no data that elucidates the mechanism of how these FHOD3 mutants lead to HCM, whether that is by disrupting the sarcomeres within cardiomyocytes, altering their contractile function, or both. Thus, understanding the biochemistry of FHOD3 mutants implicated in HCM *in vitro* and in cardiomyocytes will better help clinical researchers design therapies against this disease.

### *Elucidation of sarcomere formation by FHOD3*

Cell biologists and biochemists have been attempting to understand the mechanism of sarcomere formation in cardiomyocytes for decades. It was previously reported that FHOD3's actin assembly activity in general is necessary for proper sarcomere formation in neonatal rat ventricular myocytes (NRVMs) (Taniguchi et al., 2009). However, whether nucleation or elongation by FHOD3, or its bundling or capping activities, are more important for this process of sarcomere formation is not currently known. Based on the *in vitro* biochemical activity for human FHOD1 and *Drosophila* Fhod formins, I hypothesized that initial nucleation of actin filaments by FHOD3 is more important for sarcomere formation and maintenance in NRVMs compared to its elongation activity (Patel et al., 2018).

In the Chapter 2 manuscript, rescue experiments in NRVMs were performed with function-separating and HCM-causative FHOD3 mutants to better understand FHOD3's function in sarcomere formation. In Chapter 3, I describe additional work from a collaboration between the Steven Clarke and Quinlan labs to reveal insights into the physiological importance of FHOD3 as a novel substrate for methylation by human protein arginine methyltransferase 7 (PRMT7). Lastly, in Chapter 4, I describe advancements to a new, automated sarcomere measurement program known as sarcApp and compare my manual measurements to those from the program (Neininger-Castro et al., 2023).

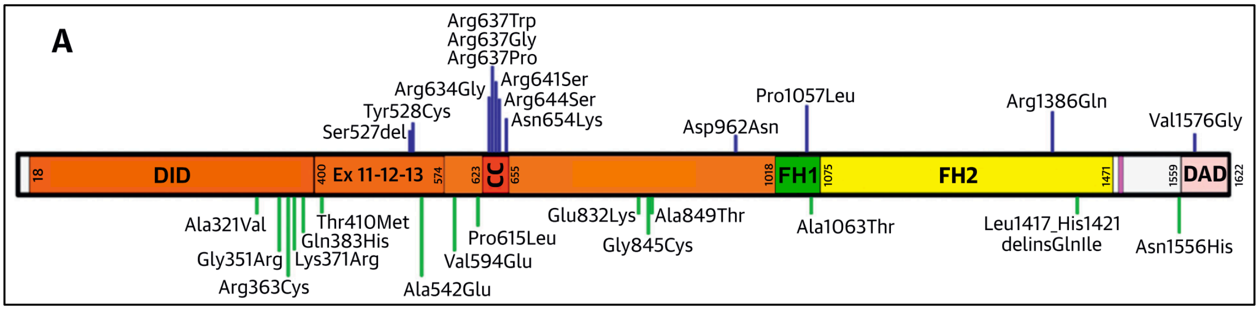

**Figure 1-3** – *Domain diagram of human FHOD3L with indicated HCM mutations*

Modified from Ochoa, et al. (2018). (**A**) The distribution across the FHOD3 protein of the mutations considered pathogenic/likely pathogenic (blue, top) and of uncertain significance (green, bottom) in HCM patients who participated in the segregation study.

## References

Ahola, A., Pölönen, R.-P., Aalto-Setälä, K., & Hyttinen, J. (2018). Simultaneous Measurement of Contraction and Calcium Transients in Stem Cell Derived Cardiomyocytes. *Annals of Biomedical Engineering*, *46*(1), 148–158. https://doi.org/10.1007/s10439-017-1933-2

Arimura, T., Takeya, R., Ishikawa, T., Yamano, T., Matsuo, A., Tatsumi, T., Nomura, T., Sumimoto, H., & Kimura, A. (2013). Dilated Cardiomyopathy-Associated FHOD3 Variant Impairs the Ability to Induce Activation of Transcription Factor Serum Response Factor. *Circ J*, *77*(12), 2990-2996. https://doi.org/10.1253/circj.cj-13-0255

Bers, D. M. (2001). *Excitation-Contraction Coupling and Cardiac Contractile Force*. https://link.springer.com/book/10.1007/978-94-010-0658-3

Boudaoud, A., Burian, A., Borowska-Wykręt, D., Uyttewaal, M., Wrzalik, R., Kwiatkowska, D., & Hamant, O. (2014). FibrilTool, an ImageJ plug-in to quantify fibrillar structures in raw microscopy images. *Nature Protocols*, *9*(2), Article 2. https://doi.org/10.1038/nprot.2014.024

Psaras, Y., Margara, F., Cicconet, M., Sparrow, A. J., Repetti, G. G., Schmid, M., Steeples, V., Wilcox, J. A. L., Bueno-Orovio, A., Redwood, C. S., Watkins, H. C., Robinson, P., Rodriguez, B., Seidman, J. G., Seidman, C. E., & Toepfer, C. N. (2021). CalTrack: High-Throughput Automated Calcium Transient Analysis in Cardiomyocytes. *Circulation Research*, *129*(2), 326-341. https://doi.org/10.1161/CIRCRESAHA.121.318868

Campellone, K. G., & Welch, M. D. (2010). A Nucleator Arms Race: Cellular Control of Actin Assembly. *Nature Reviews. Molecular Cell Biology*, *11*(4), 237–251. https://doi.org/10.1038/nrm2867

Courtemanche, N. (2018). Mechanisms of formin-mediated actin assembly and dynamics. *Biophysical Reviews*, *10*(6), 1553–1569. https://doi.org/10.1007/s12551-018-0468-6

Denes, L. T., Kelley, C. P., & Wang, E. T. (2021). Microtubule-based transport is essential to distribute RNA and nascent protein in skeletal muscle. *Nature Communications*, *12*(1), 6079. https://doi.org/10.1038/s41467-021-26383-9

Dolan, E. B., Verbruggen, S. W., & Rolfe, R. A. (2018). Chapter 1—Techniques for studying mechanobiology. In S. W. Verbruggen (Ed.), *Mechanobiology in Health and Disease* (pp. 1–53). Academic Press. https://doi.org/10.1016/B978-0-12-812952-4.00001-5

Dunham, C. S., Mackenzie, M. E., Nakano, H., Kim, A. R., Nakano, A., Stieg, A. Z., & Gimzewski, J. K. (2022). Cardio PyMEA: A user-friendly, open-source Python application for cardiomyocyte microelectrode array analysis. *PloS One*, *17*(5), e0266647. https://doi.org/10.1371/journal.pone.0266647

Fenix, A. M., Neininger, A. C., Taneja, N., Hyde, K., Visetsouk, M. R., Garde, R. J., & Burnette, D. T. (2018). Muscle-specific stress fibers give rise to sarcomeres in cardiomyocytes. *eLife*, *7*, e42144. https://doi.org/10.7554/eLife.42144

Fujimoto, N., Kan-o, M., Ushijima, T., Kage, Y., Tominaga, R., Sumimoto, H., & Takeya, R. (2016). Transgenic Expression of the Formin Protein Fhod3 Selectively in the Embryonic Heart: Role of Actin-Binding Activity of Fhod3 and Its Sarcomeric Localization during Myofibrillogenesis. *PLoS ONE*, *11*(2), e0148472. https://doi.org/10.1371/journal.pone.0148472

Fürst, D. O., Osborn, M., Nave, R., & Weber, K. (1988). The organization of titin filaments in the half-sarcomere revealed by monoclonal antibodies in immunoelectron microscopy: A map of ten nonrepetitive epitopes starting at the Z line extends close to the M line. *Journal of Cell Biology*, *106*(5), 1563–1572. https://doi.org/10.1083/jcb.106.5.1563

Gasteier, J. E., Madrid, R., Krautkrämer, E., Schröder, S., Muranyi, W., Benichou, S., & Fackler, O. T. (2003). Activation of the Rac-binding Partner FHOD1 Induces Actin Stress Fibers via a ROCK-dependent Mechanism. *Journal of Biological Chemistry*, *278*(40), 38902–38912. https://doi.org/10.1074/jbc.M306229200

Gautel, M., & Goulding, D. (1996). A molecular map of titin/connectin elasticity reveals two different mechanisms acting in series. *FEBS Letters*, *385*(1–2), 11–14. https://doi.org/10.1016/0014-5793(96)00338-9

Gould, C. J., Maiti, S., Michelot, A., Graziano, B. R., Blanchoin, L., & Goode, B. L. (2011). The Formin DAD Domain Plays Dual Roles in Autoinhibition and Actin Nucleation. *Current Biology*, *21*(5), 384–390. https://doi.org/10.1016/j.cub.2011.01.047

Grune, T., Ott, C., Häseli, S., Höhn, A., & Jung, T. (2019). The “MYOCYTER” – Convert cellular and cardiac contractions into numbers with ImageJ. *Scientific Reports*, *9*(1), Article 1. https://doi.org/10.1038/s41598-019-51676-x

Guatimosim, S., Guatimosim, C., & Song, L.-S. (2011). Imaging Calcium Sparks in Cardiac Myocytes. *Methods Mol Biol*, *689*, 205–214. https://doi.org/10.1007/978-1-60761-950-5_12

Herman, I. M. (1993). Actin isoforms. *Current Opinion in Cell Biology*, *5*(1), 48–55. https://doi.org/10.1016/S0955-0674(05)80007-9

Huebsch, N., Loskill, P., Mandegar, M. A., Marks, N. C., Sheehan, A. S., Ma, Z., Mathur, A., Nguyen, T. N., Yoo, J. C., Judge, L. M., Spencer, C. I., Chukka, A. C., Russell, C. R., So, P.-L., Conklin, B. R., & Healy, K. E. (2015). Automated Video-Based Analysis of Contractility and Calcium Flux in Human-Induced Pluripotent Stem Cell-Derived Cardiomyocytes Cultured over Different Spatial Scales. *Tissue Engineering Part C: Methods*, *21*(5), 467–479. https://doi.org/10.1089/ten.tec.2014.0283

Huxley, A. F., & Niedergerke, R. (1954). Structural Changes in Muscle During Contraction: Interference Microscopy of Living Muscle Fibres. *Nature*, *173*(4412), 971–973. https://doi.org/10.1038/173971a0

Huxley, H., & Hanson, J. (1954). Changes in the Cross-Striations of Muscle during Contraction and Stretch and their Structural Interpretation. *Nature*, *173*(4412), 973–976. https://doi.org/10.1038/173973a0

Iskratsch, T., Yu, C.-H., Mathur, A., Hone, J., Ehler, E., & Sheetz, M. (2013). FHOD1 Is Needed for Directed Forces and Adhesion Maturation during Cell Spreading and Migration. *Developmental Cell*, *27*(5), 545-559. https://doi.org/10.1016/j.devcel.2013.11.003

Kan-o, M., Takeya, R., Abe, T., Kitajima, N., Nishida, M., Tominaga, R., Kurose, H., & Sumimoto, H. (2012). Mammalian formin Fhod3 plays an essential role in cardiogenesis by organizing myofibrillogenesis. *Biology Open | The Company of Biologists*, *1*(9), 889-896. https://doi.org/10.1242/bio.20121370

Kan-o, M., Takeya, R., Taniguchi, K., Tanoue, Y., Tominaga, R., & Sumimoto, H. (2012). Expression and Subcellular Localization of Mammalian Formin Fhod3 in the Embryonic and Adult Heart. *PLOS ONE*, *7*(4), e34765. https://doi.org/10.1371/journal.pone.0034765

Lewis, Y. E., Moskovitz, A., Mutlak, M., Heineke, J., Caspi, L. H., & Kehat, I. (2018). Localization of transcripts, translation, and degradation for spatiotemporal sarcomere maintenance. *Journal of Molecular and Cellular Cardiology*, *116*, 16–28. https://doi.org/10.1016/j.yjmcc.2018.01.012

Linke, W. A., Ivemeyer, M., Olivieri, N., Kolmerer, B., Rüegg, C. J., & Labeit, S. (1996). Towards a Molecular Understanding of the Elasticity of Titin. *Journal of Molecular Biology*, *261*(1), 62–71. https://doi.org/10.1006/jmbi.1996.0441

Littlefield, R. S., & Fowler, V. M. (2008). Thin Filament Length Regulation in Striated Muscle Sarcomeres: Pointed-end dynamics go beyond a nebulin ruler. *Seminars in Cell & Developmental Biology*, *19*(6), 511–519. https://doi.org/10.1016/j.semcdb.2008.08.009

Maruyama, K., Natori, R., & Nonomura, Y. (1976). New elastic protein from muscle. *Nature*, *262*(5563), 58–60. https://doi.org/10.1038/262058a0

Mitchison, T. J., & Cramer, L. P. (1996). Actin-Based Cell Motility and Cell Locomotion. *Cell*, *84*(3), 371–379. https://doi.org/10.1016/S0092-8674(00)81281-7

Müller, M., Diensthuber, R. P., Chizhov, I., Claus, P., Heissler, S. M., Preller, M., Taft, M. H., & Manstein, D. J. (2013). Distinct Functional Interactions between Actin Isoforms and Nonsarcomeric Myosins. *PLoS ONE*, *8*(7), e70636. https://doi.org/10.1371/journal.pone.0070636

Nakano, H., Minami, I., Braas, D., Pappoe, H., Wu, X., Sagadevan, A., Vergnes, L., Fu, K., Morselli, M., Dunham, C., Ding, X., Stieg, A. Z., Gimzewski, J. K., Pellegrini, M., Clark, P. M., Reue, K., Lusis, A. J., Ribalet, B., Kurdistani, S. K., … Nakano, A. (2017). Glucose inhibits cardiac muscle maturation through nucleotide biosynthesis. *eLife*, *6*, e29330. https://doi.org/10.7554/eLife.29330

Neininger-Castro, A. C., Jr, J. B. H., Sanchez, Z. C., Taneja, N., Fenix, A. M., Moparthi, S., Vassilopoulos, S., & Burnette, D. T. (2023). Independent regulation of Z-lines and M-lines during sarcomere assembly in cardiac myocytes revealed by the automatic image analysis software sarcApp. *eLife*, *12*. https://doi.org/10.7554/eLife.87065.2

Ochoa, J. P., Sabater-Molina, M., Garcia-Pinilla, J. M., Mogensen, J., Restrepo-Cordoba, A., Palomino-Doza, J., Villacorta, E., Martinez-Moreno, M., Ramos-Maqueda, J., Zorio, E., Peña-Peña, M. L., García-Granja, P. E., Rodríguez-Palomares, J. F., Cárdenas-Reyes, I. J., de la Torre-Carpente, M. M., Bautista-Pavés, A., Akhtar, M. M., Cicerchia, M. N., Bilbao-Quesada, R., … Monserrat, L. (2018). Formin Homology 2 Domain Containing 3 (FHOD3) Is a Genetic Basis for Hypertrophic Cardiomyopathy. *Journal of the American College of Cardiology*, 72(20), 2457-2467. https://doi.org/10.1016/j.jacc.2018.10.001

Palmer, B. M., Swank, D. M., Miller, M. S., Tanner, B. C. W., Meyer, M., & LeWinter, M. M. (2020). Enhancing diastolic function by strain-dependent detachment of cardiac myosin crossbridges. *Journal of General Physiology*, *152*(4), e201912484. https://doi.org/10.1085/jgp.201912484

Patel, A. A., Oztug Durer, Z. A., van Loon, A. P., Bremer, K. V., & Quinlan, M. E. (2018). Drosophila and human FHOD family formin proteins nucleate actin filaments. *The Journal of Biological Chemistry*, *293*(2), 532–540. https://doi.org/10.1074/jbc.M117.800888

Perriard, J.-C., Hirschy, A., & Ehler, E. (2003). Dilated Cardiomyopathy: A Disease of the Intercalated Disc? *Trends in Cardiovascular Medicine*, *13*(1), 30–38. https://doi.org/10.1016/S1050-1738(02)00209-8

Perrin, B. J., & Ervasti, J. M. (2010). The Actin Gene Family: Function Follows Isoform. *Cytoskeleton*, *67*(10), 630–634. https://doi.org/10.1002/cm.20475

Pirani, A., Vinogradova, M. V., Curmi, P. M. G., King, W. A., Fletterick, R. J., Craig, R., Tobacman, L. S., Xu, C., Hatch, V., & Lehman, W. (2006). An Atomic Model of the Thin Filament in the Relaxed and $Ca^{2+}$-Activated States. *Journal of Molecular Biology*, *357*(3), 707–717. https://doi.org/10.1016/j.jmb.2005.12.050

Pollard, T. D. (1986). Assembly and dynamics of the actin filament system in nonmuscle cells. *Journal of Cellular Biochemistry*, *31*(2), 87–95. https://doi.org/10.1002/jcb.240310202

Pollard, T. D. (2016). Actin and Actin-Binding Proteins. *Cold Spring Harbor Perspectives in Biology*, *8*(8), a018226. https://doi.org/10.1101/cshperspect.a018226

Sala, L., Van Meer, B. J., Tertoolen, L. G. J., Bakkers, J., Bellin, M., Davis, R. P., Denning, C., Dieben, M. A. E., Eschenhagen, T., Giacomelli, E., Grandela, C., Hansen, A., Holman, E. R., Jongbloed, M. R. M., Kamel, S. M., Koopman, C. D., Lachaud, Q., Mannhardt, I., Mol, M. P. H., … Mummery, C. L. (2018). MUSCLEMOTION A Versatile Open Software Tool to Quantify Cardiomyocyte and Cardiac Muscle Contraction In Vitro and In Vivo. *Circulation Research*, *122*(3), e5–e16. https://doi.org/10.1161/CIRCRESAHA.117.312067

Schönichen, A., Mannherz, H. G., Behrmann, E., Mazur, A. J., Kühn, S., Silván, U., Schoenenberger, C.-A., Fackler, O. T., Raunser, S., Dehmelt, L., & Geyer, M. (2013). FHOD1 is a combined actin filament capping and bundling factor that selectively associates with actin arcs and stress fibers. *Journal of Cell Science*, *126*(8), 1891–1901. https://doi.org/10.1242/jcs.126706

Simiczyjew, A., Mazur, A. J., Dratkiewicz, E., & Nowak, D. (2017). Involvement of β- and γ-actin isoforms in actin cytoskeleton organization and migration abilities of bleb-forming human colon cancer cells. *PLoS ONE*, *12*(3), e0173709. https://doi.org/10.1371/journal.pone.0173709

Taniguchi, K., Takeya, R., Suetsugu, S., Kan-o, M., Narusawa, M., Shiose, A., Tominaga, R., & Sumimoto, H. (2009). Mammalian formin Fhod3 regulates actin assembly and sarcomere organization in striated muscles. *Journal of Biological Chemistry*, *284*(43), 29873–29881. https://doi.org/10.1074/jbc.M109.059303

Ushijima, T., Fujimoto, N., Matsuyama, S., Kan-o, M., Kiyonari, H., Shioi, G., Kage, Y., Yamasaki, S., Takeya, R., & Sumimoto, H. (2018). The actin-organizing formin protein Fhod3 is required for postnatal development and functional maintenance of the adult heart in mice. *The Journal of Biological Chemistry*, *293*(1), 148–162. https://doi.org/10.1074/jbc.M117.813931

Valencia, DA, Quinlan, M. (2021). Formins. *Current Biology*, *31*(10), R517-R522. https://doi.org/10.1016/j.cub.2021.02.047

Vizcarra, C. L., Bor, B., & Quinlan, M. E. (2014). The Role of Formin Tails in Actin Nucleation, Processive Elongation, and Filament Bundling. *The Journal of Biological Chemistry*, *289*(44), 30602–30613. https://doi.org/10.1074/jbc.M114.588368

Zhu, H., Scharnhorst, K. S., Stieg, A. Z., Gimzewski, J. K., Minami, I., Nakatsuji, N., Nakano, H., & Nakano, A. (2017). Two dimensional electrophysiological characterization of human pluripotent stem cell-derived cardiomyocyte system. *Scientific Reports*, *7*(1), Article 1. https://doi.org/10.1038/srep43210

# Appendix

disrupt Hem1 structure, leading to WRC degradation, except for the M371V mutation, which has been suggested to disrupt Arf1–WRC signaling.

## Outlook and future directions

Many important questions remain to be answered for a complete understanding of the function and regulation of the WRC, from both a biochemical/structural and cell biological perspective. A key remaining question is how the WRC interacts with or becomes activated by various ligands, including Rac1, Arf1, $PIP_3$ and many other molecules, both individually and cooperatively, and both *in vitro* and at the plasma membrane of cells. As an example, it is still unclear whether WRC activation can be separated from its recruitment to the membrane. Answering all of these questions will promote the development of inhibitors, activators, and chemical or optogenetic tools to control or track WRC functions in cells, which will be of both scientific and potential medical relevance. Such tools might also provide us with the ability to unravel additional, perhaps less canonical, functions to those summarized above. How different WRC variants containing distinct combinations of subunits are differentially regulated in cells is emerging as yet another exciting future topic. Additional questions that have remained almost entirely unanswered include the regulation of WRC assembly, recycling and degradation, as well as biochemical mechanisms of WRC regulation in plants. Last, but not least, it will be essential that a full understanding of WRC regulation and function establishes how its individual subunits also participate in other complexes, such as Sra1 with FMRP–eIF4E, and how cells balance all of these individual subunit activities in normal development and disease.

## FURTHER READING

Begemann, A., Sticht, H., Begtrup, A., Vitobello, A., Faivre, L., Banka, S., Alhaddad, B., Asadollahi, R., Becker, J., Bierhals, T., *et al*. (2020). New insights into the clinical and molecular spectrum of the novel CYFIP2-related neurodevelopmental disorder and impairment of the WRC-mediated actin dynamics. Genet. Med. *23*, 543–554.

Chen, B., Brinkmann, K., Chen, Z., Pak, C.W., Liao, Y., Shi, S., Henry, L., Grishin, N.V., Bogdan, S., and Rosen, M.K. (2014). The WAVE regulatory complex links diverse receptors to the actin cytoskeleton. Cell *156*, 195–207.

Chen, B., Chou, H.T., Brautigam, C.A., Xing, W., Yang, S., Henry, L., Doolittle, L.K., Walz, T., and Rosen, M.K. (2017). Rac1 GTPase activates the WAVE regulatory complex through two distinct binding sites. eLife *6*, e29795.

Chen, Z., Borek, D., Padrick, S.B., Gomez, T.S., Metlagel, Z., Ismail, A.M., Umetani, J., Billadeau, D.D., Otwinowski, Z., and Rosen, M.K. (2010). Structure and control of the actin regulatory WAVE complex. Nature *468*, 533–538.

Cook, S.A., Comrie, W.A., Poli, M.C., Similuk, M., Oler, A.J., Faruqi, A.J., Kuhns, D.B., Yang, S., Vargas-Hernandez, A., Carisey, A.F., *et al*. (2020). HEM1 deficiency disrupts mTORC2 and F-actin control in inherited immunodysregulatory disease. Science *369*, 202–207.

Fort, L., Batista, J.M., Thomason, P.A., Spence, H.J., Whitelaw, J.A., Tweedy, L., Greaves, J., Martin, K.J., Anderson, K.I., Brown, P., *et al*. (2018). Fam49/CYRI interacts with Rac1 and locally suppresses protrusions. Nat. Cell Biol. *20*, 1159–1171.

Gautreau, A., Ho, H.Y., Li, J., Steen, H., Gygi, S.P., and Kirschner, M.W. (2004). Purification and architecture of the ubiquitous Wave complex. Proc. Natl. Acad. Sci. USA *101*, 4379–4383.

Innocenti, M., Gerboth, S., Rottner, K., Lai, F.P., Hertzog, M., Stradal, T.E., Frittoli, E., Didry, D., Polo, S., Disanza, A., *et al*. (2005). Abi1 regulates the activity of N-WASP and WAVE in distinct actin-based processes. Nat. Cell Biol. *7*, 969–976.

Koronakis, V., Hume, P.J., Humphreys, D., Liu, T., Horning, O., Jensen, O.N., and McGhie, E.J. (2011). WAVE regulatory complex activation by cooperating GTPases Arf and Rac1. Proc. Natl. Acad. Sci. USA *108*, 14449–14454.

Lebensohn, A.M., and Kirschner, M.W. (2009). Activation of the WAVE complex by coincident signals controls actin assembly. Mol. Cell *36*, 512–524.

Qin, H., Lu, S., Thangaraju, M., and Cowell, J.K. (2019). Wasf3 deficiency reveals involvement in metastasis in a mouse model of breast cancer. Am. J. Pathol. *189*, 2450–2458.

Salzer, E., Zoghi, S., Kiss, M.G., Kage, F., Rashkova, C., Stahnke, S., Haimel, M., Platzer, R., Caldera, M., Ardy, R.C., *et al*. (2020). The cytoskeletal regulator HEM1 governs B cell development and prevents autoimmunity. Sci. Immunol. *5*, eabc3979.

Schaks, M., Singh, S.P., Kage, F., Thomason, P., Klunemann, T., Steffen, A., Blankenfeldt, W., Stradal, T.E., Insall, R.H., and Rottner, K. (2018). Distinct interaction sites of Rac GTPase with WAVE regulatory complex have non-redundant functions in vivo. Curr. Biol. *28*, 3674–3684.e6.

Wu, S., Ma, L., Wu, Y., Zeng, R., and Zhu, X. (2012). Nudel is crucial for the WAVE complex assembly in vivo by selectively promoting subcomplex stability and formation through direct interactions. Cell Res. *22*, 1270–1284.

Yamazaki, D., Suetsugu, S., Miki, H., Kataoka, Y., Nishikawa, S., Fujiwara, T., Yoshida, N., and Takenawa, T. (2003). WAVE2 is required for directed cell migration and cardiovascular development. Nature *424*, 452–456.

[1]Division of Molecular Cell Biology, Zoological Institute, Technische Universität Braunschweig, Spielmannstrasse 7, 38106 Braunschweig, Germany. [2]Department of Cell Biology, Helmholtz Centre for Infection Research, Inhoffenstrasse 7, 38124 Braunschweig, Germany. [3]Roy J. Carver Department of Biochemistry, Biophysics and Molecular Biology, Iowa State University, 3110 Molecular Biology Building, Ames, IA, USA.
*E-mail: k.rottner@tu-braunschweig.de (K.R.); stone@iastate.edu (B.C.)

---

## Primer

# Formins

Dylan A. Valencia[1,2]
and Margot E. Quinlan[2,3,*]

Actin is one of the most abundant proteins in eukaryotes. Discovered in muscle and described as far back as 1887, actin was first purified in 1942. It plays myriad roles in essentially every eukaryotic cell. Actin is central to development, muscle contraction, and cell motility, and it also functions in the nucleus, to name a spectrum of examples. The flexibility of actin function stems from two factors: firstly, it is dynamic, transitioning between monomer and filament, and, secondly, there are hundreds of actin-binding proteins that build and organize specific actin-based structures. Of prime importance are actin nucleators — proteins that stimulate *de novo* formation of actin filaments. There are three known classes of actin nucleators: the Arp2/3 complex, formins, and tandem WASP homology 2 (WH2) nucleators. Each class nucleates by a distinct mechanism that contributes to the organization of the larger structure being built. Evidence shows that the Arp2/3 complex produces branched actin filaments, remaining bound at the branch point, while formins create linear actin filaments, remaining bound at the growing end. Here, we focus on the formin family of actin nucleators.

Formins are crucial proteins for a range of cellular processes, as demonstrated by their links to various pathologies, including cardiomyopathies, cancers, intellectual disabilities and other neuronal disorders, nonsyndromic deafness, and renal disorders. It follows that understanding how formins help to build actin-based structures is essential to our knowledge of normal physiology as well as many pathologies. In this Primer, we highlight the biochemical activities underlying actin assembly by formins and, where possible, we weave in links between biochemistry and biological roles. Finally, we discuss outstanding questions about formins.

## The importance of nucleators

Nucleators are essential for tightly regulated actin assembly. The initial step of actin filament

Table 1. The metazoan formin superfamily.

| Subtype (full name) | Human isoforms | Associated structures or processes | Associated diseases |
|---|---|---|---|
| **Dia**<br>(Diaphanous) | Dia1, Dia2, Dia3 | Stress fibers, contractile ring, microtubule stabilization and cell migration | Deafness, seizures, cortical blindness, microcephaly syndrome |
| **Daam**<br>(Disheveled-associated activators of morphogenesis) | Daam1, Daam2 | Planar cell polarity, cilia, sarcomeres | Unknown |
| **FMNL/FRL**<br>(Formin-related proteins identified in leukocytes) | FMNL1, FMNL2, FMNL3 | Cell morphology, cortical actin | Unknown |
| **INF**<br>('inverted' formins) | INF1, INF2 | Mitochondrial fission | Focal segmental glomerulosclerosis, Charcot-Marie-Tooth disease |
| **FHOD**<br>(Formin homology domain containing proteins) | Fhod1, Fhod3 | Sarcomeres, stress fibers | Hypertrophic cardiomyopathy and possibly other cardiac disorders |
| **GRID2IP**<br>(Delphilin) | Delphilin | Purkinje cells | Unknown |
| **FMN**<br>(the founding family of 'formins') | Fmn1, Fmn2 | Oogenesis, DNA damage response | Polydactyly, intellectual disability |
| **MWHF**<br>(Multiple wing hairs formins) | N/A | Unknown | N/A |
| **PHCF**<br>(PH-domain-containing formins) | N/A | Unknown | N/A |

formation — nucleation — is a kinetically unfavorable process. That is, actin alone spontaneously nucleates, but it does so at a much slower rate than that required for cellular actin dynamics. In addition, some actin-binding proteins (primarily profilin) bind to most available actin monomers in the cytoplasm, further limiting nucleation. Given the need to assemble structures at strictly controlled locations, at specific times, and in response to rapidly changing signals, the cell uses nucleators to 'turn on' actin assembly at will.

After the nucleation of a new actin filament, the filament grows or elongates. *In vitro*, one end of the filament, the so-called 'barbed' end, grows around ten times faster than the other end, the 'pointed' end. Growth at the barbed end is believed to be the dominant form of elongation in the cell. An important feature of formins, compared with other actin nucleators, is that they are elongation factors as well. That is, formins remain associated with the fast-growing barbed end, in some cases markedly accelerating growth and also competing with proteins that inhibit growth, such as capping protein. In this way, formins influence the length of actin filaments, in addition to their number.

## The formin superfamily

The first 'formin' was so named to reflect the defect in mouse limb formation that resulted from mutations in the *limb deformity* locus. In fact, the *limb deformity* phenotype is now attributed to two neighboring genes: Fmn1, of the FMN-subtype of formins, and gremlin, an unrelated gene. Shortly after Fmn1 was identified, a similar gene, *diaphanous*, was found to be essential for cytokinesis in *Drosophila*. When related yeast proteins were shown to nucleate actin assembly, the formin family of actin nucleators was established. Metazoans have nine subtypes of formins in the superfamily (Table 1), with humans having 15 different formin genes (and more isoforms due to alternative splicing) representing seven of the nine subtypes. Genomic evidence suggests that placental mammals lost the other two subtypes. The common yeast models, fission and budding yeast, have formins that are closely related to metazoan formins of the Dia subtype. Other fungi have formins that do not fall into the nine metazoan subtypes, although they likely arose from a Dia-like ancestor. More distant species show continued divergence. For example, plants have formins that fall into three distinct classes or subtypes. Phylogenetically, the core formin homology 2 (FH2) domain likely arose once during eukaryotic evolution and was connected to other structural domains through gene duplication events and divergence, resulting in varied subtypes.

Most cells contain a diverse complement of formins that is needed to build a collection of structures, including tightly organized stress fibers (require Dia, Fhod, Daam; metazoan formin subtypes, but not specific formin genes, are given here) and sarcomeres (Daam, Fhod), diffuse meshes that fill the oocyte (Fmn), long narrow filopodia (Dia, FMNL), transient structures on mitochondria (INF2), and the cytokinetic contractile ring (Dia), among many others (Figure 1 and

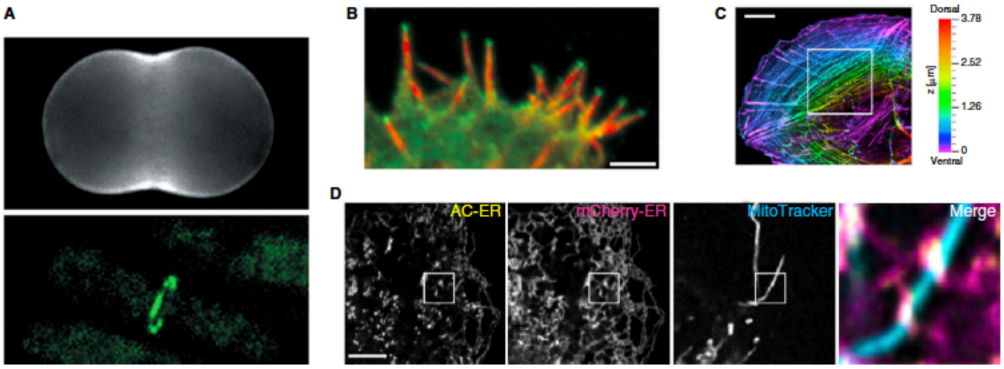

**Figure 1. Fluorescence images of formin-dependent actin structures.**
(A) Contractile rings in a large and a small cell. Sea urchin embryo (top) stained for actin filaments with rhodamine–phalloidin, and fission yeast cell (bottom) expressing a myosin light chain–GFP fusion protein. The fission yeast cell is approximately 14 times smaller than the sea urchin cell. (Reproduced from Chang and Burgess (2003) Curr. Biol. *13*, R692–R693.) (B) A *Dictyostelium* cell expressing GFP-tagged full-length dDia2 was fixed and labelled with anti-GFP antibodies to visualize dDia2 (green) and with TRITC–phalloidin to visualize F-actin (red). The formin is enriched at the tips of filopodia. Scale bar: 2 µm. (Image used with permission from Portland Press © Schirenbeck *et al*. (2005) Biochem. Soc. Trans. *33*, 1256–1259.) (C) Stress fibers in U2OS cells. Depicted is the maximum projection of a confocal Z-stack (F-actin), in which the z-coordinates are indicated by the color bar. Scale bar: 10 µm. (Reproduced from Schulze *et al*. (2014) J. Cell Sci. *127*, 1379–1393, with permission.) (D) Accumulation of actin, as indicated by an endoplasmic reticulum targeted actin nanobody (AC–ER), is observed at mitochondria–ER crossover points. Co-expression in U2OS cells of mCherry–ER and AC–ER, labeled with MitoTracker. Scale bar: 5 µm. (Reprinted by permission from Springer Nature, Schiavon *et al*. (2020) Nat. Methods *17*, 917–921 © 2020.)

Table 1). A clear example of the functional specificity of formins comes from fission yeast. This single-celled organism has four major actin-based structures built by four nucleators: the Arp2/3 complex and three different formins. The Arp2/3 complex nucleates actin in endocytic patches, and the formins For3, Cdc12, and Fus1 nucleate actin for cables, cytokinesis, and fusion during sexual reproduction, respectively. With so many formins, it is important to understand how their specificity of function arises.

## Formin structure and function

Each formin has characteristic nucleation and elongation activities, suggesting that precise actin assembly activity is central to the ability of the formin superfamily to build such a broad range of actin-based structures. Structurally, formins are defined by the eponymous formin homology (FH) domains 1 and 2 (Figure 2A). These domains are straddled by regulatory domains that modulate their activity (Figure 2B). Central to the actin nucleator role of formins is the FH2 domain, which forms a donut-shaped homodimer (Figure 2C). The FH2 domain is sufficient to nucleate and processively move with the growing barbed end of the actin filament (Figure 2D,E). The nucleation process remains poorly understood. Existing models suggest that the FH2 homodimer stabilizes otherwise short-lived actin dimers or trimers, thereby favoring filament formation (Figure 2C). Efficiencies as low as 0.02 filaments/nucleator and as high as 0.2 have been reported. The FH2 domain also influences the rate of filament elongation by a process termed gating, which is modeled as switching between two conformational states — 'open' and 'closed'. The fraction of time spent in the closed state determines the extent to which elongation is slowed by the FH2 domain. The gating fraction ranges from essentially 0 to 1 for different formins.

The rate of elongation is also controlled by the FH1 domain. This unstructured, proline-rich domain indirectly binds actin via the actin-monomer-binding protein profilin. The commonly accepted model for promotion of actin filament elongation by FH1 domains is the 'capture and delivery' model: the FH1 domain binds (captures) profilin-bound actin and rapidly delivers it to the growing end of the actin filament (Figure 2E). Under typical conditions used to study formin-mediated actin assembly *in vitro*, capture is the slowest step. Recent work has shown that profilin release from the actin filament can be rate-limiting at physiological concentrations of profilin–actin (~two orders of magnitude higher than common (and practical) concentrations used for *in vitro* studies). The composition of FH1 domains varies widely. Some FH1 domains have only one or two profilin-binding sites, while others have as many as ten. The number of profilin-binding sites, their distances from the FH2 domain and their affinities for profilin all influence the efficacy of a given FH1 domain. Consistent with the range of FH1 domains and FH2-mediated gating, the resulting effect on formin-mediated elongation rates varies widely, with FMNL1 slowing elongation by around fivefold and Dia1 accelerating elongation by around fivefold.

Given that formins set the elongation rate, the time that a formin remains associated with a filament is also important. This property is referred to as processivity. The product of the elongation rate and processivity (or off-rate) determines the characteristic run length of (or typical filament length built by) a given formin. Characteristic run lengths as short as 2 µm and as long as 200 µm have been reported.

To summarize, among the formins characterized to date, the range of nucleation activity is at least one order of magnitude, the range of gating is

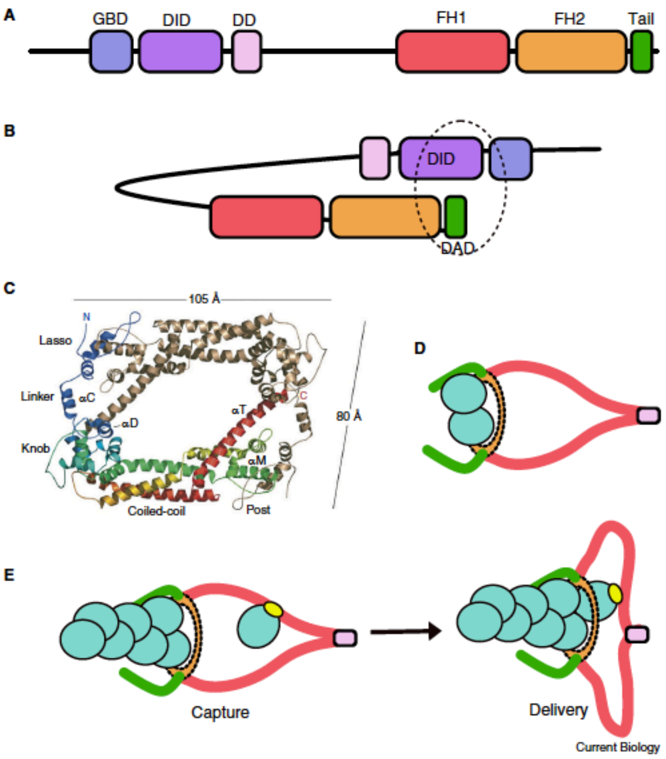

**Figure 2. Formin structures and models of assembly.**
(A) Domain structure of (Diaphanous-related) formins. GBD, GTPase-binding domain; DID, Diaphanous inhibitory domain; DD, dimerization domain; FH1, formin homology 1 domain; FH2, formin homology 2 domain; tail, includes the Diaphanous autoinhibitory domain (DAD). (B) Autoinhibitory interaction between the DID and DAD. (C) Crystal structure of an FH2 domain (Bni1p). Dimensions and subdomains are indicated. (Reproduced from Xu *et al.* (2004) Cell *116*, 711–723.) (D) Nucleation: the FH2 domain stabilizes an actin dimer with help from the tail. Domains are color matched to (A) and actin is light blue. (E) Elongation: the FH1 domain binds (captures) profilin-bound actin (profilin is yellow). The flexible FH1 domain then delivers actin to the barbed end of the growing filament.

two orders of magnitude, the range of elongation rates is at least one order of magnitude, and the range of processivities is at least two orders of magnitude. The combination of nucleation, elongation, and processivity can lead to a range of six orders of magnitude in overall activity, resulting in many short filaments, a few long filaments, and everything in between. Notably, this is the range of activities measured *in vitro*, without considering the proteins and post-translational modifications that could further modify any step of actin assembly mediated by formins.

## Regulation of formin activity

Controlling when and where new actin structures are built is critical. Thus, tight regulation of formin activity is a must. A third conserved domain, FH3, was found to be part of a larger regulatory domain in formins. First described in the formin Dia1, this domain is commonly referred to as the Diaphanous inhibitory domain or DID (Figure 2A). On either side of the DID is a GTPase-binding domain (GBD) and a dimerization domain. The DID makes an intramolecular interaction with a short motif at the carboxyl terminus, called the Diaphanous autoregulatory domain (DAD), which results in autoinhibition (Figure 2B). Thus, purified full-length formins are generally inactive. DIDs and DADs are present in four other subtypes of formins, in addition to the Diaphanous subtype. FMN-family formins are autoinhibited in an analogous manner, despite lacking recognizable DIDs and DADs. The three other subtypes — Delphilin, PHCF, and MWHF formins — appear to be regulated by distinct mechanisms. Only MWHF formins retain the DID and all three lack a recognizable carboxy-terminal DAD. While some formins might have a cryptic functional DAD, others do not have any carboxy-terminal sequence beyond the FH2 domains, necessitating an alternative mechanism to inhibit activity.

The first formin activator described was the small GTPase Rho, which binds to the GBD, adjacent to the DID of Dia1. However, Rho-mediated formin activation was incomplete when analyzed in biochemical assays. Subsequently, other small GTPases were linked to activation of specific formins. Mammals do not have fifteen small GTPases, suggesting that the specificity of activity is more complex. Recently, the contractile ring proteins anillin and IQGAP1 were proposed to mediate localization and co-activate specific formins in conjunction with Rho. Additional proteins and post-translational modifications are likely to modify formin activity. For example, purified full-length INF2 is active, despite the presence of DID and DAD domains. For this formin, an inhibitory complex of lysine-acetylated actin and cyclase-associated protein is required to stabilize or perhaps bridge the DID–DAD inhibitory interaction. A well-studied example of post-translational modification comes from the FHOD subtype of formins, including Fhod1 and Fhod3. Fhod3 is important for sarcomere formation in both skeletal and cardiac muscle, and two distinct phosphorylation events regulate this formin. One phosphorylation site is within an alternatively spliced exon and phosphorylation by casein kinase 2 drives the subcellular localization of Fhod3 to sarcomeres. Phosphorylation by the Rho-associated kinase ROCK of a consensus site within the DAD of both Fhod1 and Fhod3 weakens the intramolecular interaction between the DID and DAD and is sufficient to activate these formins in cells.

In addition to containing the DAD, the carboxy-terminal tail directly influences actin assembly. Formin tails weakly interact with actin monomers and filaments, yet they can have a strong impact on nucleation and processivity. Data suggest that the ability of formin tails to bind actin monomers, holding them in proximity to the FH2 domain, contributes to nucleation (Figure 2C). A role for the tail in nucleation fits with the fact that the DAD is located within this region: the DID–DAD interaction would compete with actin monomer binding, thereby preventing or at least reducing nucleation. The tail also enhances processivity through electrostatic interactions with actin filaments. In one case, removing the tail decreased processivity by ~1.5 orders of magnitude. One can imagine that post-translational modifications of the tail, such as the phosphorylation reported for FHOD-family formins, could modulate nucleation and/or processivity in addition to the inhibitory state, though this is yet to be tested.

Actin filaments are commonly part of the cell's force-generating structures and/or modify physical conditions within the cell. Thus, formins might need to respond to external forces. An elegant demonstration of this concept comes from reconstituting components of the cytokinetic ring. In fission yeast, the formin Cdc12p contributes actin filaments to the ring. When myosin pulls on formin-bound actin filaments, Cdc12p-mediated actin assembly is inhibited. These observations were complemented by computational estimates consistent with force-induced formin inhibition being necessary for the formation of the cytokinetic ring. Quantitative measurements of formin mechanosensitivity have been made for Bni1, Dia1, and Dia2 using microfluidics and optical or magnetic traps. Both the FH1 and FH2 domains appear to be subject to force-mediated regulation, with growth slowing or accelerating depending on force amplitude (among other conditions) and the formin itself.

## Actin isoform specificity of formins

The six mammalian isoforms of actin have at least 93% sequence identity, with most of the small amount of variation occurring in the first 10 residues at the amino terminus. This high level of conservation makes it unclear exactly why we need so many actin genes and how they function differentially. Recent studies reported a role for formins as selectors of specific actin isoforms. β-actin is enriched in the contractile ring of dividing cells and γ-actin is distributed throughout the cortex. These isoforms differ by only four residues. The primary formin at the contractile ring is Dia2, and *in vitro* experiments indicate that it selectively nucleates and elongates β-actin, potentially establishing the biased localization of this actin isoform in this context. Delphilin, a formin specific to Purkinje cells, can also differentiate between actin isoforms. Delphilin selectively nucleates non-muscle actin (β and/or γ-actin) over muscle actin (α-actin). It is not immediately obvious why Delphilin has this specificity if it is predominantly expressed in neurons. However, removal of α-actin from neurons does result in a phenotype, suggesting that this actin isoform is expressed in and important for neurons. A more intuitive example is provided by Fhod1. This formin is ubiquitously expressed, including in cardiomyocytes. In the cardiomyocyte, Fhod3 is associated with sarcomeres, the contractile units of the muscle, while Fhod1 is linked to intercalated discs, structures that mediate communication for synchronized contraction of the heart. As in cell division, actin isoforms are differentially localized: muscle actin is in sarcomeres and non-muscle actin is in intercalated discs. While we do not know if it is causative or even necessary, we do know that Fhod1 preferentially nucleates non-muscle actin. Interestingly, Fhod3 nucleates both actin isoforms, with only a slight preference for muscle actin. In contrast to these examples, other formins that have been tested for isoform specificity are not selective: FMNL1 and the *Drosophila* FMN-family formin Cappuccino (Capu), in addition to Fhod3, potently nucleate both muscle and non-muscle actin.

The fact that some formins can select between actin isoforms suggests that they are sensitive to individual amino acids. Consistent with this, we now know that formins are sensitive to specific post-translational modifications of actin, and this is a new, exciting area of investigation.

## Formins in health and disease

Given the broad range of physiological effects, it should not come as a surprise that disruption of formin function has been associated with various diseases (Table 1). For example, the Dia formin subtype is linked to several cancers, as one might expect given its essential role in cell division. In addition, specific mutations in Dia1 and Dia3 have been linked with deafness and the developmental disorder termed seizures, cortical blindness, microcephaly syndrome (SCBMS), while Dia2 mutations are associated with premature ovarian failure.

INF2 mutations are linked to both renal (focal segmental glomerular syndrome, FSGS) and neural (Charcot-Marie Tooth) disorders. All of the mutations identified to date are in the amino-terminal regulatory region of INF2, which was interpreted as evidence that loss of INF2 regulation results in pathologies. Now evidence has revealed that some of these mutants are not properly transported to the foot processes of renal podocytes, which are essential for filtration. Specifically, an amino-terminal fragment of INF2 generated by proteolysis binds and inhibits Dia1 specifically in these processes. To date there have been few reports of interactions between formins. Cdc12p and For3p both play a role at the fission yeast contractile ring, but this appears to be an indirect interaction. Formin–formin interactions are an intriguing and complex issue, giving rise to many open questions, including what happens to the other half of INF2, which is presumably constitutively active, after proteolytic cleavage? And, why, if Dia1 can be autoinhibited, would it require *trans*-inhibition by another formin?

As noted above, Fhod3 plays a role in sarcomere formation and maintenance in both skeletal and cardiac muscle. Sequencing Fhod3 in a large cohort of patients with diagnosed hypertrophic cardiomyopathy (HCM) revealed 13 mutations that are likely to be causative. Similar to INF2, most of the mutations are located outside of the FH1 and FH2 domains, but their functional consequences remain unknown. Patients live for many years with HCM and FSGS. Presumably misregulation of a formin is less detrimental than loss of function, otherwise we might expect to find more mutations in the FH2 domain.

A contrasting example comes from the *Drosophila* formin Capu, a maternal effect gene, meaning that it is essential for egg development and female fertility, but not viability. Of the many alleles that have been sequenced, most are nonsense mutations and the seven missense mutations identified were all in the FH2 domain, compromising actin assembly to different degrees. In this case, overactive Capu may be tolerated because the formin is autoinhibited and not essential, but loss of activity is detrimental to egg development. The mammalian homolog of Capu, Fmn2, is essential in the developing egg, with its loss leading to infertility in mice and likely in humans as well.

### Formin functions outside of actin assembly

The length of this section should not belie its importance. Formins can have additional activities aside from actin assembly. Many, but not all, formins bind to the sides of actin filaments and most of these bundle filaments, creating larger assemblies. At least one formin, INF2, severs actin filaments in addition to building them. Interestingly, several formins, either alone or in conjunction with microtubule-binding proteins, stabilize microtubules. They may crosslink and align actin filaments with microtubules, making formins central to overall cytoskeletal organization in some cases. Finally, some formins have additional conserved domains, such as PDZ, pleckstrin homology (PH), and WH2 domains, which likely contribute to specificity of function by determining localization or additional binding proteins. This variety of capabilities is part of how formins contribute to a broad array of structures and functions.

### Remaining questions

There is more to learn. On the biochemical front, nucleation is still poorly understood. We have a firmer grasp on elongation but there is plenty to learn about the elements that control gating, processivity, and potential crosstalk between the FH1 and FH2 domains. For example, how does a formin remain bound to a continuously growing filament end? On the cell biological front, roles for many formins are yet to be determined. In some cases, this may be complicated by crosstalk and/or compensation. For example, researchers have long sought the mechanism of actin filament formation and regulation within the sarcomere. Many proteins have been identified, including at least three formins. With advances on these two fronts we will begin to understand the link between the specific activity of a formin and its function. Finally, many proteins are known to have strong effects on different elements of actin assembly, but clear common themes have yet to be identified: there are certainly more formin-interacting proteins to be found and studied. In conclusion, all nine metazoan subfamilies of formins share common activities in terms of nucleation and elongation, but are also distinguished by activity level, localization, and cell-type-specific expression, which are probably among many other aspects that remain to be discovered!

### FURTHER READING

Bartolini, F., and Gundersen, G.G. (2010). Formins and microtubules. Biochim. Biophys. Acta *1803*, 164–173.

Chen, A., Arora, P.D., McCulloch, C.A., and Wilde, A. (2017). Cytokinesis requires localized β-actin filament production by an actin isoform specific nucleator. Nat. Commun. *8*, 1530.

Courtemanche, N., and Pollard, T.D. (2012). Determinants of formin homology 1 (FH1) domain function in actin filament elongation by formins. J. Biol. Chem. *287*, 7812–7820.

Courtemanche, N. (2018). Mechanisms of formin-mediated actin assembly and dynamics. Biophys. Rev. *10*, 1553–1569.

Funk, J., Merino, F., Venkova, L., Heydenreich, L., Kierfeld, J., Vargas, P., Raunser, S., Piel, M., and Bieling, P. (2019). Profilin and formin constitute a pacemaker system for robust actin filament growth. eLife *8*, e50963.

Kovar, D.R., and Pollard, T.D. (2004). Insertional assembly of actin filament barbed ends in association with formins produces piconewton forces. Proc. Natl. Acad. Sci. USA *101*, 14725–14730.

Pruyne, D. (2016). Revisiting the phylogeny of the animal formins: two new subtypes, relationships with multiple wing hairs proteins, and a lost human formin. PLoS One *11*, e0164067.

Subramanian, B., Chun, J., Perez-Gill, C., Yan, P., Stillman, I.E., Higgs, H.N., Alper, S.L., Schlöndorff, J.S., and Pollak, M.R. (2020). FSGS-causing INF2 mutation impairs cleaved INF2 N-fragment functions in podocytes. J. Am. Soc. Nephrol. *31*, 374–391.

Vizcarra, C.L., Bor, B., and Quinlan, M.E. (2014). The role of formin tails in actin nucleation, processive elongation, and filament bundling. J. Biol. Chem. *289*, 30602–30613.

Wioland, H., Suzuki, E., Cao, L., Romet-Lemonne, G., and Jegou, A. (2020). The advantages of microfluidics to study actin biochemistry and biomechanics. J. Muscle Res. Cell. Motil. *41*, 175–188.

Zimmermann, D., Homa, K.E., Hocky, G.M., Pollard, L.W., Cruz, E.M.D.L., Voth, G.A., Trybus, K.M., and Kovar, D.R. (2017). Mechanoregulated inhibition of formin facilitates contractile actomyosin ring assembly. Nat. Commun. *8*, 703.

[1]BMSB Graduate Program, University of California, Los Angeles, CA 90095, USA. [2]Department of Chemistry and Biochemistry, University of California, Los Angeles, CA 90095, USA. [3]Molecular Biology Institute, University of California, Los Angeles, CA 90095, USA.
*E-mail: margot@chem.ucla.edu

---

## Primer

# Intermediate filaments

**Gaëlle Dutour-Provenzano**[1,2] **and Sandrine Etienne-Manneville**[1,*]

Cell morphology, architecture and dynamics primarily rely on intracellular cytoskeletal networks, which in metazoans are mainly composed of actin microfilaments, microtubules and intermediate filaments (IFs). The diameter size of 10 nm — intermediate between the diameters of actin microfilaments and microtubules — initially gave IFs their name. However, the structure, dynamics, mechanical properties and functions of IFs are not intermediate but set them apart from actin and microtubules. Because of their nucleotide-independent assembly, the lack of intrinsic polarity, their relative stability and their complex composition, IFs had long been overlooked by cell biologists. Now, the numerous human diseases identified to be associated with IF gene mutations and the accumulating evidence of IF functions in cell and tissue integrity explain the growing attention that is being given to the structural characteristics, dynamics and functions of these filaments. In this Primer, we highlight the growing evidence that has revealed a role for IFs as a key element of the cytoskeleton, providing versatile, tunable, cell-type-specific filamentous networks with unique cytoplasmic and nuclear functions.

### Elucidating IF physiological functions

IFs are generated by a wide variety of proteins encoded by 73 genes in humans. With the exception of nuclear lamins, which are found in all cells of multicellular organisms, the expression of IF proteins, such as keratins, desmin or vimentin, is cell-type specific and also varies during cell differentiation (Figure 1). IF-related diseases affect particular tissues or organs that mostly correspond to the sites of expression of the particular IF proteins. More than 90 pathologies, including the so-called laminopathies, keratinopathies and desminopathies, have been associated with mutations in IF proteins. Mutation of desmin, which is specifically expressed

# Chapter 2: Human formin FHOD3-mediated elongation is required for sarcomere integrity in cardiomyocytes

# Human formin FHOD3-mediated elongation is required for sarcomere integrity in cardiomyocytes

**Dylan A. Valencia**[1,2], **Angela N. Koeberlein**[1,2], **Airi Harui**[3], **Haruko Nakano**[2,4,5], **Akos Rudas**[6], **Cassandra Spencer**[4], **Atsushi Nakano**[2,4,5*], **and Margot E. Quinlan**[1,2*]

[1]*Department of Chemistry and Biochemistry,* [2]*Molecular Biology Institute,* [3]*Divison of Pulmonary & Critical Care Medicine, Geffen School of Medicine,* [4]*Department of Molecular, Cell, and Developmental Biology,* [5]*Eli & Edythe Broad Center of Regenerative Medicine & Stem Cell Research,* [6]*Department of Computational Medicine, University of California Los Angeles, Los Angeles, California, 90095*

*To whom correspondence should be addressed: UCLA Department of Chemistry and Biochemistry, 607 Charles E. Young Dr. E., Los Angeles, California 90095. E-mail: anakano@ucla.edu, margot@chem.ucla.edu

## Abstract

Contractility and cell motility depend on accurately controlled assembly of the actin cytoskeleton. Formins are a group of actin assembly proteins. One family of formins known as Formin HOmology Domain-containing protein (FHOD) is critical to the formation of the fundamental contractile unit, the sarcomere, in cardiomyocytes. Despite our knowledge of FHOD3L's importance in cardiomyocytes, its biochemical and cellular activities remain poorly understood. Contrary to a previous report, we found FHOD3L to nucleate rabbit skeletal muscle actin (RSA) and briefly elongate actin filaments after temporarily pausing elongation. Further, we designed mutants to separate nucleation and elongation activities by FHOD3L. In this study, we have shown that human FHOD3L's elongation ability, but not its nucleation or bundling activity, is necessary for proper sarcomere formation and contractile function in neonatal rat ventricular myocytes (NRVMs). Interestingly, we found that an HCM-associated FHOD3L mutant within a regulatory domain is degraded in NRVMs, while another HCM-associated FHOD3L mutant in the FH2 domain enhances nucleation. The results of this work will contribute to knowledge regarding how cardiomyopathies arise from defects in sarcomere integrity and provide insight into the mechanisms by which formins build specific structures in cardiomyocytes.

Keywords: Formin; Formin Homology Domain-Containing Protein 3 (FHOD3); Sarcomere; Cardiomyocytes; Hypertrophic cardiomyopathy (HCM)

## Introduction

Higher order actin-based structures are the foundation for specific cellular functions and demand precise spatial and temporal coordination. For example, filopodia, stress fibers, and sarcomeres are required for cell migration, adhesion, and contractility, respectively. A plethora of actin binding proteins, such as cofilin, fascin, or profilin, are required to assemble these complex structures by severing filaments, bundling filaments, or inhibiting nucleation of new actin filaments, respectively (Jansen et al., 2011; Okreglak & Drubin, 2007; Pernier et al., 2016; Yamashiro et al., 1998). There are three known classes of actin nucleators that stimulate actin assembly. One such class of actin nucleators known as formins mediates both nucleation and elongation of actin filaments. Formins are defined by the Formin Homology (FH) domains 1 and 2. The FH2 domain is highly conserved and forms a donut-shaped homodimer, which is sufficient to nucleate new filaments. It also remains processively associated with the faster-growing barbed-end of actin filaments, modifying the rate of elongation. The FH1 domain is less conserved and contains proline-rich tracts that can bind profilin-actin heterodimers to aid in elongation of actin filaments (Courtemanche & Pollard, 2012). The regulatory domains for most formins are on either side of these FH domains and an intramolecular interaction leads to autoinhibition (Gould et al., 2011). Both actin assembly strengths and relief of this autoinhibitory interaction differ between formins, enabling them to play distinct cellular roles.

Notably, the Formin HOmology Domain–containing protein (FHOD) family of formins has two mammalian isoforms, FHOD1 and FHOD3. FHOD1 is widely expressed and assembles stress fibers that help with adhesion and motility of various cell types, but, surprisingly, has been shown to be dispensable in cardiomyocytes (Gardberg et al., 2013; Gasteier et al., 2003; Iskratsch, Yu, et al., 2013; Jurmeister et al., 2012; Koka et al., 2003; Sanematsu et al., 2019; Schulze et al., 2014; Takeya et al., 2008). In stark contrast to this, FHOD3 is essential for myofibrillogenesis in cardiac muscle, such that *Fhod3*$^{-/-}$ mice are embryonic lethal by E11.5 (Kan-o, Takeya, Abe, et al., 2012; Taniguchi et al., 2009). FHOD3 has two splice isoforms that we denote as FHOD3S (short, Uniprot isoform 1) and FHOD3L (long, Uniprot isoform 4) (Iskratsch et al., 2010). FHOD3L is predominantly expressed in striated muscle, whereas FHOD3S is more widely expressed (Iskratsch et al., 2010; Kan-o, Takeya, Taniguchi, et al., 2012). In cardiomyocytes, FHOD3L localizes to the sarcomeres in a striated pattern and plays a role in sarcomere assembly and maintenance. The role of FHOD3S is less well understood (Fujimoto et al., 2016; Iskratsch et al., 2010; Kan-o, Takeya, Abe, et al., 2012; Taniguchi et al., 2009). Strikingly, mutations in *FHOD3* have been implicated in 1-2% of hypertrophic cardiomyopathy (HCM) cases, in addition to left ventricular noncompaction (LVNC), dilated cardiomyopathy (DCM), and even progressive high-frequency hearing loss (Arimura et al., 2013; Boussaty et al., 2023; Myasnikov et al., 2022; Ochoa et al., 2018). Moreover, recent clinical studies have shown that the HCM-causative FHOD3 mutations increase the likelihood of cardiovascular death and all-cause death, with the onset of the disease occurring as early as age 4 and as late as age 63 (Vodnjov et al., 2023; G. Wu et al., 2021).

To obtain a more nuanced understanding of FHOD3's role in cardiomyocytes, floxed *Fhod3* mice were used to bypass the embryonic lethality of a *Fhod3* knockout (KO) (Ushijima et al., 2018). Perinatal KO of *Fhod3* in the heart led to lethality at day 10. In contrast, KO of *Fhod3* in the adult heart only mildly impairs cardiac function. These data indicate that FHOD3 is crucial for heart development and suggest a less critical role in maintenance of the adult heart (Ushijima et al., 2018). Furthermore, Fhod3 localization, while striated, is not at either end of actin filaments despite formins typically associating with barbed ends of actin filaments. Instead, a direct interaction between Fhod3 and cardiac myosin-binding protein C (cMyBP-C) is required for proper localization of Fhod3 along the thin actin filaments of sarcomeres. In the absence of cMyBP-C, Fhod3 is mislocalized and cardiac function is compromised, suggesting that the balance between these two proteins is critical for proper heart function in mice (Matsuyama et al., 2018). Moreover, a different group reported that another formin DIAPH1 interacts with Mitofusin-2 (MFN2) to alter the mitochondrial-sarcoplasmic reticulum (SR) distance in cardiomyocytes, thus directly affecting mitochondrial efficiency and cardiac function, which is an example of a different role for formins in cardiomyocytes (Yepuri et al., 2023). Alterations to these mitochondrial-SR dynamics can directly affect calcium transients upstream of the physical contraction of the sarcomere (Eisner et al., 2013; Fernandez-Sanz et al., 2014). Further, rhythmic contractions that are elicited by proper electrical stimuli and calcium transients ensure that the heart delivers oxygenated blood and nutrients throughout the body, reducing the risk of blood clots (Hennis et al., 2024; Neeman-Egozi et al., 2024).

We still lack a mechanistic understanding of FHOD3's role. Although Fhod3 has been extensively studied in cells and *in vivo*, its biochemical properties have not been well studied. Unlike other formins, purified FHOD3L was shown to decelerate, rather than hasten, actin assembly *in vitro* (Taniguchi et al., 2009). A classical mutation in the FH2 domain removes this impact on actin assembly and fails to rescue sarcomere formation when endogenous protein is knocked down. Thus, it has been suggested that FHOD3L is an actin capper (Taniguchi et al., 2009). Likewise, roles other than nucleation, including capping and bundling, have been proposed to be the primary actin assembly activities for FHOD1 (Schonichen et al., 2013). However, we found that *Drosophila* Fhod is a potent actin nucleator and that nucleation by FHOD1 is sensitive to the actin isoform used *in vitro*. Thus, we decided to analyze all four of these actin-related biochemical activities of FHOD3L more closely.

Here, we show for the first time to date that purified human FHOD3L accelerates actin assembly by nucleation and elongation, albeit weakly. We also measure capping and bundling activity. Notably, mammalian formin FHOD1 bundles actin filaments into stress fibers *in vivo* and plays a role in nuclear positioning in cardiomyocytes, with implications in cardiac laminopathy (Antoku et al., 2019; Schonichen et al., 2013; Takeya & Sumimoto, 2003). Using function separating mutations, we link FHOD3L's biochemistry to the structural integrity of the sarcomere within cardiomyocytes. We show that reduced nucleation and bundling by FHOD3L is tolerated in neonatal rat ventricular myocytes (NRVMs), whereas elongation activity is necessary for proper sarcomere formation. Further, we investigate the consequences of two HCM-causative FHOD3L mutations *in vitro* and in NRVMs. Interestingly, we found that both tested HCM-causative mutants lead to reduced contractile function, but only one of which leads to arrhythmia in culture.

## Results

### *Biochemical characterization of human FHOD3*

We purified the C-terminal half of human FHOD3L (FHOD3L-CT), encompassing the FH1 domain, FH2 domain, and C-terminal tail, which is typically sufficient for actin assembly *in vitro* and *in vivo* (**Fig.2-1**, **Fig.2-3A**) (Courtemanche, 2018; Patel et al., 2018). In contrast to earlier reports, we found that FHOD3L-CT enhances rabbit skeletal muscle actin (RSA) assembly in bulk pyrene assays (**Fig.2-2A**) (Taniguchi et al., 2009).

We used rabbit skeletal muscle actin (RSA) throughout the paper, based on FHOD3L's role in skeletal and cardiac muscle. We also asked if the shorter, alternatively spliced FHOD3 isoform, FHOD3S-CT, nucleated actin. FHOD3S-CT, which is 8 residues shorter than FHOD3L-CT, accelerates actin assembly (~33%) more potently than FHOD3L-CT (**Fig.2-2A and B**, **Fig.2-3B**). We then visualized the products of similar reactions using total internal reflection fluorescence (TIRF) microscopy (**Fig.2-2C**). Consistent with nucleation, we observed many more filaments in the presence of FHOD3L-CT compared to actin alone. Thus, we conclude that the C-terminal halves of both FHOD3 isoforms are able to nucleate actin filaments.

To further compare FHOD3L-CT to previously characterized formin mutants, we introduced two mutations in conserved residues of the FH2 domain, I1163A and K1309A, (Xu et al., 2004). Like most formins, the I1163A mutant lacked nucleation activity, while the K1309A mutant reduced nucleation by 78% (**Fig.2-2B**, **Fig.2-4A**) (Xu et al., 2004). We observed a reduction in the plateau with both wild-type FHOD3S/L-CT (we use S/L to indicate both the short and long isoforms of FHOD3) and the I1163A mutant. The decrease was more apparent at higher concentrations of the nucleator and seemed to be dose-dependent (**Fig.2-2A**, **Fig.2-4B**). Control experiments demonstrated that the fluorescence change does not reflect quenching due to side binding or bundling (**Fig.2-4C**). We, therefore, tested for barbed-end binding. We asked whether FHOD3L-CT could inhibit filament elongation by performing bulk seeded-elongation assays. Indeed, we found that FHOD3L-CT potently slows barbed-end elongation ($K_{app}$ = 25.5 ± 5.7 pM; **Fig.2-2D and E**). Barbed-end binding by FHOD3S-CT is ~24-fold weaker ($K_{app}$ = 620 ± 170 pM) (**Fig.2-2E**, **Fig.2-2C**). The isoleucine mutation is generally thought to abolish binding to both actin monomers and filament barbed ends. However, FHOD3L-CT I1163A has an affinity of 21.1 ± 4.2 nM for the barbed ends of actin filaments (**Fig.2-2E**, **Fig.2-4D**). While the affinity is ~1000-fold weaker than wild-type, it still reflects tight binding. Therefore, we interpret the plateau decrease as evidence of barbed-end capping.

To directly observe the impact of FHOD3L-CT on growing actin filaments, we performed TIRF microscopy in the presence of profilin. Most of the filaments elongated at rates indistinguishable from actin alone (**Fig.2-2F and G**). Initially, we could not confirm whether FHOD3L-CT was bound to these filaments. We, therefore, repeated bulk seeded-elongation assays in the presence of profilin. Under these conditions, we observed acceleration of elongation at low doses of FHOD3L-CT (**Fig.2-2F**). However, at higher concentrations, we found that elongation was actually slower than actin alone (**Fig.2-2F**). We attribute the complicated shapes and dose response of these data to the interplay of multiple FHOD3-CT activities-elongation, capping, etc. We also note that the concentrations required for FHOD3L-CT to elicit measurable changes in actin assembly when profilin is present indicate a marked decrease in affinity for the barbed-end under these conditions.

Upon closer observation of individual filaments in the TIRF assay, we detected pauses followed by short “bursts” of faster elongation (**Fig.2-2H**, **Fig.2-3D and E**). During the bursts, the filaments were dimmer and elongated ~3-fold faster, consistent with formin-mediated elongation (**Fig.2-2G and H**, **Fig.2-3E**). The average length of these bursts was 1.10 ± 0.49 $\mu$m, which is similar to the characteristic run length of *Drosophila* Fhod-A (~2 $\mu$m), but very different from many other formins, which commonly range from 20 – 200 $\mu$m (Bremer et al., 2024; Cao et al., 2018; Moseley & Goode, 2005; Patel et al., 2018; Vizcarra et al., 2014) (**Fig.2-2I**). FHOD3S-CT mediated similar behavior with indistinguishable capping duration and velocity, but with significantly briefer bursts (characteristic run length of 0.90 ± 0.33 $\mu$m) (**Fig.2-2G and I**, **Fig.2-3D**). Taken together, FHOD3S/L-CT can cap barbed-ends and also accelerate elongation, both for brief intervals, in the presence of profilin.

Next we investigated bundling by FHOD3S/L-CT. First, we visually examined the organization of phalloidin-stabilized actin filaments after incubating with FHOD3S/L-CT. We observed bundles in both cases, with FHOD3L-CT producing apparently thicker bundles compared to bundles formed by FHOD3S-CT (**Fig.2-3F**). To better quantify bundling activity, we performed low-speed bundling assays with a fixed concentration of actin filaments and several concentrations of FHOD3S/L-CT. Consistent with the difference we observed in bundle size, we found that FHOD3L-CT is a more potent bundler than FHOD3S-CT at concentrations above 15 nM (**Fig.2-3G and H**).

Overall, FHOD3S/L-CT nucleate and elongate actin. FHOD3S-CT is a more potent nucleator, a weaker barbed-end capper, and a slightly weaker bundler compared to FHOD3L-CT (**Table 2-1**). Taken together, these data suggests that the T(D/E)$_5$XE insertion at the end of the last helix in the FH2 domain ($\alpha$T) of FHOD3L-CT that distinguishes it from FHOD3S-CT influences both barbed-end and side binding (**Fig.2-1**).

### *Biochemical validation of function-separating mutants*

We next designed FHOD3L-CT mutants to separate nucleation and elongation and assessed the impact of these mutations on capping and bundling. Previously, Baker et al. identified two mutations in the FH2 domain of Bni1 that diminish nucleation while maintaining elongation (Baker et al., 2015). We tested both in the context of FHOD3L-CT. While FHOD3L-CT E1307N had nearly wild-type nucleation activity, nucleation by FHOD3L-CT K1193L was 71% weaker than wild-type (**Fig.2-5A, Fig.2-6A and B**). The barbed-end affinity of FHOD3L-CT K1193L was 290 $\pm$ 70 pM, ~12-fold weaker than wild-type, but similar to FHOD3L-CT GS-FH1 (**Fig.2-5B, Fig.2-6C**). We then confirmed that K1193L-mediated elongation of actin filaments is similar to wild-type (characteristic run length of 1.11 $\pm$ 0.42 $\mu$m) (**Fig.2-5C and D**). Low-speed bundling assays show that K1193L bundling is ~2-fold weaker than wild-type (**Fig.2-6D and E**).

To abolish elongation, we expressed and purified a C-terminal FHOD3L construct, substituting glycine-serine linkers for the polyproline tracts (Zweifel & Courtemanche, 2020). (The FH2 domain alone was unstable.) We confirmed that elongation was not enhanced by FHOD3L-CT GS-FH1 in the presence of profilin in bulk-seeded elongation assays (**Fig.2-5E**). Pyrene-based actin assembly assays were confounded by bundling/aggregation induced by this mutant. Although low-speed cosedimentation suggests that its bundling strength is slightly weaker than wild-type, images show irregular shapes that may scatter light more (**Fig.2-6E-G**). Thus, to compare the nucleation strength of FHOD3L-CT wild-type to GS-FH1, we used TIRF. We observed similar numbers of filaments generated in the presence of low concentrations (used to minimize bundling) of FHOD3L-CT wild-type or GS-FH1 (**Fig.2-2C**, **Fig.2-5F and G**). Finally, we performed barbed-end elongation assays to compare the barbed-end affinity of FHOD3L-CT GS-FH1 to wild-type and measured a $K_d$ of 300 ± 70 pM in the absence of profilin, ~12-fold weaker than wild-type, and, interestingly, fairly similar in the presence of profilin with a $K_d$ of 201 ± 92 pM (**Fig.2-5B, Fig.2-6H and I, Table 2-1**). Taken together with wild-type FHOD3L-CT's likely weaker affinity for the barbed-end in the presence of profilin, this suggests that profilin binding its FH1 domain may induce a conformational change into a state that is more amenable for formin-mediated elongation.

Together, these mutations provide a good range of nucleation, elongation, capping, and bundling activities (**Table 2-1**). We, therefore, used them to examine whether nucleation and elongation activities are important for the sarcomere formation and maintenance in cardiomyocytes.

### *FHOD3L rescues sarcomere organization and contractility in neonatal rat ventricular myocytes*

In order to perform structure-function analysis in a cellular context, we established methods to knock down and rescue FHOD3L in NRVMs, similar to (Taniguchi et al., 2009) (**Fig.2-7A**). When we knocked down endogenous Fhod3 with "reverse" siRNA transfection, qPCR showed that mRNA levels were reduced by ~65% after four days (**Fig.2-8**). We also observed an ~80% reduction in endogenous Fhod3 protein via Western blot (**Fig.2-7B and C**). To detect sarcomeres, we stained fixed cells with anti-a-actinin. To be able to analyze on a per cell basis, we stained with WGA to segment NRVMs (Stringer et al., 2021)(**Fig.2-9A**). As expected, sarcomeres are largely absent in the mock rescue condition (3 ± 7) with $\alpha$-actinin puncta and aggregates visible by immunofluorescence (IF), compared to mock knockdown NRVMs with more organized sarcomeres (12 ± 13) (**Fig.2-7D and E**)(Taniguchi et al., 2009). We rescued by adenoviral infection four days after siRNA treatment was initiated and examined the cells two days after infection (**Fig.2-7A**). We confirmed that expression of HA-FHOD3L (wild-type) was sufficient to rescue the loss of sarcomeres via IF (19 ± 14) and stained with anti-HA to confirm that exogenous HA-tagged FHOD3L localizes to the sarcomeres (**Fig.2-7D**). In fact, wild-type FHOD3L-rescued NRVMs form significantly more sarcomeres than both the mock knockdown and mock rescue NRVMs (**Fig.2-7D and E**). Thus, we examined protein expression levels and found that exogenous FHOD3L wild-type expression was ~90% above endogenous levels on average at the end of the rescue timeline (**Fig.2-7B and C**). Unfortunately, the DsRed reporter fluorescence was not an accurate readout for exogenous FHOD3L expression levels (**Fig.2-9B**). Therefore, we had to rely on HA levels to quantify the expression of exogenous FHOD3 on a per cell basis. To exclude NRVMs that express too highly above endogenous FHOD3 levels, we set an upper cutoff for the normalized exogenous FHOD3L expression per cell area of 5% and applied that same intensity level as a cutoff for all other experiments (**Fig.2-9C**). Additionally, we set a lower cutoff slightly above background HA levels to exclude NRVMs not expressing exogenous FHOD3L. Given the ~90% higher levels of exogenous FHOD3L on average compared to endogenous Fhod3 in NRVMs, these expression level cutoffs allowed us to analyze NRVMs with FHOD3L levels closer to those of endogenous levels (**Fig.2-7B and C**, **Fig.2-9C**). We acknowledge that the noise in our sarcomere number measurements is likely due to analyzing all NRVMs within these expression level cutoffs that lacked sarcomeres and only a small random sample of NRVMs containing sarcomeres. However, these right-tailed distributions are consistent with other reports of sarcomere numbers per cardiomyocyte (Neininger-Castro et al., 2023). Qualitatively, we found untreated NRVMs to have a similar degree of sarcomere integrity as the mock knockdown and wild-type FHOD3L-rescued NRVMs via IF, but did not measure sarcomere number for that condition (**Fig.2-10A**). Moving forward in this study for the wild-type FHOD3L rescue, we compare our results to mock knockdown NRVMs as the control.

To analyze sarcomere integrity more closely, we measured sarcomere lengths and widths as well as thin filament lengths within sarcomeres. In the FHOD3L wild-type rescue, we found that sarcomere lengths (Z-line to Z-line) (1.72 ± 0.18 μm) and sarcomere widths (Z-line lengths) (1.70 ± 0.46 μm) were recovered to lengths similar to the mock knockdown control (**Fig.2-7F and G**). To measure thin filament length, we stained NRVMs with phalloidin and anti- HA at the end of the rescue. We observed shorter thin filament lengths in wild-type FHOD3L-rescued NRVMs (739 ± 81 nm) compared to mock knockdown NRVMs (925 ± 94 nm). We also examined thin filaments in untreated NRVMs (928 ± 97 nm), which were similar to those in mock knockdown NRVMs (**Fig.2-7H and I**, **Fig.2-10A and B**). All these thin filament length measurements are on par with those from chicken cardiomyocytes, despite being reported to be quite variable between different myofibrils from the same muscle and even within the same sarcomeres (Littlefield & Fowler, 2002; Robinson & Winegrad, 1979). Therefore, wild-type FHOD3L-rescued NRVMs form more sarcomeres *de novo* with slightly shorter thin filaments on average compared to endogenous conditions, perhaps due to higher FHOD3L expression levels.

We also measured contractile function in FHOD3L-rescued NRVMs. To do so, we used the motionGUI MatLab program that makes use of Digital Image Correlation (DIC) to measure contractility (Huebsch et al., 2015; Nakano et al., 2017) (**Fig.2-11A-E**). Contraction and relaxation velocities inform us of systolic and diastolic function of the cardiomyocytes, respectively, and thus their ability to promote proper blood flow in organisms (Ferreira-Martins & Leite-Moreira, 2010). Contraction velocities were indistinguishable in untreated and mock knockdown NRVMs (**Fig.2-12A**). Relaxation velocities were slightly lower in the mock knockdown control compared to untreated (**Fig.2-12B**). Thus, the treatment alone did not noticeably harm contractile function. We found that maximal contraction and relaxation velocities were significantly decreased in knockdown conditions and recovered to mock knockdown levels when FHOD3L was expressed in NRVMs (**Fig.2-11A-E**).

Rhythmic contractions of cardiomyocytes depend on upstream electrical stimuli and calcium transients. Thus, to better understand whether these upstream signals were properly functioning, we also measured the percentage of beating area in each video that exhibited consistent, rhythmic contractions (defined as no more than 1 beat out of sync in a 10 second period). We observed rhythmic contractions for both the mock knockdown NRVMs and wild-type FHOD3L-rescued NRVMs for ~75% of the analyzed videos (**Fig.2-11A, C, and F**). In contrast, arrhythmic contractions were primarily detected in FHOD3-depleted NRVMs, with only ~15% of the videos showing rhythmic beating (**Fig.2-11B and F**). To assess whether some NRVMs in these conditions were not contracting at all, we estimated the proportion of NRVMs that were contracting per video and found contractions throughout ~95% of the field of view on average for both mock knockdown NRVMs and wild-type FHOD3L-rescued NRVMs (**Fig.2-11G**). We observed a slight reduction in contractile area to ~80% for FHOD3-depleted NRVMs (**Fig.2-11G**). We attribute some of the movement to neighboring cells pulling each other. We also quantified contractility when we overexpressed FHOD3L. Contraction and relaxation velocities were moderately reduced in the NRVMs with FHOD3L overexpression, but the area of rhythmic contractions were similar to the mock knockdown NRVMs, suggesting that excessive FHOD3L activity has a mild impact on mechanics and little on calcium handling in NRVMs (**Fig.2-12C-F**). Taken together with the lack of sarcomere organization in the FHOD3-depleted NRVMs, this suggests that proper sarcomere structure directly influences overall cellular organization of the sarcoplasmic reticulum (SR) in NRVMs, thus disrupting calcium dynamics and leading to arrhythmogenicity in the absence of sarcomeres (Eisner et al., 2013; Fernandez-Sanz et al., 2014; Yepuri et al., 2023).

### *FHOD3L elongation activity is required for proper sarcomere formation and cardiac function*

Once we established baseline levels of sarcomere organization and contractility in NRVMs with the FHOD3L wild-type rescue, we asked which actin organizing activities of FHOD3L are important for its *in vivo* function. To this end, we performed rescue experiments with the nucleation-hindering mutant (K1193L) and the elongation-hindering mutant (GS-FH1) in NRVMs. We observed a strong rescue with the K1193L mutant: 15 ± 16 sarcomeres formed per NRVM with proper localization of FHOD3L to sarcomeres (**Fig.2-13A and B**). There was a slight, albeit significant, reduction in sarcomere lengths compared to wild-type (1.65 ± 0.22 vs. 1.72 ± 0.18 μm) (**Fig.2-13C**), but sarcomere widths were indistinguishable from wild-type (1.67 ± 0.41 μm) (**Fig.2-13D**). Thin filament lengths from the K1193L rescued-NRVMs (792 ± 79 nm) were significantly longer than thin filament lengths from the wild-type FHOD3L rescued NRVMs, despite similar exogenous expression levels for each rescue (**Fig.2-13E and F**, **Fig.2-14**). However, we observed shorter thin filament lengths in both the wild-type and K1193L-rescued NRVMs compared to that of mock knockdown NRVMs (**Fig.2-7H and I**, **Fig.2-13F**). This is perhaps due to a byproduct of sarcomere reformation in NRVMs where more sarcomeres are formed per NRVM, but each with shorter thin filaments on average, such that the total F-actin concentration per NRVM is maintained. In agreement with the well-organized, near wild-type appearance of sarcomeres, contraction and relaxation velocities, as well as the proportion of rhythmically contracting NRVMs, were similar to the wild-type rescue (**Fig.2-13G-I, Fig.2-15**). Thus, ~70% loss of nucleation, 10-fold weaker barbed-end capping, and loss of over 50% of bundling activity had minimal impact on FHOD3L function.

In contrast, the GS-FH1 mutant did not rescue FHOD3L loss in NRVMs. The sarcomere number per cell was only 2 ± 4, similar to the mock rescue (**Fig.2-13A and B**). Of the NRVMs that had sarcomeres in the GS-FH1 mutant rescue, only a small fraction had exogenous HA-FHOD3L GS-FH1 properly localized to the sarcomeres as wild-type (**Fig.2-13A, Fig.2-14**). Within the sarcomeres detected, sarcomere lengths and widths were both reduced (**Fig.2-13C and D**). We were not able to confidently measure thin filament lengths, due to the lack of sarcomere organization (**Fig.2-13A and B**). Based on total fluorescence per cell, we determined that FHOD3L GS-FH1 levels were somewhat lower than observed for wild-type or K1193L, despite infecting a similar proportion of NRVMs, suggesting that FHOD3L GS-FH1 turnover may be higher than wild-type (**Fig.2-14**). Not surprisingly, contractility was nearly abolished after rescuing with GS-FH1 (**Fig.2-13G-I**). Contraction and relaxation velocities were decreased and contractions were largely arrhythmic (**Fig.2-13G-I**, **Fig.2-15**). Therefore, elongation activity by FHOD3L is necessary for sarcomere formation, whereas reduced nucleation activity is tolerated. While barbed-end capping and bundling activities were weaker than wild-type in the GS-FH1 mutant, they were equivalent or greater than the activities found for the K1193L mutant which rescued well. Therefore, we conclude that elongation activity of FHOD3L is the primary activity required for sarcomere formation, whereas reduced nucleation, barbed-end binding, and bundling activities are tolerated.

### *FHOD3L hypertrophic cardiomyopathy mutants impact sarcomere formation and function*

Finally, we applied our methodology to investigate mutations causative for HCM (Ochoa et al., 2018). Because it is in the FH2 domain, we first tested the actin assembly activities of the R1386Q mutant in our C-terminal FHOD3L construct. Intriguingly, we found that FHOD3L-CT R1386Q nucleates actin ~37% more potently than wild-type (**Fig.2-16A**). It caps barbed ends (in the absence of profilin) with a $K_d$ that is ~3x weaker than wild-type (83 ± 22 pM) (**Fig.2-16B**, **Fig.2-17A**). Enhancement of elongation was indistinguishable from wild type, with short, accelerated runs (**Fig.2-17B and C**). We observed a slight, but significant, increase in the capping duration before these bursts (**Fig.2-16C**). Finally, we detect no change in bundling activity (**Fig.2-17D and E**).

Therefore, the R1386Q mutation in the FH2 domain primarily improves nucleation strength while maintaining all other actin assembly activities relative to wild-type.

We then asked if a cellular phenotype can be observed by replacing FHOD3L with the R1386Q mutant in NRVMs. When FHOD3L R1386Q was the rescue construct, we observed fewer sarcomeres per NRVM (9 ± 13) compared to the wild-type rescue (**Fig.2-18A and B**). As expected, the R1386Q mutant localized to the sarcomeres, but upon closer inspection with line scans through the myofibrils, we found that it localizes closer to the Z-lines, compared to wild-type (**Fig.2-18C and D**, **Fig.2-19A and B**). The sarcomeres were significantly thinner (1.34 ± 0.30 µm) but with similar sarcomere lengths (1.72 ± 0.20 µm), compared to the wild-type rescue (**Fig.2-18E and F**). We found that FHOD3L R1386Q-rescued NRVMs had significantly longer thin filaments (813 ± 83 nm) compared to the wild-type rescue, possibly due to compensation for having thinner sarcomeres (shorter Z-lines) (**Fig.2-18G and H**). Given the shift in R1386Q localization and longer thin filaments relative to wild-type, HA-FHOD3L R1386Q appears to be further away from the pointed ends of the thin actin filaments compared to wild-type. In functional assays, we observed contraction and relaxation velocities significantly weaker than those of the wild-type rescue, but the proportion of contractile area and rhythmic contractions were on par with the wild-type rescue (**Fig.2-18I and J**, **Fig.2-20A and B**). Thus, an increase in nucleation activity appears to be detrimental.

Finally, we were intrigued by a mutational hotspot in patients with HCM at arginine 637 and nearby residues (Ochoa et al., 2018). This location is far removed from the C-terminal half of FHOD3L, which mediates actin assembly, or the regulatory

DID domain (Iskratsch, Reijntjes, et al., 2013). Therefore, we did not perform biochemical analysis. Instead, based on prediction of the greatest structural disruption (RaptorX) we selected and analyzed the consequences of replacing FHOD3L with the R637P mutant. We observed significantly fewer sarcomeres per NRVM (6 ± 9) compared to the wild-type rescue (**Fig.2-18A and B**). Interestingly, we did not observe any enrichment of the R637P mutant in sarcomeres (**Fig.2-18A**). Western blots revealed that exogenous FHOD3L R637P protein levels are ~75% of wildtype exogenous FHOD3L, consistent with single-cell measurements of exogenous HA-FHOD3L R1386Q levels being slightly above background (**Fig.2-18K and L**, **Fig.2-20C**). In addition to reduced sarcomere number, we found slightly shorter sarcomere lengths (1.54 ± 0.32 μm) and sarcomere widths (1.48 ± 0.42 μm) in R637P-rescued NRVMs (**Fig.2-18A-B,E, and F**). Moreover, we observed a reduction in contraction and relaxation velocities as well as a notable reduction in rhythmic contractions by R637P-rescued NRVMs (**Fig.2-18I and J**, **Fig.2-20A and B**). Thus, a point mutation in an apparently sensitive region of FHOD3L, with no known function, had strong impact on NRVMs.

## Discussion

Here, we show that mammalian formin FHOD3L's unique ability of pausing elongation before brief, rapid enhancement is necessary for proper sarcomere formation and contractile function in NRVMs. FHOD3L likely elongates stress-fiber like filaments to specific lengths in pre-myofibrils near the membrane of cardiomyocytes as sarcomerogenesis has been shown to occur in a retrograde fashion away from the cell edge (Fenix et al., 2018; Fujimoto et al., 2016; Ono, 2010; Rhee et al., 1994; Sanger et al., 2005; Dlugosz et al., 1984). However, other formins, like Daam1, and other actin binding proteins at the pointed and barbed ends, such as Leiomodin and CapZ, respectively, may still be important for precisely tuned thin actin filament lengths in NRVMs (Ajima et al., 2015; Farkas et al., 2024; Papa et al., 1999; Pappas et al., 2008; Szikora et al., 2022). Structural insights into FHOD3L's interactions at the barbed-end may be informative to its mechanism for elongation during early stages of sarcomere formation. Given the ~25 pM affinity for FHOD3L within the same order of magnitude as capping protein (CP) at 60-100 pM, FHOD3L can cap filaments and be filtered off size-exclusion chromatography to then perform CryoEM for structural determination, as was successfully done with CP, and more recently, multiple formins (Funk et al., 2021; Oosterheert et al., 2024; Wear et al., 2003). Particularly, structural determination of FHOD3L at the barbed-end of actin filaments can inform us if FHOD3L's FH2 domain samples multiple conformations, which could possibly explain how it "prepares" for brief bursts of elongation in the presence of profilin. Further, since the activity of Sarcomere Length Short protein (SALS), the *Drosophila* ortholog of mammalian Leiomodin-2 (LMOD2), has been shown to be formin-dependent and FHOD3L localizes near the pointed ends in mature sarcomeres, it's possible that FHOD3L also helps indirectly maintain thin filament lengths with LMOD2 as actin monomers at the pointed ends are recycled with the help of cofilin-2 or adenylyl cyclase-associated protein 2 (CAP2) during active contractions (Colpan et al., 2021; Ehler, 2018; Farkas et al., 2024; Skwarek-Maruszewska et al., 2009; Tolkatchev et al., 2020).

FHOD3L K1193L successfully rescued sarcomere formation and contractile function despite reduced nucleation and bundling activity observed *in vitro*. This observation is consistent with the findings from previous knockout mouse studies: Deletion of *Fhod3* in germ-line or at perinatal stages is lethal, while deletion at adult stages only mildly hinders cardiac function (Kan-o, Takeya, Abe, et al., 2012; Taniguchi et al., 2009; Ushijima et al., 2018). This is possibly because another formin, such as DAAM1 or DIAPH1, compensates for the primary nucleation role in cardiomyocytes, whereas bundling activity could be highly regulated as thick actin bundles are embryonic lethal in cardiomyocytes (Ajima et al., 2015; Li et al., 2011; O'Shea et al., 2017; Rosado et al., 2014; T. Wu et al., 2017). Interestingly, despite reduced nucleation activity by FHOD3L being tolerated in NRVMs, we still observed a nonsignificant reduction in sarcomere number per NRVM and a slight, nonsignificant reduction in sarcomere widths from the K1193L mutant rescue compared to wild-type, suggesting that FHOD3L's nucleation strength partially contributes to sarcomere formation and width at the Z-lines (**Table 2-2**). We cannot rule out the potential importance for barbed-end binding affinity of FHOD3L for sarcomere formation and maintenance as both function-separating mutants still tightly bound muscle actin barbed-ends with picomolar affinity, ~10-fold weaker than wild-type (**Table 2-1**). Upon FHOD3 knockdown, the sarcomere structure is largely disrupted in most cardiomyocytes, and this diffuse $\alpha$-actinin distribution could lead to its ubiquitination and degradation, thus initiating a negative feedback loop for total $\alpha$-actinin content (Solís et al., 2023). Consistent with this reduction in total $\alpha$-actinin protein levels, it follows that sarcomere number or sarcomere width at the Z-line could potentially be reduced. This phenomenon could explain the longer thin filaments from the K1193L and R1386Q mutant rescues compared to the wild-type rescue because of thin actin filament elongation being compensated for reduced sarcomere formation.

We observe no localization of exogenous FHOD3L in most NRVMs when sarcomeres are largely absent, consistent with cMyBP-C requiring the presence of sarcomeres for proper FHOD3L localization (Matsuyama et al., 2018). The lack of FHOD3L localization to the sarcomeres seems to consistently lead to arrhythmogenicity in the NRVMs, such as from the GS-FH1 and R637P rescues, suggesting that its localization is important for maintaining mitochondrial energetics and calcium handling. A recent study found that DIAPH1 interacts with MFN2 to regulate the tethering of mitochondrial-sarcoplasmic reticulum (mito-SR) in cardiomyocytes (Yepuri et al., 2023). It remains to be observed exactly how FHOD3L mutations impact the electrophysiology and calcium transients in cardiomyocytes. FHOD3L is required for both proper sarcomere formation and cardiomyocyte function in NRVMs. However, conditional FHOD3 KO's in the adult mouse heart only mildly impaired cardiac function and maintained sarcomere integrity (Ushijima et al., 2018). Therefore, there seems to be a stage-specific requirement of FHOD3 in the heart. Moreover, it remains to be seen whether the distribution of sarcomere gene transcripts, such as *MYH6* and *MYH7*, fail to properly localize upon FHOD3 knockdown via fluorescent *in situ* hybridization (FISH) and/or if the transcriptional levels change in the NRVMs via qPCR since microtubule-based transport of mRNAs, as well as their downstream translation and degradation, all occur locally along the Z-lines of sarcomeres (Bogdanov et al., 2021; Denes et al., 2021; Lewis et al., 2018; Scarborough et al., 2021). This potential phenomenon could result in a negative feedback loop for reduced sarcomere integrity and cardiac function, which may become less severe as development occurs.

FHOD3 was first linked to HCM in a genome-wide association study (GWAS) in 2013 (Wooten et al., 2013) and one of the two strongest signals for HCM in the larger GWAS (Tadros et al., 2021). Although the number of HCM-causing FHOD3 mutations continues to grow, the molecular characteristics of these mutations are poorly understood. We studied two FHOD3L mutants causative for HCM here in rescue experiments in NRVMs and acknowledge that the observed phenotypes are more extreme than what would likely be observed at a molecular level in human patients given that our knockdown approach results in an ~80% decrease in the FHOD3 protein level whereas most HCM-causing mutations in humans are heterozygous mutations (Ochoa et al., 2018; van Rijsingen et al., 2009; Wessels et al., 2015; Yuan et al., 2023). Consistent with other HCM models, we observed deficits in sarcomere contraction and relaxation for both FHOD3L R637P and R1386Q-rescued NRVMs (Garfinkel et al., 2018), although it needs to be validated whether or not our *in vitro* parameters accurately reflect contractile and relaxation functions of the heart. The instability and degradation of FHOD3L R637P may be due to protein misfolding in the N-terminus containing the binding interface for cMyBP-C, resulting in diffuse localization of FHOD3L (Matsuyama et al., 2018). The protein instability would potentially be seen with other likely pathogenic HCM FHOD3L mutants in the N-terminal regulatory domains. Moreover, FHOD3L R1386Q localizes slightly differently than wild-type, where it is closer to, but not at, the barbed-end of thin actin filaments, suggesting that it interacts differently with cMyBP-C and thus gets localized further towards the Z-line than wild-type does. Due to improved capping ability for FHOD3L-CT R1386Q in the presence of profilin compared to wild-type, we think this can also factor into its altered localization, possibly being displaced by CapZ at the barbed-end towards the end of sarcomerogenesis, thus forcing it to bind the sides of thin actin filaments closer to the Z-lines without the help of cMyBP-C.

Many intriguing questions remain to be tested. Why is a nucleation-hindering mutant tolerated in NRVMs? Is it also tolerated in immature fetal-type cardiomyocytes? What phenotypes would be observed from these different FHOD3L rescues if performed in human cardiomyocytes? The rescue workflow that we established here in NRVMs allows for structural assessment of the sarcomere components as well as functional assessment of contractility and calcium transients and can easily be applied to more immature cardiomyocytes to gain more insight into earlier developmental stages of myofibrillogenesis.

## Materials and Methods

### *Protein expression, purification, and labeling*

Wild-type FHOD3L C-terminal (FHOD3L-CT) 963-1622 (spanning the FH1 domain, FH2 domain, and tail) was cloned into a modified version of the pGEX plasmid with an N-terminal glutathione-S-transferase (GST) tag. Point mutations were generated by site-directed mutagenesis as described (Liu & Naismith, 2008). pGEX-FHOD3L-CT GS-FH1 963-1622 where the polyproline tracts were replaced with GS linkers was cloned via Gibson Assembly using pGEX-FHOD3L-CT 963-1622 and a gBlock as templates. The FHOD3L-CT wild-type and mutant constructs were transformed in

Rosetta 2 (DE3) cells (Novagen), which were grown in 1 liter of Terrific Broth supplemented with 100 mg/liter ampicillin and 32 mg/liter chloramphenicol. Expression was induced at an OD of 0.6-0.8 by adding 0.5 mM isopropyl β-D-1-thiogalactopyranoside (IPTG) and shaking overnight at 18°C, 210 rpm. The cells were harvested by centrifugation, washed in PBS, and flash frozen in liquid nitrogen.

Cell pellets expressing GST-FHOD3L-CT wild-type and mutants from *E. coli* were resuspended in 20 mM HEPES pH 7.5, 150 mM NaCl, 1 mM PMSF, 1 mM DTT, 2 µg/mL DNaseI. All subsequent steps were performed on ice or at 4°C. The cells were lysed by microfluidizing, cleared by centrifugation at 20,000 x g for 20 minutes, and then purified using a HitrapSP-FF cation exchange column (GE Life Sciences) with a gradient of 0.2 –0.6 M NaCl over 1 column volume after 1 column volume of washing at 0.2 M NaCl. Peak fractions were dialyzed overnight into 20 mM HEPES pH 8, 200 mM NaCl, 1 mM DTT to cut off the GST with prescission protease, centrifuged at 4°C for 48,000 rpm for 20 minutes, and further purified on a MonoS cation exchange column (GE Life Sciences) with a gradient of 0.2–0.95 M NaCl over 40 column volumes after 1 column volume of washing at 0.2 M NaCl. Peak fractions were exchanged into storage buffer (10 mM Tris pH 8, 150 mM NaCl, 20% glycerol, 1 mM DTT), then flash frozen in liquid nitrogen and stored at -80°C.

Cell pellets expressing GST-FHOD3S-CT wild-type from *E. coli* were purified and stored similarly as GST-FHOD3L-CT wild-type, except 150 mM NaCl was used throughout the entire purification with a gradient of 0.15–0.95 M NaCl over 40 column volumes after 1 column volume of washing at 0.15 M NaCl on the MonoS cation exchange column (GE Life Sciences).

Cell pellets expressing Human Profilin-1 were resuspended in 10 mM Tris pH 8, 1 mM EDTA, 1 mM PMSF, and 1 mM DTT. All subsequent steps were performed on ice or at 4°C. The cells were lysed and clarified as above. The resulting clarified lysate was filtered through DEAE resin after nutating together for 30 minutes. The flowthrough was subjected to a 35% ammonium sulfate cut. The mixture was allowed to equilibrate 15-20 minutes and then spun down 30,000 x g for 30 minutes. Then a 61% ammonium sulfate cut was taken from the clarified supernatant and allowed to stir for 20 minutes. This mixture was then spun down 30,000 x g for 30 minutes. The resulting pellet was taken and resuspended in 10 mL of 5 mM potassium phosphate pH 7.5, 1 mM DTT and nutated for 30 minutes. The protein mixture was dialyzed in 1 L 5 mM potassium phosphate pH 7.5, 1 mM DTT for two 2-hour blocks followed by overnight with buffer changes in between. The following day, dialysate was spun down at 20,000 x g for 20 minutes and the clarified supernatant was loaded onto the HA column for filtration using 8 CV of 5 mM potassium phosphate pH 7.5, 1 mM DTT and 5 CV of 500 mM potassium phosphate pH 7.5, 1 mM DTT. Using 1 mL fractions, the protein was in the flow through and first five fractions of the first wash. NaCl was added to 150 mM final before spin concentrating sample down to 11 mL to dialyze overnight in 10 mM HEPES pH 7, 150 mM NaCl. The following day, sample was clarified by spinning 56,000 rpm for 30 minutes and loaded onto the S75 gel filtration column, running it at 1 mL/min with 1 mL fractions for 1.2 CV. Samples were dialyzed into 10 mM HEPES pH 7, 0.5 mM TCEP.

Concentrations of C-terminal FHOD3 constructs were determined by running a series of serial dilutions on a Sypro Red-stained quantitative gel using densitometry (ImageJ) with rabbit skeletal actin as the standard. Gels stained with Sypro Red at room temperature for 1 h, shaking at 60 rpm in 10% acetic acid and rinsed briefly with 10% acetic acid before scanning on a Molecular Imager PharosFX Plus (Bio-Rad). All FHOD3L-CT concentrations are reported as dimer concentrations.

Protein concentrations for Profilin-1 were calculated using Beer's law: $A = \varepsilon bc$ where A is the absorbance at 280 nm, $\varepsilon$ is the extinction coefficient, b is the path length (1 cm), and c is the concentration. Profilin-1 concentration was determined above with extinction coefficient 14,992 $M^{-1}$ $cm^{-1}$.

Skeletal muscle actin was isolated from rabbit back muscle acetone powder (Pel-Freez) according to the method described by Spudich and Watt with modifications (Spudich & Watt, 1971). Skeletal muscle actin was labeled with pyrene iodoacetamide (Thermo Scientific) or Alexa Fluor 488 NHS-ester (Thermo Scientific) as described with modifications (Sun et al., 2018). *Schizosaccharomyces pombe* profilin was purified as described (Harris et al., 2004).

### *Pyrene Assays*

Pyrene assays were performed essentially as described (Bor et al., 2012) on an Infinite 200 Pro plate reader (Tecan). In all assays, FHOD3L-CT was diluted in G-actin buffer before addition to polymerization buffer to improve stability. For bulk pyrene assays, nucleation strengths were calculated from the slope at $t_{1/8}$ through the origin. The concentration of barbed ends was calculated from the slope (obtained by linear regression over 90 s) as described in (Pollard, 1986 and Patel et al., 2018). For seeded elongation assays, actin filaments were sheared by passing three times through a 24-gauge needle and then aliquoted into each well of a microplate. Proteins were added to the seeds and incubated for 2–4 min at room temperature. Seeds and additional proteins in KMEH (10mM HEPES, pH 7, 1mM EGTA, 50 mM KCl, 1 mM $MgCl_2$) were added to magnesium-actin to initiate actin elongation. Elongation rates were determined by linear regression over the first 90 s and normalized against the rate of actin alone in each experiment. The affinity of FHOD3-CT for barbed ends was determined by fitting the data to the quadratic binding equation $r = a + \mathrm{b} * ((\mathrm{[barbed\ ends]} + \mathrm{[FHOD3-CT]} + K_d) - \sqrt{(\mathrm{[barbed\ ends]} + \mathrm{[FHOD3-CT]} + K_d)^2 - 4 * \mathrm{[barbed\ ends]} * \mathrm{[FHOD3-CT]}})$, where *r* is the normalized elongation rate and *a* and *b* are constants.

### *Low Speed Bundling Assays*

10 $\mu$M F-actin was polymerized for 1 hour at room temperature and diluted to 5 $\mu$M with varying amounts of FHOD3-CT constructs diluted in 1X KMEH (10mM HEPES, pH 7, 1mM EGTA, 50 mM KCl, 1 mM MgCl2) for 30 min., room temperature and then spun 20 min., 14,000 x g to separate the pellet and supernatant. The supernatant samples were carefully transferred to new tubes and the pellet samples were resuspended in an equal volume of 1X sample loading buffer for quantitative comparison. Samples were boiled in 1X sample loading buffer for 10 minutes and run on 10% SDS-PAGE gels. The percentage of actin pelleted was determined via densitometry on FIJI.

### *TIRF Microscopy*

TIRF microscopy was utilized to measure the elongation rates and run lengths of the FHOD3-CT constructs. Coverslips were rinsed three times in MilliQ water, placed in 2% Hellmanex (Hellma Analytics) at 60–65 °C for 2 h, and rinsed another five times in MilliQ water. Once dry, the slips were used for the elongation experiments.

Flow chambers of ~15 $\mu$l were assembled on the slide using strips of double-sided tape. Flow chambers were prepared with the following steps: 1) block with 20 $\mu$l of high-salt buffer (50 mM Tris pH 7.5, 600 mM NaCl) for 2 min; 2) 12.5 $\mu$l of 60 nM NEM-myosin; 3) 20 $\mu$l of high-salt BSA-containing buffer (1% BSA, 50 mM Tris pH 7.5, 600 mM NaCl); 4) 20 $\mu$l of low-salt BSA-containing buffer (1% BSA, 50 mM Tris pH 7.5, 150 mM NaCl). 5) 50 $\mu$l of magnesium-actin and additional proteins to be assayed for a final concentration of 1 $\mu$M G-actin (10% Alexa Fluor 488-labeled) and 5 $\mu$M human Profilin-1 in 1X TIRF buffer supplemented with 250 $\mu$g/ml glucose oxidase and 50 $\mu$g/ml catalase. Bright and dim filaments were distinguished manually in the presence of formin.

The videos and images were acquired using a Zeiss Axio Observer 7 Basic Marianas Microscope with Definite Focus 2 equipped with a 3i Vector TIRF System, an Alpha Plan-Apochromat 63x (1.46 NA) Oil TIRF Objective, and an Andor iXon3 897 512x512 10 MHz EMCCD Camera, using Slidebook 6 software. Experiments were performed at room temperature. Images were captured at 2.5-s intervals for 10 min. Filament lengths were quantified with the JFilament plug-in in FIJI.

### *Adenoviral generation, purification, and infection*

Adenoviruses containing a full-length FHOD3L wild-type construct were generated by transiently transfecting HEK293 cells using the CalPhos Mammalian

Transfection Kit (Catalog No. 631312, Takara Bio) separately with pAdenoX-CMV-3xHA-FHOD3L-CMV-DsRed wild-type after digesting with PacI (NEB) in Cutsmart buffer (NEB) for 1 hr at 37 °C. All HEK293 cultures were cultured in 1X DMEM (Thermo Fisher, Catalog No. 11965092), 10% FBS (Thermo Fisher, Catalog No. 10082147), and 1% penicillin/streptomycin/amphotericin B (Thermo Fisher, Catalog No. 15240096). HEK293 cells were lysed 7-10 days later when noticeable cytopathic effect (CPE) was present and spun down at 1.5k x g for 5 min., RT. All infections described were performed in PBS with magnesium chloride and calcium chloride (PBS+/+) (Thermo Fisher, Catalog No. 14040117) for 1 hr at room temperature, rotating the plate every 10-15 minutes. Additional crude adenovirus was harvested after infecting multiple 6 cm dishes of HEK293. All dilutions of adenovirus were made in PBS+/+ (Thermo Fisher, Catalog No. 14040117). Plaque formation assays were then performed as in (Baer & Kehn-Hall, 2014). Individual viral plaques were then collected with a P1000 tip to isolate adenoviral clones of full-length FHOD3L wild-type constructs. Clone variability was assessed by infecting HEK 293 for each adenoviral clone and observing subsequent DsRed expression over time. Optimal adenoviral clones were picked and scaled up for large-scale purification. 5 15 cm dishes of HEK293 were infected, then collected 2-3 days later for purification with the Adeno-X Maxi Purification kit (Takara Bio, Catalog No. 631533), following their protocol for the purification steps after infection.

Crude adenoviruses containing pAV-CMV-{3xHA-FHOD3L R637P}:SV40 pA-CMV-mCherry, pAV-CMV-{3xHA-FHOD3L GS-FH1}:SV40 pA-CMV-mCherry, and pAV-CMV-{3xHA-FHOD3L K1193L}:SV40 pA-CMV-mCherry were commercially generated and purchased from VectorBuilder. The amount of crude adenovirus was estimated as mentioned previously and then used to infect 5 15 cm dishes of HEK293 for 1 hr at room temperature and collected 2-3 days later for purification with the Adeno-X Maxi Purification kit (Takara Bio, Catalog No. 631533), following their protocol for the purification steps after infection. pAdenoX-CMV-3xHA-FHOD3L R1386Q-CMV-DsRed was cloned and then sent to VectorBuilder for adenoviral generation and purification. Particle titers of all purified viruses were quantified by making three separate dilutions of each virus in 0.1% SDS (Thermo Fisher) and vortexing for 5 minutes, spinning down 13,000 x rpm, 5 minutes, and then taking the average of the absorbance readings on the Nanophotometer N50-GO (Implen) to quantify particles/mL as per (Maizel et al., 1968).

### *Neonatal rat ventricular myocyte seeding, siRNA knockdown, and rescue*

Neonatal rat ventricular myocytes (NRVMs) were seeded in 8-well chamber slides (Corning, Catalog No. 354118) at 175,000 NRVMs/well upon reverse transfection of siRNA targeting FHOD3 (Qiagen, Rn_LOC100360334_2 Flexitube siRNA) and AllStars Negative Control siRNA (Qiagen, 20 nmol) using Lipofectamine RNAiMAX transfection reagent (Thermo Fisher, Catalog No. 13778075) and Opti-MEM I Reduced Serum Medium (Thermo Fisher, Catalog No. 31985062) to dilute the siRNA. NRVMs were seeded in a mixture of 75% DMEM (Thermo Fisher, Catalog No. 11965092), 15% Medium-199 (Thermo Fisher, Catalog No. 11150059) supplemented with 2 mM L-glutamine (Thermo Fisher, Catalog No. A2916801) and 10 mM HEPES (Thermo Fisher, Catalog No. 15630080). Media was changed 24 hours later to one containing penicillin/streptomycin (Thermo Fisher, Catalog No. 15140122). NRVMs were infected with adenovirus as above 48 hours after reverse transfection and media containing penicillin/streptomycin was added on top of the PBS+/+ at the end of the infection. Media was changed 24 hours later.

*Gene expression analysis by quantitative reverse-transcriptase PCR*

RNA was extracted from the NRVMs four days after reverse transfection of siRNA using the Direct-zol RNA mini prep kit (Zymo Research, Catalog No. R2050). RNA was reverse-transcribed into complementary DNA using the qScript cDNA synthesis kit (Quanta Biosciences, Catalog No. 95047-025). Quantitative reverse-transcriptase PCR was performed using PowerUp SYBR green master mix for qPCR (Applied Biosystems, Catalog No. A25742) on a Lightcycler 480 (Roche). In Figure 3—figure supplement 1A, each well of NRVMs is triplicated for each qPCR reaction. Forward and reverse primer sequences are as follows: GAPDH forward, CCGCATCTTCTTGTGCAGTG; GAPDH reverse, CGATACGGCCAAATCCGTTC; FHOD3 forward, CAGCCAATCACGGAG; FHOD3 reverse, TGCTGTCCTTGCCCTGA.

*Western blots*

NRVMs were lysed in 100 mM Tris pH 8, 150 mM NaCl, 0.5% Triton-X from 8-well chamber slides (Corning, Catalog No. 354118) after rescue experiments and samples were vortexed for 1 minute before centrifuging at 15,000 rpm, 4°C, for 10 minutes. The resulting supernatant was boiled in sample loading buffer at 100°C for 10 minutes and then run on an SDS-PAGE gel. The gel was then transferred to an Immobilon-FL polyvinylidene fluoride membrane (Millipore, IPFL00010) at 100V for 90 minutes on ice. The membrane was blocked in 4% milk in low-salt TBST (20 mM Tris pH 7.6, 150 mM NaCl, 0.05% Tween-20, 0.01% sodium azide) for 30 minutes at room temperature and then blotted with Fhod3 polyclonal rabbit (Abcam, ab224463) or HA monoclonal rabbit (Cell Signaling Technologies, 3724S) and GAPDH monoclonal mouse (Santa Cruz Biotechnology, sc-365062) diluted 1:1000 in low-salt TBST, rotating in 4°C overnight. Membranes were washed 3 times for 5 minutes each the next day in high-salt TBST (20 mM Tris pH 7.6, 500 mM NaCl, 0.05% Tween-20, 0.01% sodium azide) and then incubated with 800CW goat anti-rabbit IgG secondary antibody (Li-Cor Biosciences, 926-32211) and 680RD goat anti-mouse IgG secondary antibody (Li-Cor Biosciences, 926-68070) diluted 1:10,000 in high-salt TBST for 1 hour at room temperature, shaking. Membranes were finally washed 3 times for 10 minutes each in high-salt TBST and then imaged on a Li-Cor Odyssey 9120 Infrared Imager (Li-Cor Biosciences).

### *In vitro contractility assay*

Contractility assessments were performed by utilizing a video-based technique with the UCSF Gladstone-developed MATLAB program MotionGUI (Huebsch et al., 2015). The videos were converted from ome.tif to a tiff stack on FIJI. A pixel size of 0.538 μm was obtained from the metadata and used for all contractility assessments. 8 pixel macroblocks were used for all contractility assessments. Motion vectors were calculated, and the data were evaluated upon completion. All samples were subjected to the same post-processing procedures to ensure consistency during comparative analysis. Each video sample was post-processed using neighbor-based cleaning with the vector-based cleaning criterion within the program. The threshold for this post-processing method was set to two for all samples and was adequate for improving the signal-to-noise ratio enough to identify peaks clearly corresponding to beating events in most samples. All other parameters of the MotionGUI program not outlined here were set to their respective default values. Videos for contractility analysis were taken on a Leica SD AF Spinning Disc system using a HC PL Fluotar 10x (0.3 NA) dry objective lens with an ORCA-Flash4.0 LT C11440 camera (Hamamatsu) at 30 fps with live NRVMs incubated at 37°C, 5% $CO_2$ (Tokai Hit). Videos were acquired using the MicroManager software.

*Immunofluorescence and image analysis*

For sarcomere integrity analysis, NRVMs were stained live with Wheat Germ Agglutinin (WGA) TMR (Thermo Fisher, Catalog No. W849) for subsequent CellPose (Stringer et al., 2021) segmentation before fixation for 10 minutes at 37°C with 5 $\mu$g/mL WGA, followed by two PBS washes. NRVMs were then fixed with 4% paraformaldehyde (Fisher Scientific, Catalog No. AC416780010) in PBS for 15 minutes at 37°C. Cells were then washed 3 times in PBS for 5 minutes each at room temperature. Cells were permeabilized and blocked with PBS/0.1% Triton-X/10% Goat Serum for 30 minutes at 37°C. $\alpha$-actinin (mouse) primary antibody (Sigma, Catalog No. A7811) was diluted 1:250 in PBS/0.1% Triton-X/5% Goat Serum (Triton-X: Thermo Fisher, Catalog No. A16046.AP; Goat Serum: Sigma, Catalog No. S26-100ML) and incubated overnight at 4°C. HA-tag (rabbit) primary antibody (Cell Signaling, Catalog No. 3724) was diluted 1:500 in PBS/0.1% Triton-X/5% Goat Serum and incubated overnight at 4°C. Cells were washed 3 times for 5 minutes each with PBS/0.1% Triton-X/5% Goat Serum at room temperature and then incubated with either Alexa Fluor 488 goat anti-mouse secondary (Thermo Fisher, Catalog No. A-11001) or Alexa Fluor 647 goat anti-rabbit secondary (Thermo Fisher, Catalog No. A-21244) diluted 1:500 in PBS/0.1% Triton-X/5% Goat Serum for 1 hour at 37°C. Cells were then washed twice in PBS/0.1% Triton-X/5% Goat Serum for 5 minutes each and then with PBS for 5 minutes before mounting in Vectashield Plus Antifade mounting media (Vector Laboratories, Catalog No. H-1900-10) with 1 μg/mL DAPI (Fisher Scientific, Catalog No. EN62248).

For thin filament determination, NRVM's were incubated with sterile-filtered Ringer's relaxation buffer (6 mM potassium phosphate pH 7.0, 100 mM NaCl, 2 mM KCl, 0.1% glucose, 2 mM $MgCl_2$, 1 mM EGTA) for 20 min., room temperature, followed by a brief PBS wash to start the WGA staining. Fixation and blocking were performed as above. HA-tag (rabbit) primary antibody (Cell Signaling, Catalog No. 3724) was diluted 1:250 in PBS/0.1% Triton-X/5% Goat Serum and incubated overnight at 4°C. Cells were briefly washed with PBS/0.1% Triton-X/5% Goat Serum twice and then incubated with Alexa Fluor 647 goat anti-rabbit secondary (Thermo Fisher, Catalog No. A-21244) diluted 1:500 in PBS/0.1% Triton-X/5% Goat Serum for 1 hour at 37°C. Cells were then washed twice in PBS/0.1% Triton-X/5% Goat Serum for 5 minutes each and then 200 nM Alexa Fluor 488 phalloidin (Thermo Fisher, Catalog No. A12379) was incubated for 1 hr, room temperature in PBS/1% BSA. Cells were washed with PBS twice for 5 minutes before mounting in Prolong Glass Antifade mountant (Thermo Fisher, Catalog No. P36980) with 1 μg/mL DAPI (Fisher Scientific, Catalog No. EN62248).

A random sample of 12 40X magnification images per biological replicate were taken from a random coordinate generator (https://onlineintegertools.com/generate-integer-pairs) excluding the edges of the wells for quantification of sarcomeres and thin filaments. Each well was treated as a 16x16 grid of 40X magnification fields of view. 16-bit images were acquired on an AXIO Imager.D1 fluorescence phase contrast microscope (Zeiss) using an EC Plan-Neofluar 40x M27 (0.75 NA) objective lens with an AxioCam MRm camera (Zeiss). Images of NRVMs in figures 3-6 were taken on a Plan-Apochromat oil DIC M27 63x (1.4 NA) objective lens for visualization.

Images showing DsRed reporter fluorescence at the end of the rescue timeline for the NRVMs were taken on a CKX53 inverted phase contrast microscope (Olympus) using a UPLFLN 4x (0.2 NA) objective lens (Olympus) with an ORCA-spark digital CMOS camera (Hamamatsu).

Cells were segmented using Cellpose (Stringer et al., 2021). Two-color images of the WGA membrane stain and nuclear stain were saved as jpeg files on FIJI. These images were then input to the Cellpose environment for batch processing with a cell diameter of 210 pixels, 0.4 cell probability and flow thresholds, 0 stitch threshold, and using the cyto2 model for segmentation. The text files of the outlines were saved and overlaid on the respective channels of the images individually using the provided python file from Cellpose as a macros through FIJI (imagej_roi_converter.py). Single cell analysis was performed and corresponded to the cell number output.

Sarcomere analysis was performed manually in a single-blind manner (for mock knockdown, mock rescue, wild-type rescue, and the K1193L rescue) using blindrename.pl to blind the filenames and generate a key filename csv file for decoding files after analysis was complete. We attempted to blind all other rescue conditions, but they were too easily distinguishable due to expression level and localization differences. Linescans were generated along myofibrils, perpendicular to the Z-lines to make sarcomere length measurements from Z-line peak to Z-line peak. Z-line lengths were measured by visual inspection of the alpha-actinin channel and measured on FIJI with the line tool. Three or more consecutive Z-lines at least 0.70 μm long in a row were analyzed as sarcomeres. Cellpose segments with no nuclei or 3 or more nuclei, as well as cell segments on the edge of the image were excluded from analysis.

*Statistical analysis*

To compare two or more groups for the rescue experiments in NRVMs, pair-wise comparisons were performed. In order to reduce Type 1 error rate stemming from multiple comparisons, Bonferroni correction was applied to obtain a corrected alpha. Whether groups were normally distributed or not was determined by the Shapiro-Wilk test. To compare two normally distributed groups, Student's two-sample, unpaired t-test was used. If either group was not normally distributed, the non-parametric Mann-Whitney U test was used. The same analysis was applied to run lengths and capping duration from the TIRF seeded elongation assays.

For the TIRF seeded elongation rate and nucleation assay analysis, one-way ANOVA's were performed for 5 treatment comparisons with post-hoc Tukey tests as the variances between all treatments tested were fairly equal.

In all cases when the sample size exceeded 20, we removed outliers from the bottom and upper 2.5% of data to perform all statistical tests, regardless of normality, to avoid introducing bias. However, all plots shown include these outliers.

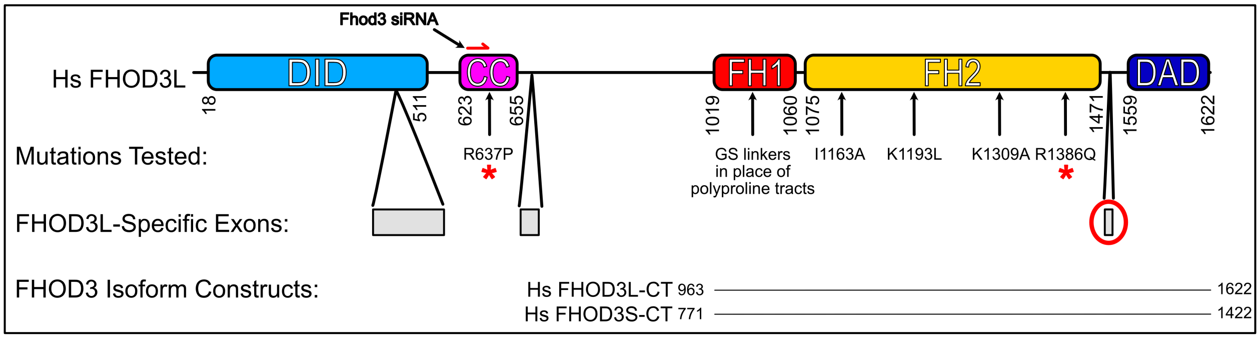

**Figure 2-1** – *Study overview of human FHOD3*

Domain structure of human FHOD3L. FH=Formin Homology, DID=Diaphanous Inhibitory Domain, DAD=Diaphanous Autoregulatory Domain, CC=Coiled-coil. Mutations tested throughout this study are indicated with black arrows. Red (*) indicates causative hypertrophic cardiomyopathy (HCM) mutations studied here. The FHOD3L construct (Uniprot Isoform 4) spans residues 963–1622 and includes the FH1 domain, FH2 domain, and tail. The FHOD3S construct (Uniprot Isoform 1) spans residues 771-1422. FHOD3L-specific exons are in gray. The 8-residue $T(D/E)_5XE$ exon that distinguishes FHOD3L-CT from FHOD3S-CT is circled in red.

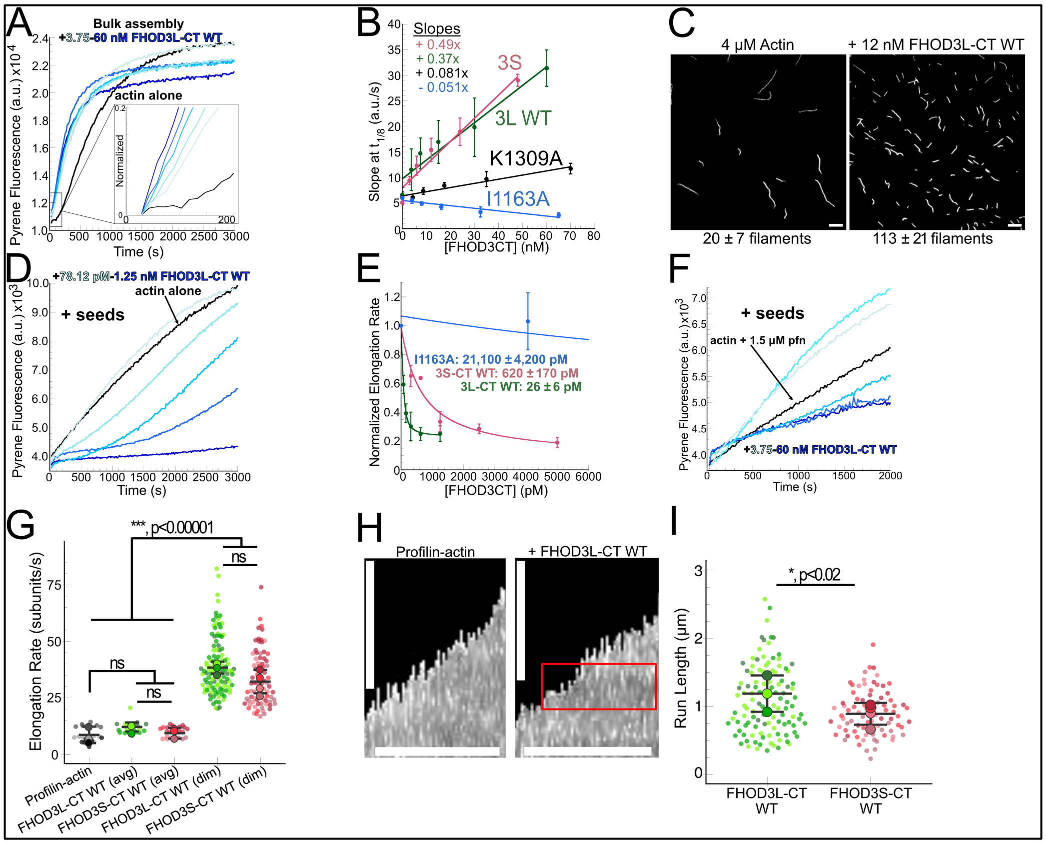

**Figure 2-2** – *Biochemical characterization of human FHOD3*

(**A**) Assembly of 4 µM rabbit muscle actin (5% pyrene-labeled) and the indicated concentrations of FHOD3L-CT WT from a 2-fold dilution series with the inset showing the first 200 seconds normalized to the plateau of 4 µM RSA. (**B**) Relative nucleation activity for FHOD3S/L-CT and FHOD3L-CT K1309A and I1163A (n=3 for all points; mean ± SD). (**C**) Actin polymerized in the presence or absence of 12 nM FHOD3L-CT WT diluted to 5 nM actin with fluorescent phalloidin. Scale bar, 10 µm. (n=3, each; mean ± SD.) (**D**) Barbed-end elongation assay. Final conditions were 0.25 µM F-actin seeds (~0.15 nM barbed ends), 0.5 µM G-actin (10% pyrene-labeled), and 78.12 pM-1.25 nM FHOD3L-CT WT. (**E**) Barbed-end affinity measurements for FHOD3L-CT WT (from **D**) and I1163A and FHOD3S-CT WT. (n=3, each; mean ± SD.) (**F**) Barbed-end elongation assays. Final conditions as in (**D**), but 1.5 µM *S. pombe* profilin with 3.75-60 nM FHOD3L-CT WT are added. (**G**) Elongation rates from TIRF assays. Conditions: 1 µM actin (10%-Alexa Fluor 488-labeled), 5 µM profilin-1 ± 100 pM FHOD3L-CT WT or 1 nM FHOD3S-CT WT. Average elongation rates (over 10s of seconds) and formin-mediated elongation rates (dim) are shown separately. (n=21, profilin-actin (avg), n=20, 3L (avg), n=24, 3S (avg), n=112, 3L (dim), n=78, 3S (dim); 4 flow channels for 3S, 3 flow channels for all others; mean ± SD, p-values by one-way ANOVA with post-hoc Tukey test.) (**H**) Kymographs of growing filaments from TIRF assays. Conditions as in (**G**). A capping event followed by a burst of elongation in the presence of FHOD3L-CT WT is boxed in red. Vertical scale bars, 5 µm, horizontal scale bars, 120 seconds. (**I**) Quantification of run lengths for FHOD3S/L-CT. Conditions as in (**G**). (n=112 3L; 3 flow channels; n=79 3S; 4 flow channels; mean ± SD, p-values by Mann-Whitney U test.)

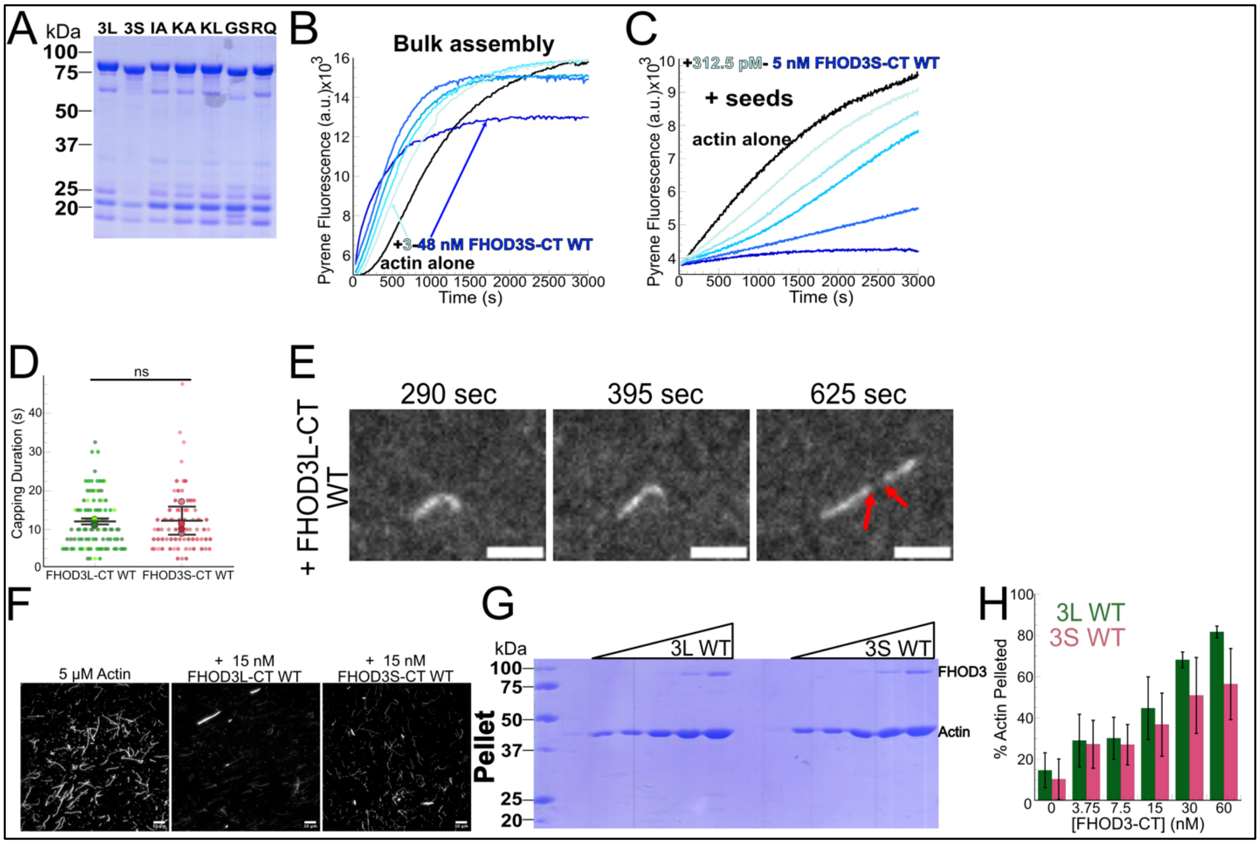

**Figure 2-3** – *Human FHOD3L is a more potent bundler, while FHOD3S is a more potent nucleator*

(**A**) Coomassie-stained polyacrylamide gel showing purified FHOD3 constructs. 3L=FHOD3L-CT WT, 3S=FHOD3S-CT WT, IA=I1163A, KA=K1309A, KL=K1193L, GS=GS-FH1, RQ=R1386Q. (**B**) Assembly of 4 μM actin (5% pyrene-labeled) and the indicated concentrations of FHOD3S-CT WT from a 2-fold dilution series. (**C**) Barbed-end elongation assay. Final conditions: 0.25 μM F-actin seeds (~0.15 nM barbed ends), 0.5 μM G-actin (10% pyrene-labeled), and 312.5 pM-5 nM FHOD3S-CT WT (**D**) Duration of capping events by FHOD3L-CT WT vs FHOD3S-CT WT observed by TIRF microscopy. Conditions as in Fig. 2G (n=97, 3L, n=73, 3S; 3 flow channels for 3L, 4 flow channels for 3S; mean ± SD, $p>0.05$ by Mann-Whitney U test.) (**E**) Time-lapse images from TIRF microscopy. Conditions as in Fig. 2-2G in the presence of FHOD3L-CT WT. Red arrows indicating dim portion of filament that was elongated by FHOD3L-CT WT. Scale bar, 10 μm. (**F**) Epifluorescence micrographs of phalloidin-stabilized filaments from a low-speed bundling assay with either 15 nM FHOD3L-CT WT or FHOD3S-CT WT with 5 μM actin compared to actin alone diluted to 5 nM actin before centrifugation. (**G**) Coomassie-stained polyacrylamide gel of pellet fractions from low-speed bundling assays with 5 μM actin and 0-60 nM FHOD3L-CT WT and FHOD3S-CT WT. (**H**) Quantification of bundling from (**G**) via densitometry (n=3 each group; mean ± SD.)

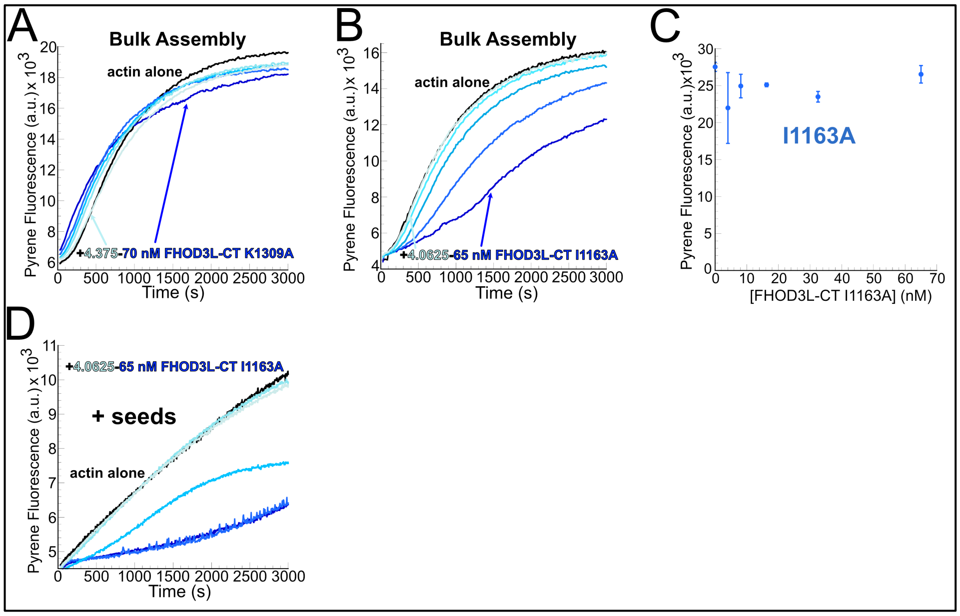

**Figure 2-4** – *FHOD3L K1309A and I1163A diminish nucleation activity and binding affinities*

(**A**) Assembly of 4 μM actin (5% pyrene-labeled) and the indicated concentrations of FHOD3L-CT K1309A from a 2-fold dilution series. (**B**) Conditions as in (**A**) with the indicated concentrations of FHOD3L-CT I1163A from a 2-fold dilution series. (**C**) Pyrene fluorescence readings after incubating different doses of FHOD3L-CT I1163A with 4 μM actin (5% pyrene-labeled) for 5 minutes. (n=2, I1163A; mean ± SD.) (**D**) Barbed-end elongation assay. Final conditions: 0.25 μM F-actin seeds (~0.15 nM barbed ends), 0.5 μM G-actin (10% pyrene-labeled), and 4.0625 nM-65 nM FHOD3L-CT I1163A.

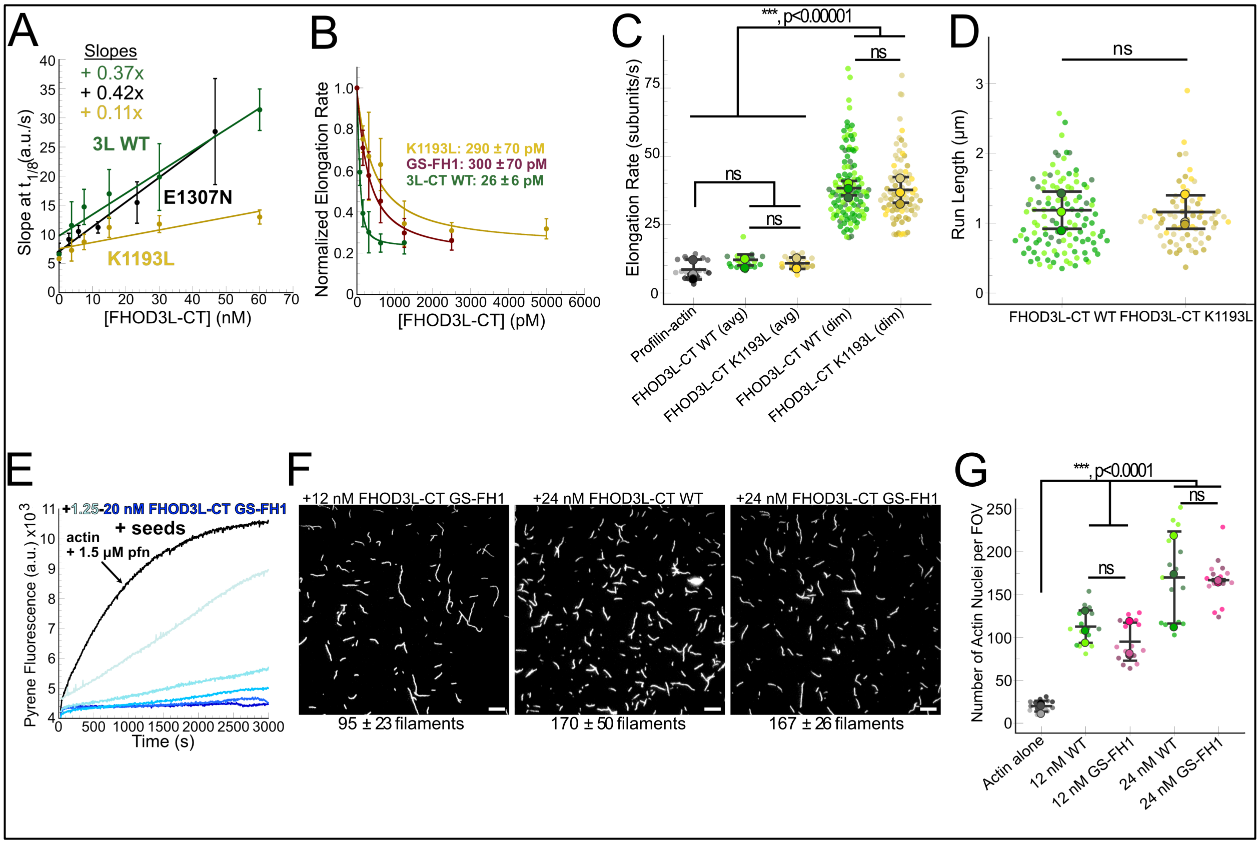

**Figure 2-5** – *FHOD3L-CT K1193L and GS-FH1 nearly isolate elongation or nucleation, respectively*

(**A**) Relative nucleation activity for FHOD3L-CT WT, K1193L, and E1307N. (n=3 for all points; mean ± SD.) (**B**) Barbed-end affinity measurements for FHOD3L-CT WT, GS-FH1, and K1193L. (n=3, each; mean ± SD.) (**C**) Elongation rates from TIRF assays. Conditions as in Fig. 2-2G with 100 pM FHOD3L-CT WT or 1 nM FHOD3L-CT K1193L. Average elongation rates (over 10s of seconds) and formin-mediated elongation rates (dim) are shown separately. (n=19, K1193L (avg), n=67, K1193L (dim); 3 flow channels; mean ± SD, p-values by one-way ANOVA with post-hoc Tukey test.) (**D**) Quantification of FHOD3L-CT WT and K1193L's run lengths. Conditions as in Fig. 2-2G. (n=67, K1193L; 3 flow channels; mean ± SD, p>0.05 by Mann-Whitney U test.) (**E**) Barbed-end elongation assay. Final conditions: 0.25 μM F-actin seeds (~0.15 nM barbed ends), 0.5 μM G-actin (10% pyrene-labeled), 1.5 μM *S. pombe* profilin, and 1.25 nM-20 nM FHOD3L-CT GS-FH1. (**F**) TIRF micrographs via TIRF nucleation assay using 4 μM actin diluted to 5 nM actin with 12 nM or 24 nM FHOD3L-CT WT or GS-FH1. Average filament numbers per field of view (FOV) below each image. (n=15 images, each; 3 biological replicates, each; mean ± SD.) (**G**) Quantification of number of filaments per FOV from (**F**). 5 images were taken per independent experiment. (n=15 images, each; 3 biological replicates, each; mean ± SD, p-values by one-way ANOVA with post-hoc Tukey test.)

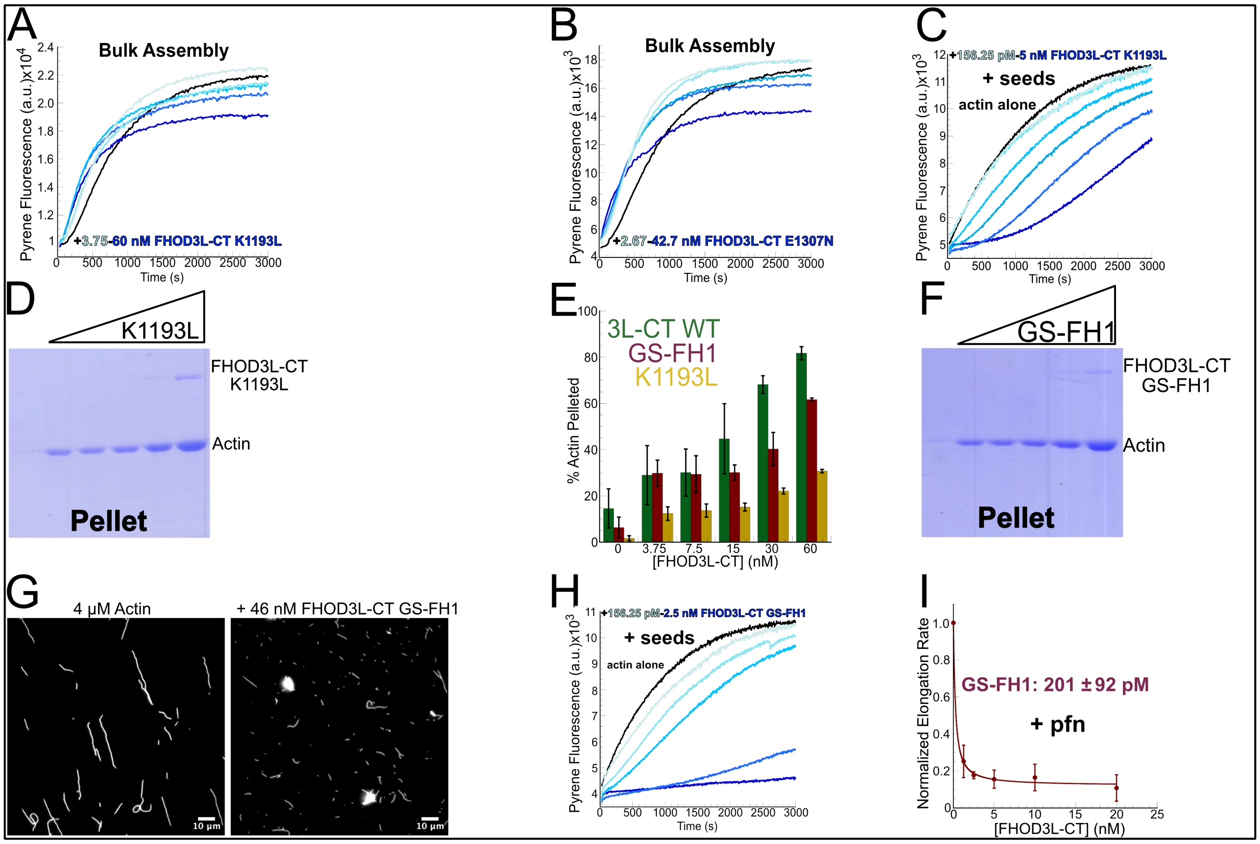

**Figure 2-6** – *Both FHOD3L-CT K1193L and GS-FH1 negatively impact bundling ability, but bind actin similarly*

(**A**) Conditions as in Fig. 2-2A with the indicated concentrations of FHOD3L-CT K1193L from a 2-fold dilution series. (**B**) Conditions as in Fig. 2-2A with the indicated concentrations of FHOD3L-CT E1307N from a 2-fold dilution series. (**C**) Barbed-end elongation assay. Final conditions were 0.25 µM F-actin seeds (~0.15 nM barbed ends), 0.5 µM G-actin (10% pyrene-labeled), and 156.25 pM-5 nM FHOD3L-CT K1193L. (**D**) Coomassie-stained polyacrylamide gel of pellet fractions from a low-speed bundling assay with 5 µM actin and 3.75 nM-60 nM FHOD3L-CT K1193L. (**E**) Quantification of bundling by FHOD3L-CT GS-FH1 and K1193L from (**D**) and (**F**) (n=3, each; mean ± SD.) (**F**) Coomassie-stained polyacrylamide gel of pellet fractions from a low-speed bundling assay with 3.75 nM-60 nM FHOD3L-CT GS-FH1. (**G**) TIRF micrographs from TIRF nucleation assays using 4 µM actin diluted to 5 nM actin in the presence or absence of 46 nM FHOD3L-CT GS-FH1. (**H**) Barbed-end elongation assay as in (**C**) with 156.25 pM-2.5 nM FHOD3L-CT GS-FH1. (**I**) Barbed-end affinity measurement for FHOD3L-CT GS-FH1 in the presence of profilin from Fig. 2-5E. (n=3; mean ± SD.)

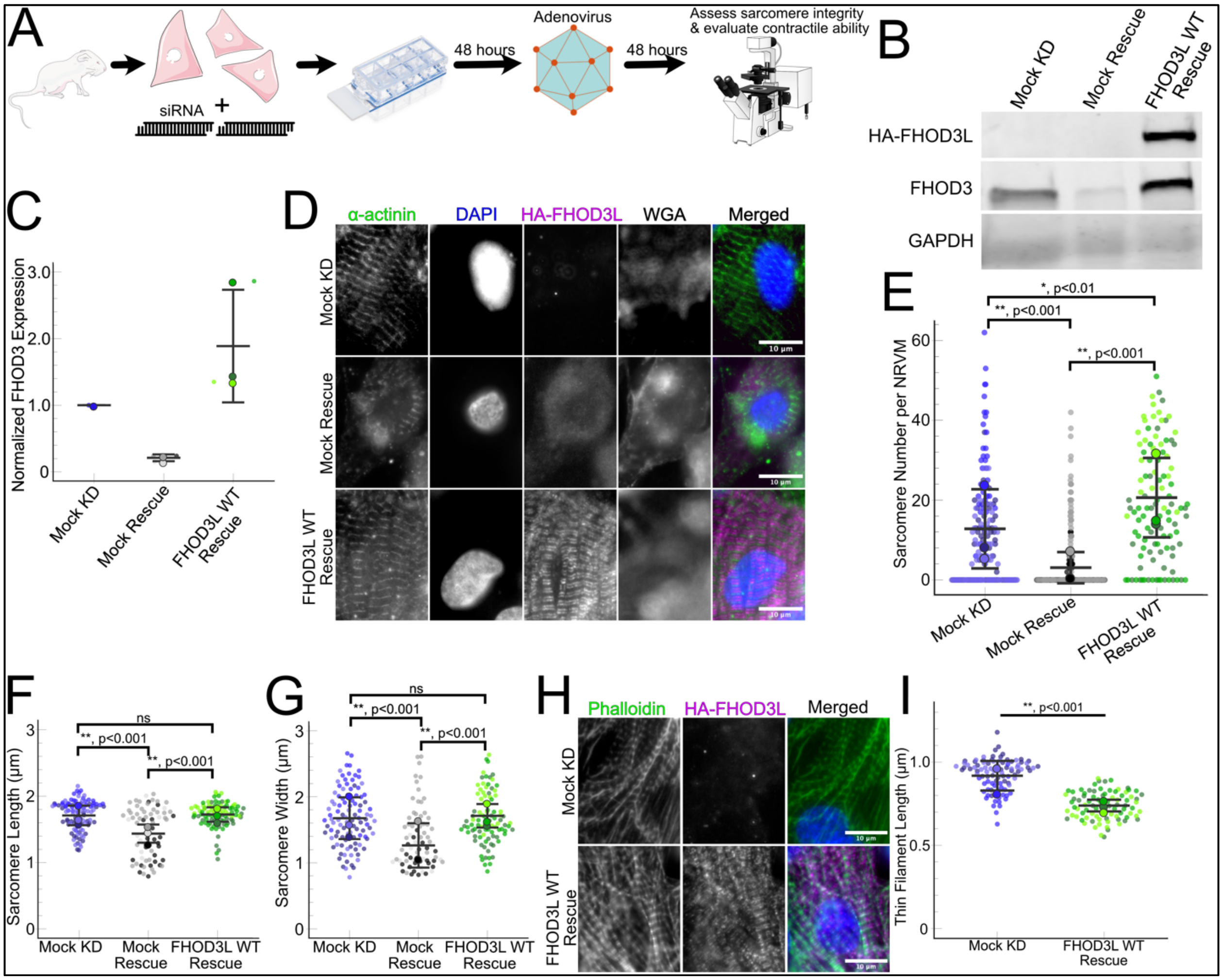

**Figure 2-7** – *Exogenous 3xHA-FHOD3L wild-type structurally rescues the sarcomeres in NRVMs after siRNA knockdown of endogenous FHOD3*

(**A**) Overview of the rescue experiments. Reverse transfection of siRNA upon plating NRVMs followed by infection with adenovirus to drive exogenous expression. (**B**) Western blot showing depletion of endogenous FHOD3 after knockdown, and exogenous FHOD3L expression levels after rescue. GAPDH used as a loading control. (**C**) Quantification of Western blot in (**B**) normalized to GAPDH for each lane and then normalized to endogenous levels in the mock knockdown. (n=3, each; mean ± SD.) (**D**) Epifluorescent micrographs showing sarcomere integrity from α-actinin (green) staining for the mock knockdown, mock rescue, and FHOD3L wild-type rescue. WGA not shown in the merged for clarity. DAPI (blue) and exogenous HA-FHOD3L wild-type (magenta). HA staining background is visible due to higher exposure needed to visualize FHOD3. (**E**) Quantification of sarcomere number per NRVM in the mock knockdown, mock rescue, and FHOD3L wild-type rescue. (n=160 cells, mock KD, n=334 cells, mock rescue, n=110 cells, WT rescue; 3 biological replicates, each; mean ± SD, p-values by Mann-Whitney U test.) (**F**) Average sarcomere lengths per NRVM for mock knockdown, mock rescue, and FHOD3L wild-type rescue. (n=100 cells, mock KD, n=71 cells, mock rescue, n=92 cells, WT rescue; 3 biological replicates, each; mean ± SD, p-values by Mann-Whitney U test.) (**G**) Average sarcomere widths (Z-line lengths) per NRVM for mock knockdown, mock rescue, and FHOD3L wild-type rescue. (n=100 cells, mock KD, n=71 cells, mock rescue, n=92 cells, WT rescue; 3 biological replicates, each; mean ± SD, p-values by Mann-Whitney U test.) (**H**) Epifluorescent micrographs showing mock knockdown and FHOD3L wild-type-rescued NRVMs stained for phalloidin (green) to stain thin filaments and exogenous HA-FHOD3L wild-type (magenta). (**I**) Quantification of thin filament lengths for mock knockdown and FHOD3L wild-type-rescued NRVMs. (n=94 cells, mock KD, n=84 cells, WT rescue; 3 biological replicates, each; mean ± SD, p-value by Mann-Whitney U test.)

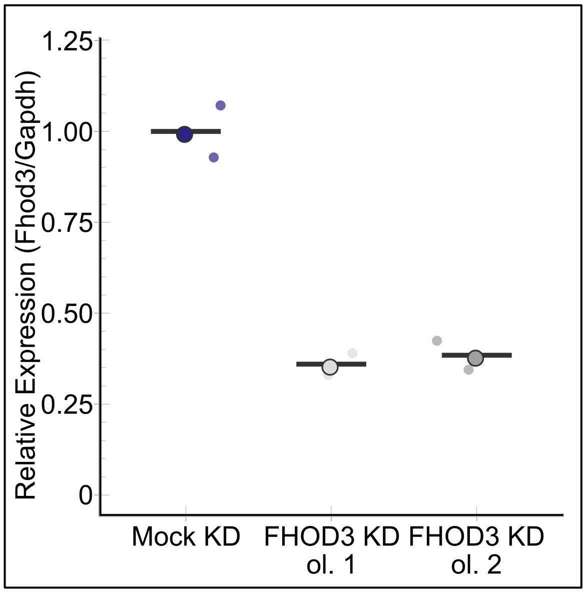

**Figure 2-8** – *Endogenous Fhod3 mRNA is sufficiently depleted at the end of the rescue timeline*

Relative mRNA expression of *Fhod3* in NRVMs after knockdown for two different siRNA oligos compared to *Gapdh* mRNA expression (n=2 wells, 1 biological replicate; mean).

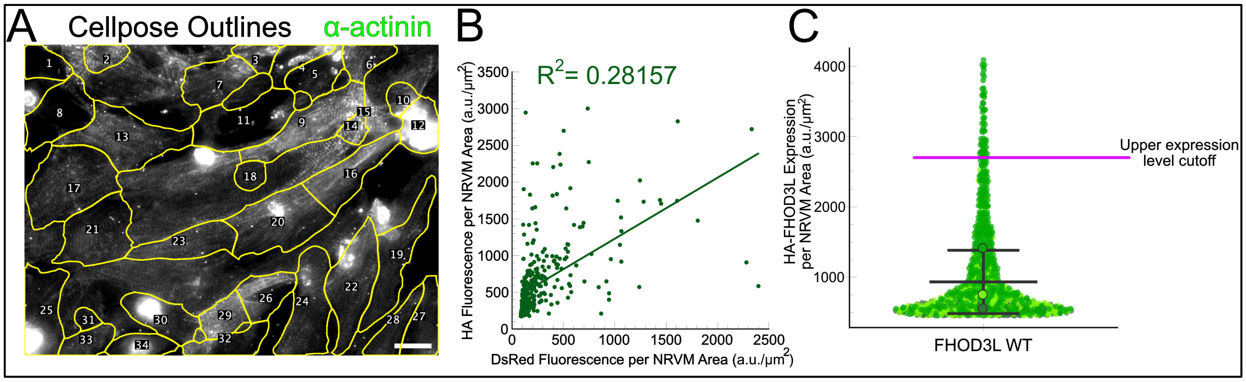

**Figure 2-9** – *Exogenous 3xHA-FHOD3L wild-type expression weakly correlates to DsRed fluorescence*

(**A**) Cellpose segmentation of wild-type FHOD3L-rescued NRVMs overlaid on the $\alpha$-actinin channel, typically used for manual quantification of sarcomeres. ROI's are numbered. Scale bar, 20 µm (**B**) Pairwise correlation of normalized DsRed fluorescence intensity per NRVM area vs. 3xHA-FHOD3L wild-type fluorescence intensity per NRVM area only showing a weak correlation (n=347 cells; 1 biological replicate). (**C**) Normalized and background corrected 3xHA-FHOD3L wild-type fluorescence intensity per NRVM area from the rescue. Purple line showing the upper expression level cutoff used for manual analysis of 2700 a.u./µm$^2$ (n=913 cells; 3 biological replicates; mean ± SD.)

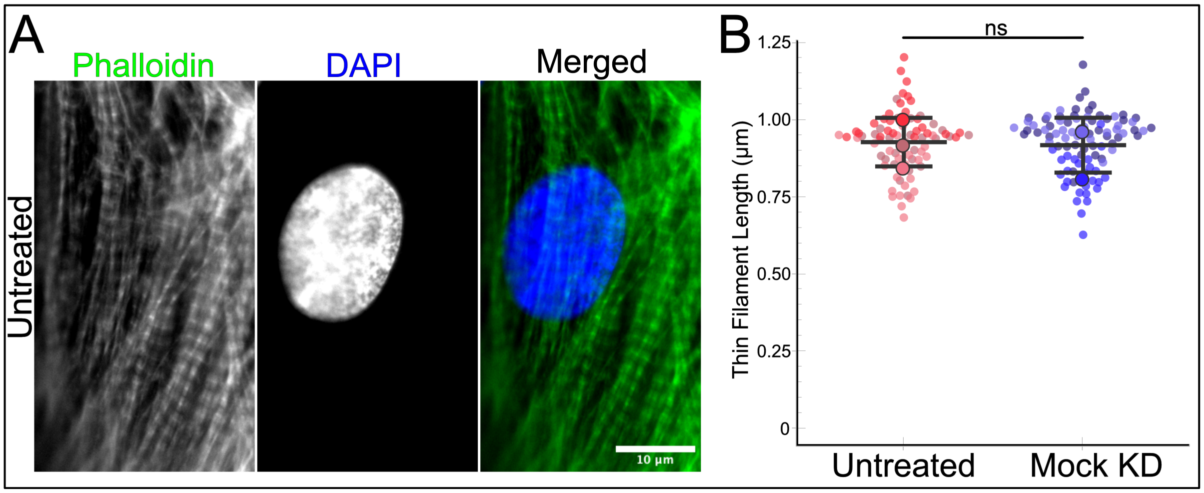

**Figure 2-10** – *Untreated and mock knockdown NRVMs have similar thin filament lengths*

(**A**) Epifluorescent micrographs of untreated NRVMs stained with phalloidin (green) and DAPI (blue). (**B**) Quantification of thin filament lengths of mock knockdown NRVMs and untreated NRVMs. (n=81 cells, untreated, n=94 cells, mock KD; 3 biological replicates, each; mean ± SD, p>0.05 by Mann-Whitney U test.)

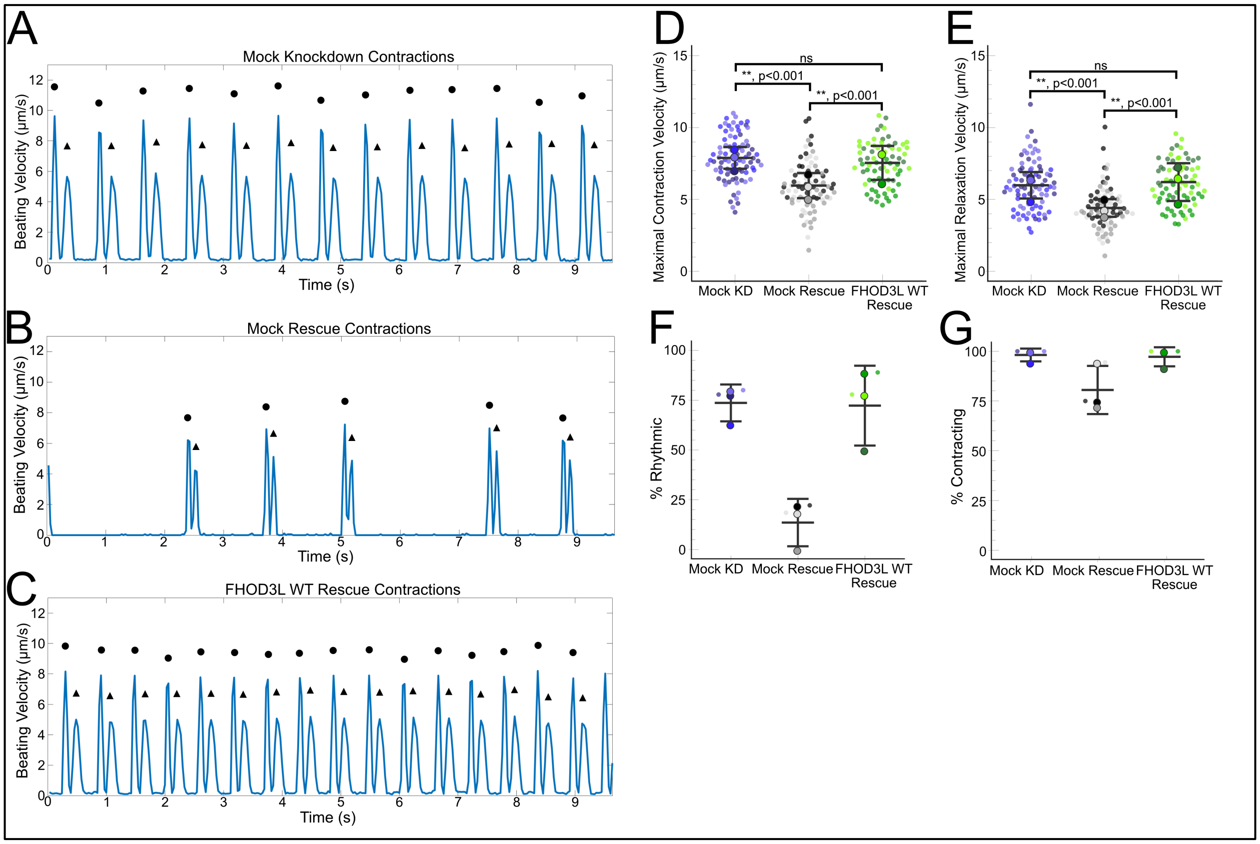

**Figure 2-11** – *Exogenous FHOD3L wild-type rescues contractile strength and rhythmicity*

(**A-C**) Motion speed analysis by digital image correlation. The first (•) and the second peak (▲) of the duplex represent the contraction and the relaxation speed, respectively. Mock knockdown, mock rescue, and FHOD3L wild-type rescue beating patterns are shown. (**D**) Maximal contraction velocities quantified for mock knockdown, mock rescue, and FHOD3L wild-type rescue (n=82 ROIs, mock KD, n=81 ROIs, mock rescue, n=72, ROIs, WT rescue; 3 biological replicates, each; mean ± SD, p-values by student's two-sample, unpaired t-test.) (**E**) Maximal relaxation velocities quantified for mock knockdown, mock rescue, and FHOD3L wild-type rescue (n=82 ROIs, mock KD, n=81 ROIs, mock rescue, n=72, ROIs, WT rescue; 3 biological replicates, each; mean ± SD, p-values by student's two-sample, unpaired t-test.) (**F**) Quantification of the percentage of analyzed ROI's from the videos that contained rhythmic contractions for mock knockdown, mock rescue, and FHOD3L wild-type rescue. (n=3, each; mean ± SD.) (**G**) Crude quantification of the percentage of NRVMs contracting in each video for mock knockdown, mock rescue, and FHOD3L wild-type rescue. (n=3, each; mean ± SD.)

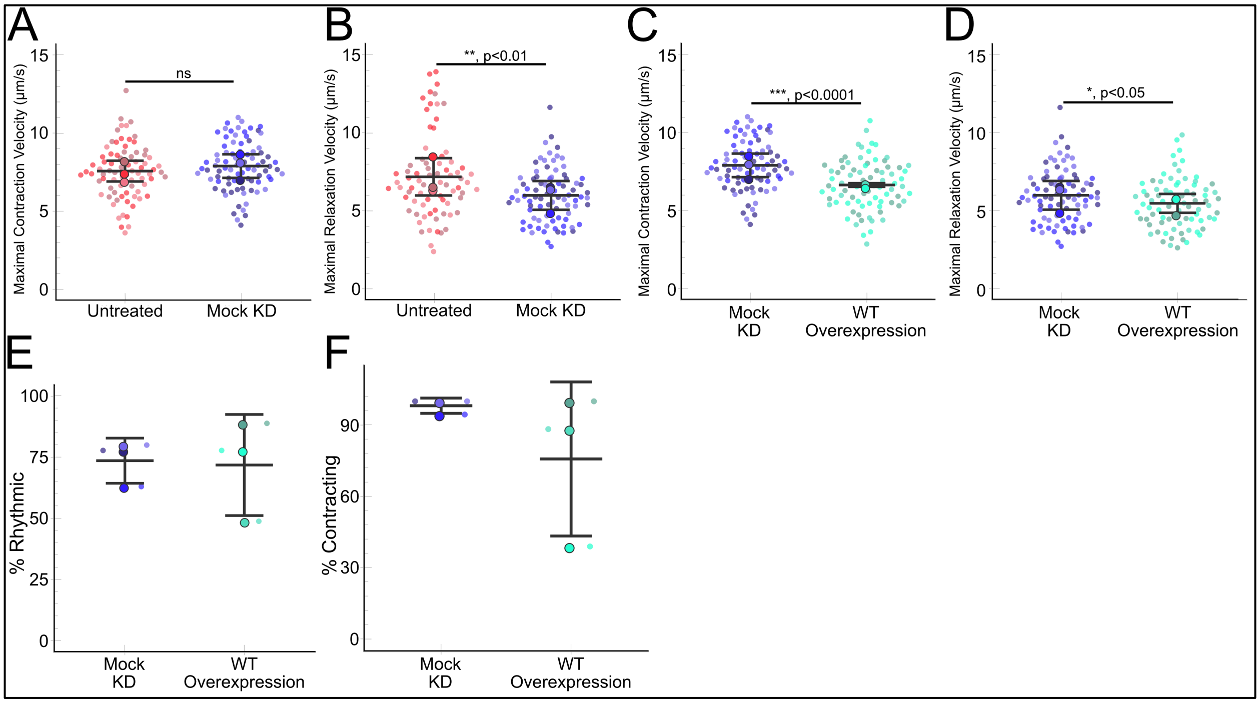

**Figure 2-12** – *Mock treatment does not negatively impact NRVMs contractile ability, but overexpression of exogenous FHOD3L wild-type above endogenous levels does*
(**A**) Maximal contraction velocities quantified for mock knockdown and untreated NRVMs (n=77 ROIs, untreated, n=82 ROIs, mock KD; 3 biological replicates, each; mean ± SD, p-value by student's two-sample, unpaired t-test.) (**B**) Maximal relaxation velocities quantified for mock knockdown and untreated NRVMs (n=77 ROIs, untreated, n=82 ROIs, mock KD; 3 biological replicates, each; mean ± SD, p-value by Mann-Whitney U test.) (**C**) Maximal contraction velocities quantified for FHOD3L wild-type rescue and FHOD3L wild-type overexpression NRVMs (n=82 ROIs, mock KD, n=79 ROIs, WT Overexpression; 3 biological replicates, each; mean ± SD, p-value by student's two-sample, unpaired t-test.) (**D**) Maximal relaxation velocities quantified for FHOD3L wild-type rescue and FHOD3L wild-type overexpression NRVMs (n=82 ROIs, mock KD, n=79 ROIs, WT Overexpression; 3 biological replicates, each; mean ± SD, p-value by student's two-sample, unpaired t-test.) (**E**) Quantification of rhythmic contractions as in Fig. 2-11F for mock knockdown and overexpression NRVMs (n=3, each; mean ± SD.) (**F**) Quantification of contracting NRVMs as in Fig. 2-11G for mock knockdown and overexpression NRVMs (n=3, each; mean ± SD.)

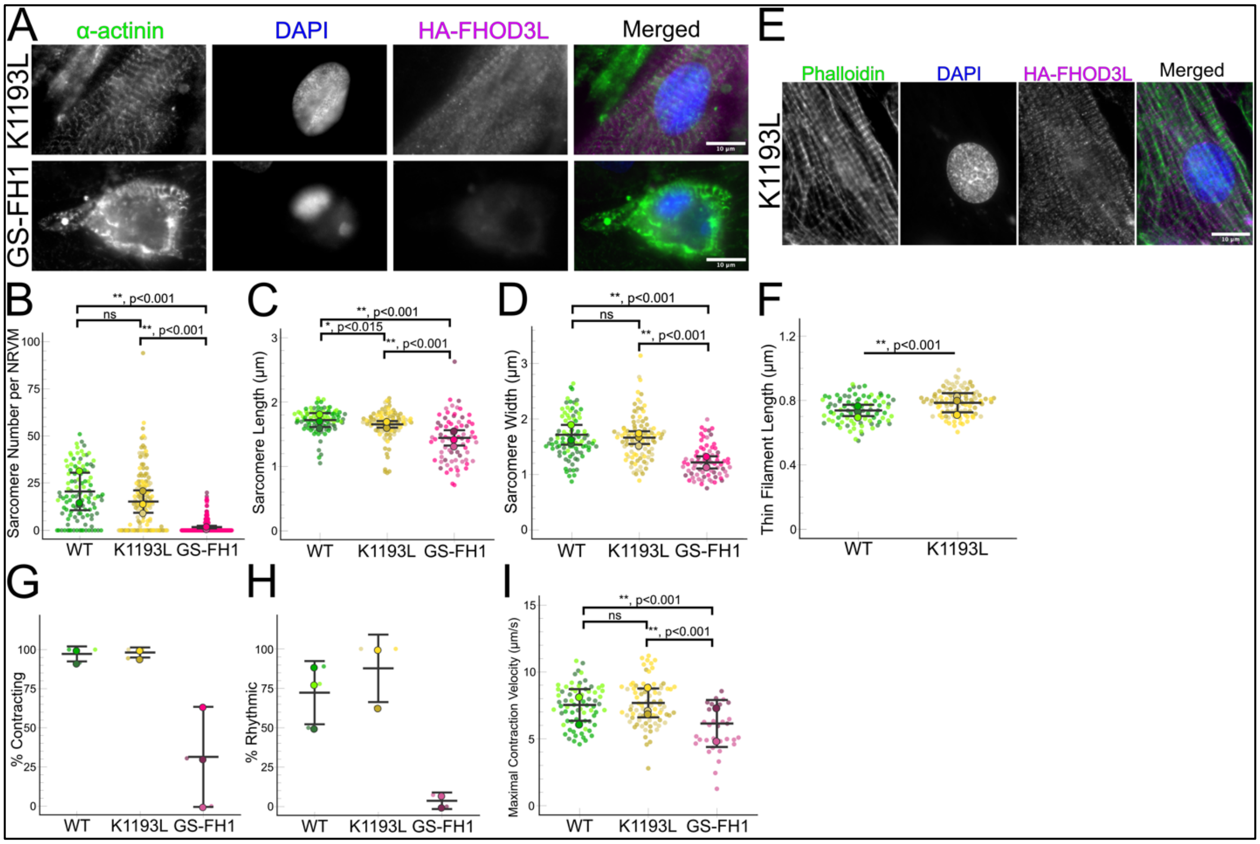

**Figure 2-13** – *FHOD3L elongation ability is required for proper sarcomere formation and cardiac function in NRVMs*

(**A**) Epifluorescent micrographs of FHOD3L GS-FH1 and K1193L-rescued NRVMs stained for α-actinin (green), DAPI (blue), and exogenous HA-FHOD3L (magenta). (**B**) Quantification of sarcomere number per NRVM in the FHOD3L wild-type, K1193L, and GS-FH1 rescues. (n=148 cells, K1193L, n=259 cells, GS-FH1; 3 biological replicates; mean ± SD, p-values by Mann-Whitney-U test.) (**C**) Average sarcomere lengths per NRVM for FHOD3L wild-type, K1193L, and GS-FH1-rescued NRVMs. (n=95 cells, K1193L, n=73 cells, GS-FH1; 3 biological replicates; mean ± SD, p-value for WT to GS-FH1 comparison by student's two-sample, unpaired t-test, all other p-values by Mann-Whitney-U test.) (**D**) Average sarcomere widths (Z-line lengths) per NRVM for FHOD3L wild-type, K1193L, and GS-FH1-rescued NRVMs. (n=95 cells, K1193L, n=73 cells, GS-FH1; 3 biological replicates; mean ± SD, p-values by Mann-Whitney-U test.) (**E**) Epifluorescent micrographs of a FHOD3L K1193L-rescued NRVM stained for phalloidin (green), DAPI (blue), and exogenous HA-FHOD3L (magenta). (**F**) Quantification of thin filament lengths for FHOD3L wild-type and K1193L-rescued NRVMs (n=99 cells, K1193L; 3 biological replicates, each; mean ± SD, p-value by Mann-Whitney-U test.) (**G**) Quantification of contracting NRVMs as in Fig. 2-11G for FHOD3L wild-type, K1193L, and GS-FH1-rescued NRVMs. (n=3, each; mean ± SD.) (**H**) Quantification of rhythmic contractions as in Fig. 2-11F for FHOD3L wild-type, K1193L, and GS-FH1-rescued NRVMs. (n=3, WT and K1193L, n=2, GS-FH1; mean ± SD.) (**I**) Maximal contraction velocities quantified for FHOD3L wild-type, K1193L, and GS-FH1-rescued NRVMs. (n=81 ROIs, K1193L, n=31, ROIs, GS-FH1; 3 biological replicates, WT and K1193L, 2 for GS-FH1; mean ± SD, p-value for K1193L to GS-FH1 comparison by student's two-sample, unpaired t-test, all other p-values by Mann-Whitney-U test.)

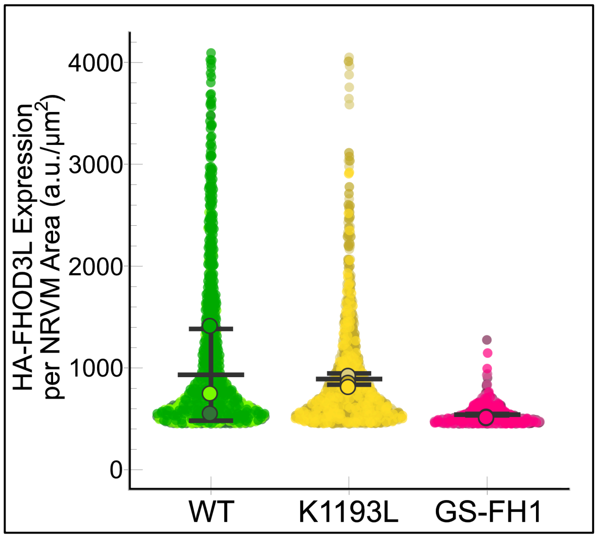

**Figure 2-14** – *FHOD3L GS-FH1-rescued NRVMs display reduced exogenous FHOD3L fluorescence intensity*

Normalized and background-corrected 3xHA-FHOD3L fluorescence intensity per NRVM area from the FHOD3L WT, K1193L, and GS-FH1 rescues. (n=897 cells, K1193L, n=536 cells, GS-FH1; 3 biological replicates, each; mean ± SD.)

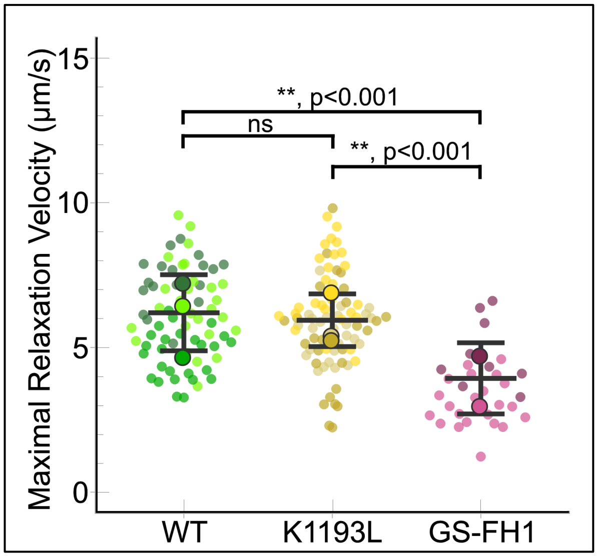

**Figure 2-15** – *FHOD3L elongation ability required for proper relaxation strengths in NRVMs*

(**A**) Maximal relaxation velocities for the FHOD3L WT, K1193L, and GS-FH1-rescued NRVMs. (n=81 ROIs, K1193L, n=31, ROIs, GS-FH1; 3 biological replicates, WT and K1193L, 2 for GS-FH1; mean ± SD, p-values by Mann-Whitney U test.)

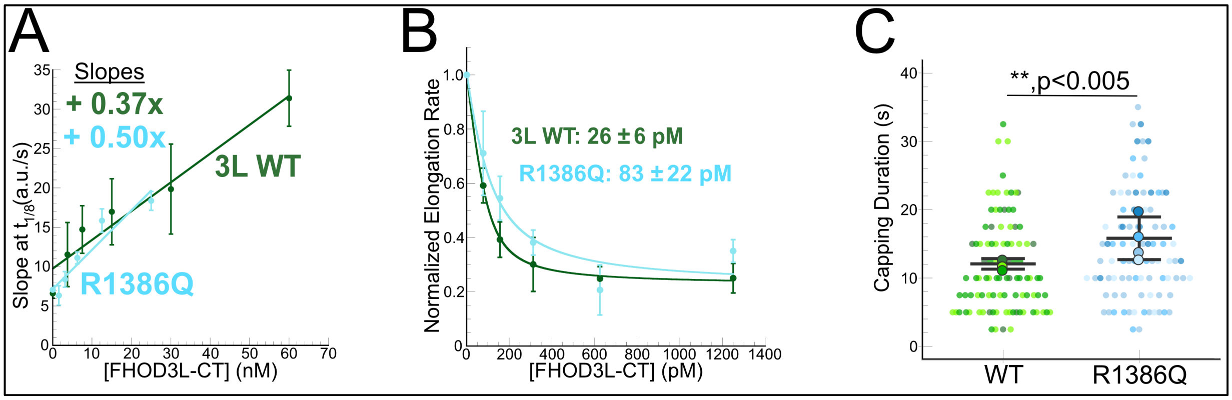

**Figure 2-16** – *FHOD3L hypertrophic cardiomyopathy mutant R1386Q improves nucleation ability, while maintaining elongation and barbed-end capping activity*
(**A**) Relative nucleation activity for FHOD3L-CT WT and R1386Q. (n=3 for all points; mean ± SD.) (**B**) Duration of capping events by FHOD3L-CT WT vs R1386Q observed via TIRF microscopy. Conditions as in Fig. 2-2G (n=91, R1386Q; 3 flow channels, WT, 4 flow channels, R1386Q; mean ± SD, p-values by Mann-Whitney U test.) (**C**) Barbed-end affinity measurements for FHOD3L-CT WT and R1386Q. (n=3, each; mean ± SD.)

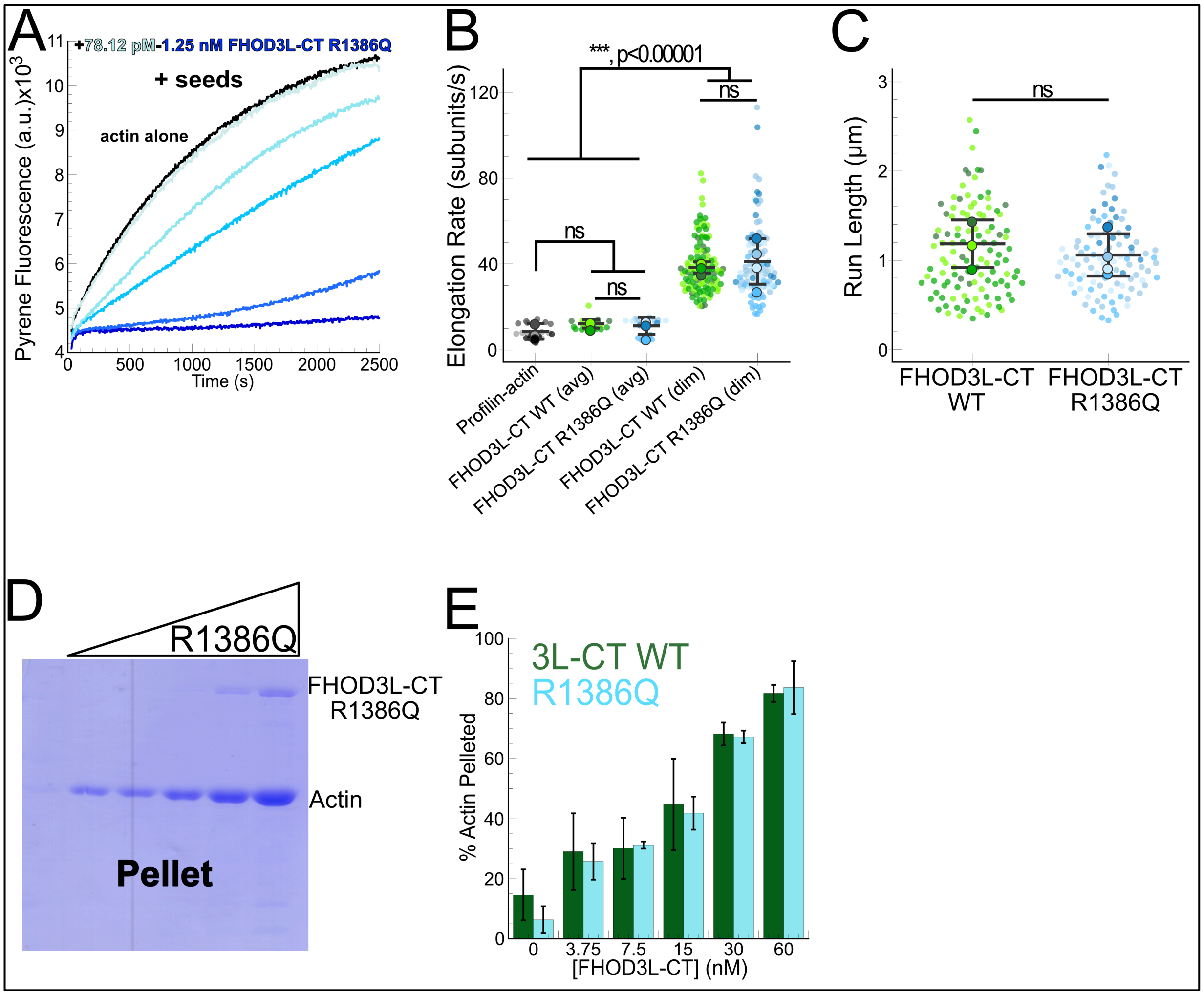

**Figure 2-17** – *FHOD3L-CT R1386Q and wild-type elongate and bundle actin similarly*
(**A**) Barbed-end elongation assay. Final conditions were 0.25 µM F-actin seeds (~0.15 nM barbed ends), 0.5 µM G-actin (10% pyrene-labeled), and 78.12 pM-1.25 nM FHOD3L-CT R1386Q. (**B**) Elongation rates from TIRF assays. Conditions as in Fig. 2-2G with 100 pM FHOD3L-CT WT or 200 pM FHOD3L-CT R1386Q. Average elongation rates (over 10s of seconds) and formin-mediated elongation rates (dim) are shown separately. (n=21, R1386Q (avg), n=98, R1386Q (dim); 3 flow channels, WT, 4 flow channels, R1386Q; mean ± SD, p-values by one-way ANOVA with post-hoc Tukey test.) (**C**) Quantification of FHOD3L-CT WT and R1386Q's run lengths. Conditions as in Fig. 2-2G. (n=98, R1386Q; 4 flow channels, R1386Q; mean ± SD, p>0.05 by Mann-Whitney U test.) (**D**) Coomassie-stained polyacrylamide gel of pellet fractions from a low-speed bundling assay with 5 µM actin and 3.75 nM-60 nM FHOD3L-CT R1386Q. (**E**) Quantification of bundling by FHOD3L-CT WT and R1386Q from (**D**) and Fig. 2-3G (n=3, each; mean ± SD.)

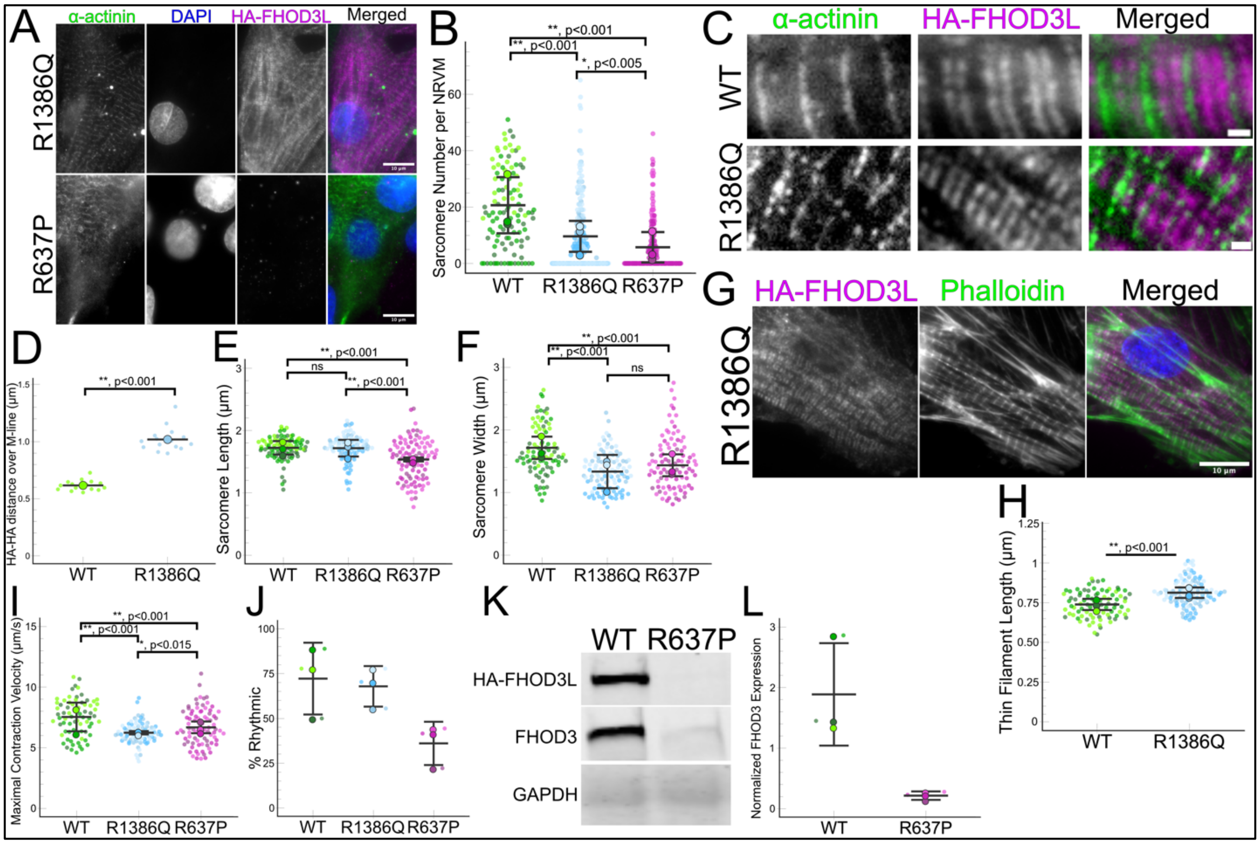

**Figure 2-18** – *FHOD3L hypertrophic cardiomyopathy mutants impact sarcomere formation and function*

(**A**) Epifluorescent micrographs of FHOD3L R1386Q or R637P-rescued NRVMs stained for α-actinin (green), DAPI (blue), and exogenous HA-FHOD3L (magenta). (**B**) Quantification of sarcomere number per NRVM in the FHOD3L wild-type, R1386Q, and R637P rescues. (n=198 cells, R1386Q, n=213 cells, R637P; 3 biological replicates, each; mean ± SD, p-values by Mann-Whitney-U test.) (**C**) Epifluorescent micrographs from a 3xHA-FHOD3L wild-type-rescued (top) and R1386Q-rescued (bottom) NRVMs. Scale bars, 1 μm. (**D**) Quantification of distances between HA-FHOD3L wild-type and R1386Q doublets across the M-line. (n=15 cells, each; 1 biological replicate, each; mean, p-value by Mann-Whitney U test.) (**E**) Average sarcomere lengths per NRVM for FHOD3L wild-type, R1386Q, and R637P-rescued NRVMs. (n=104 cells, R1386Q, n=97 cells, R637P; 3 biological replicates, each; mean ± SD, p-values by Mann-Whitney U test.) (**F**) Average sarcomere widths (Z-line lengths) per NRVM for FHOD3L wild-type, R1386Q, and R637P-rescued NRVMs. (n=104 cells, R1386Q, n=97 cells, R637P; 3 biological replicates, each; mean ± SD, p-values by Mann-Whitney U test.) (**G**) Epifluorescent micrographs of a FHOD3L R1386Q-rescued NRVM stained for phalloidin (green), exogenous HA-FHOD3L (magenta), and DAPI (blue). (**H**) Quantification of thin filament lengths for FHOD3L wild-type and R1386Q-rescued NRVMs (n=107 cells, R1386Q; 3 biological replicates, each; mean ± SD, p-value by Mann-Whitney U test.) (**I**) Maximal contraction velocities quantified for FHOD3L wild-type, R1386Q, and R637P-rescued NRVMs. (n=81 ROIs, R1386Q and R637P; 3 biological replicates, each; mean ± SD, p-values by Mann-Whitney U test.) (**J**) Quantification of rhythmic contractions as in Fig. 2-11F for FHOD3L wild-type, R1386Q, and R637P-rescued NRVMs. (n=3, each; mean ± SD.) (**K**) Western blot showing exogenous FHOD3L expression levels after wild-type or R637P rescue. GAPDH used as a loading control. (**L**) Quantification of Western blot in (**K**) showing low levels of FHOD3L R637P relative to endogenous FHOD3 after normalizing as in Fig. 2-7B-C (n=3, each; mean ± SD.)

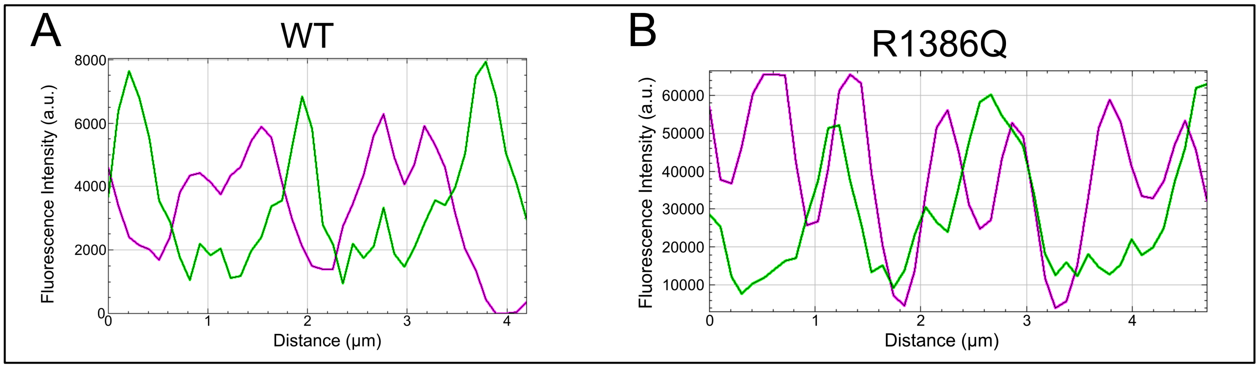

**Figure 2-19** – *Exogenous 3xHA-FHOD3L R1386Q localizes closer to sarcomere Z-lines compared to FHOD3L wild-type*

(**A**) Linescan from Fig. 2-18C showing the localization of exogenous 3xHA-FHOD3L wild-type (magenta) in between the Z-lines (green) of sarcomeres. (**B**) Linescan from Fig. 2-18C showing the localization of exogenous 3xHA-FHOD3L R1386Q (magenta) closer to the Z-lines (green).

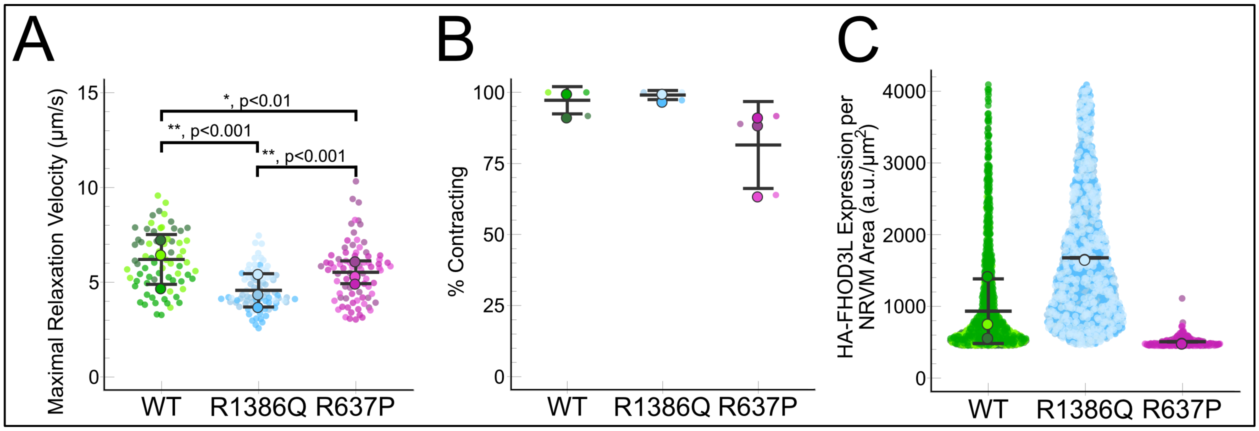

**Figure 2-20** – *FHOD3L R637P partially recovers contractile ability despite its possible degradation*

(**A**) Maximal relaxation velocities for FHOD3L wild-type, R1386Q, and R637P-rescued NRVMs. (n=81 ROIs, R1386Q and R637P; 3 biological replicates, each; mean ± SD, p-values by Mann-Whitney U test.) (**B**) Quantification of contracting NRVMs as in Fig. 2-11G for FHOD3L wild-type, R1386Q, and R637P-rescued NRVMs. (n=3, each; mean ± SD.) (**C**) Normalized and background corrected 3xHA-FHOD3L fluorescence intensity per NRVM area from the FHOD3L wild-type, R1386Q, and R637P rescues. (n=1213 cells, R1386Q, n=340 cells, R637P; 3 biological replicates; mean ± SD.)

|  | Nucleation Strength (by $t_{1/8}$ slopes) (a.u./s) | Barbed end binding affinity (no profilin) (pM) | Elongation Rate (subunits/ s) | Run Length (μm) | Capping duration (s) | Bundling (% actin pelleted at 60 nM) |
|---|---|---|---|---|---|---|
| FHOD3L-CT Wild-type | 0.37 ± 0.08 | 25.5 ± 5.7 | 39 ± 13 | 1.10 ± 0.49 | 11.8 ± 6.8 | 81.7 ± 2.9 |
| FHOD3S-CT Wild-type | 0.49 ± 0.06 | 620 ± 170 | 33 ± 12 | 0.90 ± 0.33 | 12.0 ± 7.8 | 56 ± 17 |
| FHOD3L-CT I1163A | -0.051 ± 0.004 | 21,100 ± 4,200 | n.d. | n.d. | n.d. | n.d. |
| FHOD3L-CT K1309A | 0.081 ± 0.020 | n.d. | n.d. | n.d. | n.d. | n.d. |
| FHOD3L-CT K1193L | 0.11 ± 0.02 | 290 ± 70 | 38 ± 12 | 1.11 ± 0.42 | 12.7 ± 5.6 | 30.8 ± 0.7 |
| FHOD3L-CT GS-FH1 | Nucleates similarly via TIRF nucleation assay | 300 ± 70 | n.d. | n.d. | n.d. | 61.7 ± 0.7 |
| FHOD3L-CT R1386Q | 0.50 ± 0.09 | 83 ± 22 | 41 ± 1 | 1.04 ± 0.40 | 15.2 ± 9.6 | 83.6 ± 8.8 |

**Table 2-1** – *Biochemical summary of FHOD3L-CT wild-type and mutants*
All data shown are means ± standard deviation each from 3 independent experiments. n.d.= no data.

|  | FHOD3 KD? | FHOD3 AdV? | Maximal Contraction Velocity (μm/s) | Maximal Relaxation Velocity (μm/s) | Avg % Rhythmic Contractions | Avg % Contracting NRCs in FOV | Sarcomere Length (μm) | Z-Line Length (μm) | Avg Sarcomere Number per NRVM | Thin Filament Length (nm) |
|---|---|---|---|---|---|---|---|---|---|---|
| Untreated | N/A | N/A | 7.6 ± 1.7 | 7.2 ± 2.6 | 58 ± 36 | 92.5 ± 0.4 | n.d. | n.d. | n.d. | 928 ± 97 |
| Mock Knockdown | - | - | 7.9 ± 1.6 | 6.0 ± 1.7 | 74 ± 9 | 98.2 ± 3.2 | 1.71 ± 0.22 | 1.69 ± 0.43 | 12 ± 13 | 925 ± 94 |
| Mock Rescue | + | - | 6.0 ± 1.7 | 4.4 ± 1.5 | 14 ± 12 | 89 ± 11 | 1.46 ± 0.37 | 1.38 ± 0.46 | 3 ± 7 | n.d. |
| WT Rescue | + | + | 7.5 ± 1.5 | 6.1 ± 1.5 | 72 ± 20 | 97.2 ± 4.8 | 1.72 ± 0.18 | 1.70 ± 0.46 | 19 ± 14 | 739 ± 81 |
| K1193L Rescue | + | + | 7.7 ± 1.6 | 5.9 ± 1.6 | 88 ± 21 | 98.2 ± 3.2 | 1.65 ± 0.22 | 1.67 ± 0.41 | 15 ± 16 | 792 ± 79 |
| GS-FH1 Rescue | + | + | 5.6 ± 1.7 | 3.6 ± 1.2 | 3.7 ± 5.2 | 32 ± 32 | 1.42 ± 0.35 | 1.23 ± 0.29 | 2 ± 4 | n.d. |
| R1386Q Rescue | + | + | 6.2 ± 0.9 | 4.6 ± 1.1 | 68 ± 11 | 99.1 ± 1.6 | 1.72 ± 0.20 | 1.34 ± 0.30 | 9 ± 13 | 813 ± 83 |
| R637P Rescue | + | + | 6.7 ± 1.5 | 5.5 ± 1.6 | 36 ± 12 | 82 ± 15 | 1.54 ± 0.32 | 1.46 ± 0.43 | 6 ± 9 | n.d. |
| FHOD3L WT Over-expression | - | + | 6.6 ± 1.6 | 5.5 ± 1.6 | 72 ± 21 | 76 ± 32 | n.d. | n.d. | n.d. | n.d. |

**Table 2-2** – *Summary of FHOD3L wild-type and mutant rescues in NRVMs*

All data shown are means ± standard deviation each from 3 independent experiments (except for GS-FH1 rescue average % rhythmic contractions and maximal contraction and relaxation velocity measurements from 2 independent experiments due to one biological replicate not contracting.) n.d.= no data. “-“ = negative control siRNA or empty virus, “+” = FHOD3 siRNA or corresponding FHOD3L adenovirus.

## References

Ajima, R., Bisson, J. A., Helt, J.-C., Nakaya, M.-A., Habas, R., Tessarollo, L., He, X., Morrisey, E. E., Yamaguchi, T. P., & Cohen, E. D. (2015). DAAM1 and DAAM2 are co-required for myocardial maturation and sarcomere assembly. *Developmental Biology*, *408*(1), 126–139. https://doi.org/10.1016/j.ydbio.2015.10.003

Antoku, S., Wu, W., Joseph, L. C., Morrow, J. P., Worman, H. J., & Gundersen, G. G. (2019). ERK1/2 Phosphorylation of FHOD Connects Signaling and Nuclear Positioning Alternations in Cardiac Laminopathy. *Developmental Cell*, *51*(5), 602-616.e12. https://doi.org/10.1016/j.devcel.2019.10.023

Arimura, T., Takeya, R., Ishikawa, T., Yamano, T., Matsuo, A., Tatsumi, T., Nomura, T., Sumimoto, H., & Kimura, A. (2013). Dilated Cardiomyopathy-Associated FHOD3 Variant Impairs the Ability to Induce Activation of Transcription Factor Serum Response Factor. *Circ J*, *77*(12), 2990-2996. https://doi.org/10.1253/circj.cj-13-0255

Baer, A., & Kehn-Hall, K. (2014). Viral Concentration Determination Through Plaque Assays: Using Traditional and Novel Overlay Systems. *Journal of Visualized Experiments : JoVE*, *93*, 52065. https://doi.org/10.3791/52065

Baker, J. L., Courtemanche, N., Parton, D. L., McCullagh, M., Pollard, T. D., & Voth, G. A. (2015). Electrostatic Interactions between the Bni1p Formin FH2 Domain and Actin Influence Actin Filament Nucleation. *Structure*, *23*(1), 68–79. https://doi.org/10.1016/j.str.2014.10.014

Bogdanov, V., Soltisz, A. M., Moise, N., Sakuta, G., Orengo, B. H., Janssen, P. M. L., Weinberg, S. H., Davis, J. P., Veeraraghavan, R., & Györke, S. (2021). Distributed synthesis of sarcolemmal and sarcoplasmic reticulum membrane proteins in cardiac myocytes. *Basic Research in Cardiology*, *116*(1), 63. https://doi.org/10.1007/s00395-021-00895-3

Bor, B., Vizcarra, C. L., Phillips, M. L., & Quinlan, M. E. (2012). Autoinhibition of the formin Cappuccino in the absence of canonical autoinhibitory domains. *Molecular Biology of the Cell*, *23*(19), 3801–3813. https://doi.org/10.1091/mbc.E12-04-0288

Boussaty, E. C., Ninoyu, Y., Andrade, L., Li, Q., Takeya, R., Sumimoto, H., Ohyama, T., Wahlin, K. J., Manor, U., & Friedman, R. A. (2023). Altered Fhod3 Expression Involved in Progressive High-Frequency Hearing Loss via Dysregulation of Actin Polymerization Stoichiometry in The Cuticular Plate. *bioRxiv: The Preprint Server for Biology*, 2023.07.20.549974. https://doi.org/10.1101/2023.07.20.549974

Bremer, K. V., Wu, C., Patel, A. A., He, K. L., Grunfeld, A. M., Chanfreau, G. F., & Quinlan, M. E. (2024). Formin tails act as a switch, inhibiting or enhancing processive actin elongation. *The Journal of Biological Chemistry*, *300*(1), 105557. https://doi.org/10.1016/j.jbc.2023.105557

Cao, L., Kerleau, M., Suzuki, E. L., Wioland, H., Jouet, S., Guichard, B., Lenz, M., Romet-Lemonne, G., & Jegou, A. (2018). Modulation of formin processivity by profilin and mechanical tension. *eLife*, *7*, e34176. https://doi.org/10.7554/eLife.34176

Colpan, M., Iwanski, J., & Gregorio, C. C. (2021). CAP2 is a regulator of actin pointed end dynamics and myofibrillogenesis in cardiac muscle. *Communications Biology*, *4*(1), 1–15. https://doi.org/10.1038/s42003-021-01893-w

Courtemanche, N. (2018). Mechanisms of formin-mediated actin assembly and dynamics. *Biophysical Reviews*, *10*(6), 1553–1569. https://doi.org/10.1007/s12551-018-0468-6

Courtemanche, N., & Pollard, T. D. (2012). Determinants of Formin Homology 1 (FH1) Domain Function in Actin Filament Elongation by Formins. *The Journal of Biological Chemistry*, *287*(10), 7812–7820. https://doi.org/10.1074/jbc.M111.322958

Cutler, K. J., Stringer, C., Lo, T. W., Rappez, L., Stroustrup, N., Peterson, S. P., Wiggins, P. A., & Mougous, J. D. (2022). Omnipose: A high-precision morphology-independent solution for bacterial cell segmentation. *Nature Methods*. *19*, 1438-1448. https://doi.org/10.1101/2021.11.03.467199

Denes, L. T., Kelley, C. P., & Wang, E. T. (2021). Microtubule-based transport is essential to distribute RNA and nascent protein in skeletal muscle. *Nature Communications*, *12*(1), 6079. https://doi.org/10.1038/s41467-021-26383-9

Dlugosz, A. A., Antin, P. B., Nachmias, V. T., & Holtzer, H. The relationship between stress fiber-like structures and nascent myofibrils in cultured cardiac myocytes. (1984). *The Journal of Cell Biology*, *99*(6), 2268–2278. https://doi.org/10.1083/jcb.99.6.2268

Ehler, E. (2018). Actin-associated proteins and cardiomyopathy—The ‘unknown’ beyond troponin and tropomyosin. *Biophysical Reviews*, *10*(4), 1121–1128. https://doi.org/10.1007/s12551-018-0428-1

Eisner, V., Csordás, G., & Hajnóczky, G. (2013). Interactions between sarco-endoplasmic reticulum and mitochondria in cardiac and skeletal muscle – pivotal roles in $Ca^{2+}$ and reactive oxygen species signaling. *Journal of Cell Science*, *126*(14), 2965–2978. https://doi.org/10.1242/jcs.093609

Farkas, D., Szikora, S., Jijumon, A. S., Polgár, T. F., Patai, R., Tóth, M. Á., Bugyi, B., Gajdos, T., Bíró, P., Novák, T., Erdélyi, M., & Mihály, J. (2024). Peripheral thickening of the sarcomeres and pointed end elongation of the thin filaments are both promoted by SALS and its formin interaction partners. *PLOS Genetics*, *20*(1), e1011117. https://doi.org/10.1371/journal.pgen.1011117

Fenix, A. M., Neininger, A. C., Taneja, N., Hyde, K., Visetsouk, M. R., Garde, R. J., & Burnette, D. T. (2018). Muscle-specific stress fibers give rise to sarcomeres in cardiomyocytes. *eLife*, *7*, e42144. https://doi.org/10.7554/eLife.42144

Fernandez-Sanz, C., Ruiz-Meana, M., Miro-Casas, E., Nuñez, E., Castellano, J., Loureiro, M., Barba, I., Poncelas, M., Rodriguez-Sinovas, A., Vázquez, J., & Garcia-Dorado, D. (2014). Defective sarcoplasmic reticulum–mitochondria calcium exchange in aged mouse myocardium. *Cell Death & Disease*, *5*(12), e1573–e1573. https://doi.org/10.1038/cddis.2014.526

Ferreira-Martins, J., & Leite-Moreira, A. F. (2010). Physiologic Basis and Pathophysiologic Implications of the Diastolic Properties of the Cardiac Muscle. *Journal of Biomedicine and Biotechnology*, *2010*, 807084. https://doi.org/10.1155/2010/807084

Fujimoto, N., Kan-o, M., Ushijima, T., Kage, Y., Tominaga, R., Sumimoto, H., & Takeya, R. (2016). Transgenic Expression of the Formin Protein Fhod3 Selectively in the Embryonic Heart: Role of Actin-Binding Activity of Fhod3 and Its Sarcomeric Localization during Myofibrillogenesis. *PLoS ONE*, *11*(2), e0148472. https://doi.org/10.1371/journal.pone.0148472

Funk, J., Merino, F., Schaks, M., Rottner, K., Raunser, S., & Bieling, P. (2021). A barbed end interference mechanism reveals how capping protein promotes nucleation in branched actin networks. *Nature Communications*, *12*(1), 5329. https://doi.org/10.1038/s41467-021-25682-5

Gardberg, M., Kaipio, K., Lehtinen, L., Mikkonen, P., Heuser, V. D., Talvinen, K., Iljin, K., Kampf, C., Uhlen, M., Grénman, R., Koivisto, M., & Carpén, O. (2013). FHOD1, a Formin Upregulated in Epithelial-Mesenchymal Transition, Participates in Cancer Cell Migration and Invasion. *PLOS ONE*, *8*(9), e74923. https://doi.org/10.1371/journal.pone.0074923

Garfinkel, A. C., Seidman, J. G., & Seidman, C. E. (2018). Genetic Pathogenesis of Hypertrophic and Dilated Cardiomyopathy. *Heart Failure Clinics*, *14*(2), 139–146. https://doi.org/10.1016/j.hfc.2017.12.004

Gasteier, J. E., Madrid, R., Krautkrämer, E., Schröder, S., Muranyi, W., Benichou, S., & Fackler, O. T. (2003). Activation of the Rac-binding Partner FHOD1 Induces Actin Stress Fibers via a ROCK-dependent Mechanism. *Journal of Biological Chemistry*, *278*(40), 38902–38912. https://doi.org/10.1074/jbc.M306229200

Gould, C. J., Maiti, S., Michelot, A., Graziano, B. R., Blanchoin, L., & Goode, B. L. (2011). The Formin DAD Domain Plays Dual Roles in Autoinhibition and Actin Nucleation. *Current Biology*, *21*(5), 384–390. https://doi.org/10.1016/j.cub.2011.01.047

Harris, E. S., Li, F., & Higgs, H. N. (2004). The Mouse Formin, FRLα, Slows Actin Filament Barbed End Elongation, Competes with Capping Protein, Accelerates Polymerization from Monomers, and Severs Filaments. *Journal of Biological Chemistry*, *279*(19), 20076-20087. https://doi.org/10.1074/jbc.M312718200

Hennis, K., Piantoni, C., Biel, M., Fenske, S., & Wahl-Schott, C. (2024). Pacemaker Channels and the Chronotropic Response in Health and Disease. *Circulation Research*, *134*(10), 1348–1378. https://doi.org/10.1161/CIRCRESAHA.123.323250

Huebsch, N., Loskill, P., Mandegar, M. A., Marks, N. C., Sheehan, A. S., Ma, Z., Mathur, A., Nguyen, T. N., Yoo, J. C., Judge, L. M., Spencer, C. I., Chukka, A. C., Russell, C. R., So, P.-L., Conklin, B. R., & Healy, K. E. (2015). Automated Video-Based Analysis of Contractility and Calcium Flux in Human-Induced Pluripotent Stem Cell-Derived Cardiomyocytes Cultured over Different Spatial Scales. *Tissue Engineering Part C: Methods*, *21*(5), 467–479. https://doi.org/10.1089/ten.tec.2014.0283

Iskratsch, T., Lange, S., Dwyer, J., Kho, A. L., Remedios, C. dos, & Ehler, E. (2010). Formin follows function: A muscle-specific isoform of FHOD3 is regulated by CK2 phosphorylation and promotes myofibril maintenance. *Journal of Cell Biology*, *191*(6), 1159–1172. https://doi.org/10.1083/jcb.201005060

Iskratsch, T., Reijntjes, S., Dwyer, J., Toselli, P., Dégano, I. R., Dominguez, I., & Ehler, E. (2013). Two distinct phosphorylation events govern the function of muscle FHOD3. *Cellular and Molecular Life Sciences : CMLS*, *70*(5), 893–908. https://doi.org/10.1007/s00018-012-1154-7

Iskratsch, T., Yu, C.-H., Mathur, A., Hone, J., Ehler, E., & Sheetz, M. (2013). FHOD1 Is Needed for Directed Forces and Adhesion Maturation during Cell Spreading and Migration. *Developmental Cell*, *27*(5), 545-559. https://doi.org/10.1016/j.devcel.2013.11.003

Jansen, S., Collins, A., Yang, C., Rebowski, G., Svitkina, T., & Dominguez, R. (2011). Mechanism of Actin Filament Bundling by Fascin. *The Journal of Biological Chemistry*, *286*(34), 30087–30096. https://doi.org/10.1074/jbc.M111.251439

Jurmeister, S., Baumann, M., Balwierz, A., Keklikoglou, I., Ward, A., Uhlmann, S., Zhang, J. D., Wiemann, S., & Sahin, O. (2012). MicroRNA-200c Represses Migration and Invasion of Breast Cancer Cells by Targeting Actin-Regulatory

Proteins FHOD1 and PPM1F. *Molecular and Cellular Biology*, *32*(3), 633-651. https://doi.org/ 10.1128/MCB.06212-11

Kan-o, M., Takeya, R., Abe, T., Kitajima, N., Nishida, M., Tominaga, R., Kurose, H., & Sumimoto, H. (2012). Mammalian formin Fhod3 plays an essential role in cardiogenesis by organizing myofibrillogenesis. *Biology Open | The Company of Biologists*, *1*(9), 889-896. https://doi.org/10.1242/bio.20121370

Kan-o, M., Takeya, R., Taniguchi, K., Tanoue, Y., Tominaga, R., & Sumimoto, H. (2012). Expression and Subcellular Localization of Mammalian Formin Fhod3 in the Embryonic and Adult Heart. *PLOS ONE*, *7*(4), e34765. https://doi.org/10.1371/journal.pone.0034765

Koka, S., Neudauer, C. L., Li, X., Lewis, R. E., McCarthy, J. B., & Westendorf, J. J. (2003). The formin-homology-domain-containing protein FHOD1 enhances cell migration. *Journal of Cell Science | The Company of Biologists*, *116*(9), 1745-1755. https://doi.org/10.1242/jcs.00386

Lewis, Y. E., Moskovitz, A., Mutlak, M., Heineke, J., Caspi, L. H., & Kehat, I. (2018). Localization of transcripts, translation, and degradation for spatiotemporal sarcomere maintenance. *Journal of Molecular and Cellular Cardiology*, *116*, 16–28. https://doi.org/10.1016/j.yjmcc.2018.01.012

Li, D., Hallett, M. A., Zhu, W., Rubart, M., Liu, Y., Yang, Z., Chen, H., Haneline, L. S., Chan, R. J., Schwartz, R. J., Field, L. J., Atkinson, S. J., & Shou, W. (2011). Dishevelled-associated activator of morphogenesis 1 (Daam1) is required for heart morphogenesis. *Development*, *138*(2), 303–315. https://doi.org/10.1242/dev.055566

Littlefield, R., & Fowler, V. M. (2002). Measurement of Thin Filament Lengths by Distributed Deconvolution Analysis of Fluorescence Images. *Biophysical Journal*, *82*(5), 2548–2564. https://doi.org/10.1016/S0006-3495(02)75598-7

Liu, H., & Naismith, J. H. (2008). An efficient one-step site-directed deletion, insertion, single and multiple-site plasmid mutagenesis protocol. *BMC Biotechnology*, *8*, 91. https://doi.org/10.1186/1472-6750-8-91

Maizel, J. V., White, D. O., & Scharff, M. D. (1968). The polypeptides of adenovirus: I. Evidence for multiple protein components in the virion and a comparison of types 2, 7A, and 12. *Virology*, *36*(1), 115–125. https://doi.org/10.1016/0042-6822(68)90121-9

Matsuyama, S., Kage, Y., Fujimoto, N., Ushijima, T., Tsuruda, T., Kitamura, K., Shiose, A., Asada, Y., Sumimoto, H., & Takeya, R. (2018). Interaction between cardiac myosin-binding protein C and formin Fhod3. *Proceedings of the National*

*Academy of Sciences*, *115*(19), E4386–E4395. https://doi.org/10.1073/pnas.1716498115

Moseley, J. B., & Goode, B. L. (2005). Differential Activities and Regulation of Saccharomyces cerevisiae Formin Proteins Bni1 and Bnr1 by Bud6. *Journal of Biological Chemistry*, *280*(30), 28023–28033. https://doi.org/10.1074/jbc.M503094200

Myasnikov, R., Bukaeva, A., Kulikova, O., Meshkov, A., Kiseleva, A., Ershova, A., Petukhova, A., Divashuk, M., Zotova, E., Sotnikova, E., Kharlap, M., Zharikova, A., Vyatkin, Y., Ramensky, V., Abisheva, A., Muraveva, A., Koretskiy, S., Kudryavtseva, M., Popov, S., … Drapkina, O. (2022). A Case of Severe Left-Ventricular Noncompaction Associated with Splicing Altering Variant in the FHOD3 Gene. *Genes*, *13*(2), Article 2. https://doi.org/10.3390/genes13020309

Nakano, H., Minami, I., Braas, D., Pappoe, H., Wu, X., Sagadevan, A., Vergnes, L., Fu, K., Morselli, M., Dunham, C., Ding, X., Stieg, A. Z., Gimzewski, J. K., Pellegrini, M., Clark, P. M., Reue, K., Lusis, A. J., Ribalet, B., Kurdistani, S. K., … Nakano, A. (2017). Glucose inhibits cardiac muscle maturation through nucleotide biosynthesis. *eLife*, *6*, e29330. https://doi.org/10.7554/eLife.29330

Neeman-Egozi, S., Livneh, I., Dolgopyat, I., Nussinovitch, U., Milman, H., Cohen, N., Eisen, B., Ciechanover, A., & Binah, O. (2024). Stress-Induced Proteasome Sub-Cellular Translocation in Cardiomyocytes Causes Altered Intracellular Calcium Handling and Arrhythmias. *International Journal of Molecular Sciences*, *25*(9), 4932. https://doi.org/10.3390/ijms25094932

Neininger-Castro, A. C., Jr, J. B. H., Sanchez, Z. C., Taneja, N., Fenix, A. M., Moparthi, S., Vassilopoulos, S., & Burnette, D. T. (2023). Independent regulation of Z-lines and M-lines during sarcomere assembly in cardiac myocytes revealed by the automatic image analysis software sarcApp. *eLife*, *12*. https://doi.org/10.7554/eLife.87065.2

Ochoa, J. P., Sabater-Molina, M., Garcia-Pinilla, J. M., Mogensen, J., Restrepo-Cordoba, A., Palomino-Doza, J., Villacorta, E., Martinez-Moreno, M., Ramos-Maqueda, J., Zorio, E., Peña-Peña, M. L., García-Granja, P. E., Rodríguez-Palomares, J. F., Cárdenas-Reyes, I. J., de la Torre-Carpente, M. M., Bautista-Pavés, A., Akhtar, M. M., Cicerchia, M. N., Bilbao-Quesada, R., … Monserrat, L. (2018). Formin Homology 2 Domain Containing 3 (FHOD3) Is a Genetic Basis for Hypertrophic Cardiomyopathy. *Journal of the American College of Cardiology*, 72(20), 2457-2467. https://doi.org/10.1016/j.jacc.2018.10.001

Okreglak, V., & Drubin, D. G. (2007). Cofilin recruitment and function during actin-mediated endocytosis dictated by actin nucleotide state. *Journal of Cell Biology*, *178*(7), 1251–1264. https://doi.org/10.1083/jcb.200703092

Ono, S. (2010). Dynamic regulation of sarcomeric actin filaments in striated muscle. *Cytoskeleton*, *67*(11), 677–692. https://doi.org/10.1002/cm.20476

Oosterheert, W., Boiero Sanders, M., Funk, J., Prumbaum, D., Raunser, S., & Bieling, P. (2024). Molecular mechanism of actin filament elongation by formins. *Science*, *384*(6692), eadn9560. https://doi.org/10.1126/science.adn9560

O'Shea, K. M., Ananthakrishnan, R., Li, Q., Quadri, N., Thiagarajan, D., Sreejit, G., Wang, L., Zirpoli, H., Aranda, J. F., Alberts, A. S., Schmidt, A. M., & Ramasamy, R. (2017). The Formin, DIAPH1, is a Key Modulator of Myocardial Ischemia/Reperfusion Injury. *EBioMedicine*, *26*, 165–174. https://doi.org/10.1016/j.ebiom.2017.11.012

Papa, I., Astier, C., Kwiatek, O., Raynaud, F., Bonnal, C., Lebart, M. C., Roustan, C., & Benyamin, Y. (1999). Alpha actinin-CapZ, an anchoring complex for thin filaments in Z-line. *Journal of Muscle Research and Cell Motility*, *20*(2), 187–197. https://doi.org/10.1023/a:1005489319058

Pappas, C. T., Bhattacharya, N., Cooper, J. A., & Gregorio, C. C. (2008). Nebulin Interacts with CapZ and Regulates Thin Filament Architecture within the Z-Disc. *Molecular Biology of the Cell*, *19*(5), 1837–1847. https://doi.org/10.1091/mbc.E07-07-0690

Patel, A. A., Oztug Durer, Z. A., van Loon, A. P., Bremer, K. V., & Quinlan, M. E. (2018). Drosophila and human FHOD family formin proteins nucleate actin filaments. *Journal of Biological Chemistry*, *293*(2), 532–540. https://doi.org/10.1074/jbc.M117.800888

Pernier, J., Shekhar, S., Jegou, A., Guichard, B., & Carlier, M.-F. (2016). Profilin Interaction with Actin Filament Barbed End Controls Dynamic Instability, Capping, Branching, and Motility. *Developmental Cell*, *36*(2), 201–214. https://doi.org/10.1016/j.devcel.2015.12.024

Rhee, D., Sanger, J. M., & Sanger, J. W. (1994). The premyofibril: Evidence for its role in myofibrillogenesis. *Cell Motility*, *28*(1), 1–24. https://doi.org/10.1002/cm.970280102

Robinson, T. F., & Winegrad, S. (1979). The measurement and dynamic implications of thin filament lengths in heart muscle. *The Journal of Physiology*, *286*, 607–619. https://doi.org/10.1113/jphysiol.1979.sp012640

Rosado, M., Barber, C. F., Berciu, C., Feldman, S., Birren, S. J., Nicastro, D., & Goode, B. L. (2014). Critical roles for multiple formins during cardiac myofibril development and repair. *Molecular Biology of the Cell*, *25*(6), 811–827. https://doi.org/10.1091/mbc.e13-08-0443

Sanematsu, F., Kanai, A., Ushijima, T., Shiraishi, A., Takaya, A., Kage, Y., Sumimoto, H., & Takeya, R. (2019). Fhod1, an actin-organizing formin family protein, is dispensable for cardiac development and function in mice. *Cytoskeleton*, 76(2), 219-229. https://doi.org/10.1002/cm.21523

Sanger, J. W., Kang, S., Siebrands, C. C., Freeman, N., Du, A., Wang, J., Stout, A. L., & Sanger, J. M. (2005). How to build a myofibril. *Journal of Muscle Research & Cell Motility*, *26*(6), 343–354. https://doi.org/10.1007/s10974-005-9016-7

Scarborough, E. A., Uchida, K., Vogel, M., Erlitzki, N., Iyer, M., Phyo, S. A., Bogush, A., Kehat, I., & Prosser, B. L. (2021). Microtubules orchestrate local translation to enable cardiac growth. *Nature Communications*, *12*, 1547. https://doi.org/10.1038/s41467-021-21685-4

Schonichen, A., Mannherz, H. G., Behrmann, E., Mazur, A. J., Kuhn, S., Silvan, U., Schoenenberger, C.-A., Fackler, O. T., Raunser, S., Dehmelt, L., & Geyer, M. (2013). FHOD1 is a combined actin filament capping and bundling factor that selectively associates with actin arcs and stress fibers. *Journal of Cell Science*, *126*(8), 1891–1901. https://doi.org/10.1242/jcs.126706

Schulze, N., Graessi, M., Soares, A., Geyer, M., Dehmelt, L., & Nalbant, P. (2014). FHOD1 regulates stress fiber organization by controlling the dynamics of transverse arcs and dorsal fibers. *Journal of Cell Science | The Company of Biologists*, *127*(7), 1379-1393. https://doi.org/10.1242/jcs.134627

Skwarek-Maruszewska, A., Hotulainen, P., Mattila, P. K., & Lappalainen, P. (2009). Contractility-dependent actin dynamics in cardiomyocyte sarcomeres. *Journal of Cell Science*, *122*(12), 2119–2126. https://doi.org/10.1242/jcs.046805

Solís, C., Warren, C. M., Dittloff, K., DiNello, E., Solaro, R. J., & Russell, B. (2023). Cardiomyocyte external mechanical unloading activates modifications of α-actinin differently from sarcomere-originated unloading. *The FEBS Journal*, *290*(22), 5322–5339. https://doi.org/10.1111/febs.16925

Spudich, J. A., & Watt, S. (1971). The Regulation of Rabbit Skeletal Muscle Contraction. *Journal of Biological Chemistry*, *246*(15), 4866–4871. https://doi.org/10.1016/S0021-9258(18)62016-2

Stringer, C., Wang, T., Michaelos, M., & Pachitariu, M. (2021). Cellpose: A generalist algorithm for cellular segmentation. *Nature Methods*, *18*(1), Article 1. https://doi.org/10.1038/s41592-020-01018-x

Sun, H., Luo, Y., & Miao, Y. (2018). Purification of Globular Actin from Rabbit Muscle and Pyrene Fluorescent Assays to Investigate Actin Dynamics in vitro. *Bio-Protocol*, *8*(23), e3102. https://doi.org/10.21769/BioProtoc.3102

Szikora, S., Görög, P., & Mihály, J. (2022). The Mechanisms of Thin Filament Assembly and Length Regulation in Muscles. *International Journal of Molecular Sciences*, *23*(10), Article 10. https://doi.org/10.3390/ijms23105306

Tadros, R., Francis, C., Xu, X., Vermeer, A. M. C., Harper, A. R., Huurman, R., Kelu Bisabu, K., Walsh, R., Hoorntje, E. T., te Rijdt, W. P., Buchan, R. J., van Velzen, H. G., van Slegtenhorst, M. A., Vermeulen, J. M., Offerhaus, J. A., Bai, W., de Marvao, A., Lahrouchi, N., Beekman, L., … Bezzina, C. R. (2021). Shared genetic pathways contribute to risk of hypertrophic and dilated cardiomyopathies with opposite directions of effect. *Nature Genetics*, *53*(2), 128–134. https://doi.org/10.1038/s41588-020-00762-2

Takeya, R., & Sumimoto, H. (2003). Fhos, a mammalian formin, directly binds to F-actin via a region N-terminal to the FH1 domain and forms a homotypic complex via the FH2 domain to promote actin fiber formation. *Journal of Cell Science*, *116*(22), 4567–4575. https://doi.org/10.1242/jcs.00769

Takeya, R., Taniguchi, K., Narumiya, S., & Sumimoto, H. (2008). The mammalian formin FHOD1 is activated through phosphorylation by ROCK and mediates thrombin-induced stress fiber formation in endothelial cells. *The EMBO Journal*, *27*(4), 618–628. https://doi.org/10.1038/emboj.2008.7

Taniguchi, K., Takeya, R., Suetsugu, S., Kan-o, M., Narusawa, M., Shiose, A., Tominaga, R., & Sumimoto, H. (2009). Mammalian formin Fhod3 regulates actin assembly and sarcomere organization in striated muscles. *Journal of Biological Chemistry*, *284*(43), 29873–29881. https://doi.org/10.1074/jbc.M109.059303

Tolkatchev, D., Jr, G. E. S., Schultz, L. E., Colpan, M., Helms, G. L., Cort, J. R., Gregorio, C. C., & Kostyukova, A. S. (2020). Leiomodin creates a leaky cap at the pointed end of actin-thin filaments. *PLOS Biology*, *18*(9), e3000848. https://doi.org/10.1371/journal.pbio.3000848

Ushijima, T., Fujimoto, N., Matsuyama, S., Kan-o, M., Kiyonari, H., Shioi, G., Kage, Y., Yamasaki, S., Takeya, R., & Sumimoto, H. (2018). The actin-organizing formin protein Fhod3 is required for postnatal development and functional maintenance of the adult heart in mice. *The Journal of Biological Chemistry*, *293*(1), 148–162. https://doi.org/10.1074/jbc.M117.813931

van Rijsingen, I. A. W., Hermans-van Ast, J. F., Arens, Y. H. J. M., Schalla, S. M., de Die-Smulders, C. E. M., van den Wijngaard, A., & Pinto, Y. M. (2009). Hypertrophic cardiomyopathy family with double-heterozygous mutations; does disease severity suggest double heterozygosity? *Netherlands Heart Journal*, *17*(12), 458–463. https://doi.org/10.1007/BF03086304

Vizcarra, C. L., Bor, B., & Quinlan, M. E. (2014). The Role of Formin Tails in Actin Nucleation, Processive Elongation, and Filament Bundling. *The Journal of*

*Biological Chemistry*, *289*(44), 30602–30613. https://doi.org/10.1074/jbc.M114.588368

Vodnjov, N., Toplišek, J., Maver, A., Čuturilo, G., Jaklič, H., Teran, N., Višnjar, T., Pušenjak, M. Š., Hodžić, A., Miljanović, O., Peterlin, B., & Writzl, K. (2023). A novel splice-site FHOD3 founder variant is a common cause of hypertrophic cardiomyopathy in the population of the Balkans–A cohort study. *PLOS ONE*, *18*(12), e0294969. https://doi.org/10.1371/journal.pone.0294969

Wear, M. A., Yamashita, A., Kim, K., Maéda, Y., & Cooper, J. A. (2003). How Capping Protein Binds the Barbed End of the Actin Filament. *Current Biology*, *13*(17), 1531–1537. https://doi.org/10.1016/S0960-9822(03)00559-1

Wessels, M. W., Herkert, J. C., Frohn-Mulder, I. M., Dalinghaus, M., van den Wijngaard, A., de Krijger, R. R., Michels, M., de Coo, I. F., Hoedemaekers, Y. M., & Dooijes, D. (2015). Compound heterozygous or homozygous truncating MYBPC3 mutations cause lethal cardiomyopathy with features of noncompaction and septal defects. *European Journal of Human Genetics*, *23*(7), 922–928. https://doi.org/10.1038/ejhg.2014.211

Wooten, E. C., Hebl, V. B., Wolf, M. J., Greytak, S. R., Orr, N. M., Draper, I., Calvino, J. E., Kapur, N. K., Maron, M. S., Kullo, I. J., Ommen, S. R., Bos, J. M., Ackerman, M. J., & Huggins, G. S. (2013). Formin homology 2 domain containing 3 variants associated with hypertrophic cardiomyopathy. *Circulation: Cardiovascular Genetics*, *6*(1), 10–18. https://doi.org/10.1161/CIRCGENETICS.112.965277

Wu, G., Ruan, J., Liu, J., Zhang, C., Kang, L., Wang, J., Zou, Y., & Song, L. (2021). Variant Spectrum of Formin Homology 2 Domain-Containing 3 Gene in Chinese Patients With Hypertrophic Cardiomyopathy. *Journal of the American Heart Association*, *10*(5), e018236. https://doi.org/10.1161/JAHA.120.018236

Wu, T., Mu, Y., Bogomolovas, J., Fang, X., Veevers, J., Nowak, R. B., Pappas, C. T., Gregorio, C. C., Evans, S. M., Fowler, V. M., & Chen, J. (2017). HSPB7 is indispensable for heart development by modulating actin filament assembly. *Proceedings of the National Academy of Sciences*, *114*(45), 11956–11961. https://doi.org/10.1073/pnas.1713763114

Xu, Y., Moseley, J. B., Sagot, I., Poy, F., Pellman, D., Goode, B. L., & Eck, M. J. (2004). Crystal Structures of a Formin Homology-2 Domain Reveal a Tethered Dimer Architecture. *Cell*, *116*(5), 711–723. https://doi.org/10.1016/S0092-8674(04)00210-7

Yamashiro, S., Yamakita, Y., Ono, S., & Matsumura, F. (1998). Fascin, an Actin-bundling Protein, Induces Membrane Protrusions and Increases Cell Motility of Epithelial Cells. *Molecular Biology of the Cell*, *9*(5), 993–1006. https://doi.org/10.1091/mbc.9.5.993

Yepuri, G., Ramirez, L. M., Theophall, G. G., Reverdatto, S. V., Quadri, N., Hasan, S. N., Bu, L., Thiagarajan, D., Wilson, R., Díez, R. L., Gugger, P. F., Mangar, K., Narula, N., Katz, S. D., Zhou, B., Li, H., Stotland, A. B., Gottlieb, R. A., Schmidt, A. M., … Ramasamy, R. (2023). DIAPH1-MFN2 interaction regulates mitochondria-SR/ER contact and modulates ischemic/hypoxic stress. *Nature Communications*, *14*, 6900. https://doi.org/10.1038/s41467-023-42521-x

Yuan, H., Lin, Y., Wang, J., Li, J., Chen, X., Guo, Y., & Tang, J. (2023). Hypertrophic cardiomyopathy caused by a heterozygous variant in TTR gene: A case report. *Medicine*, *102*(20), e33752. https://doi.org/10.1097/MD.0000000000033752

Zweifel, M. E., & Courtemanche, N. (2020). Competition for delivery of profilin–actin to barbed ends limits the rate of formin-mediated actin filament elongation. *The Journal of Biological Chemistry*, *295*(14), 4513–4525. https://doi.org/10.1074/jbc.RA119.012000

# Appendix

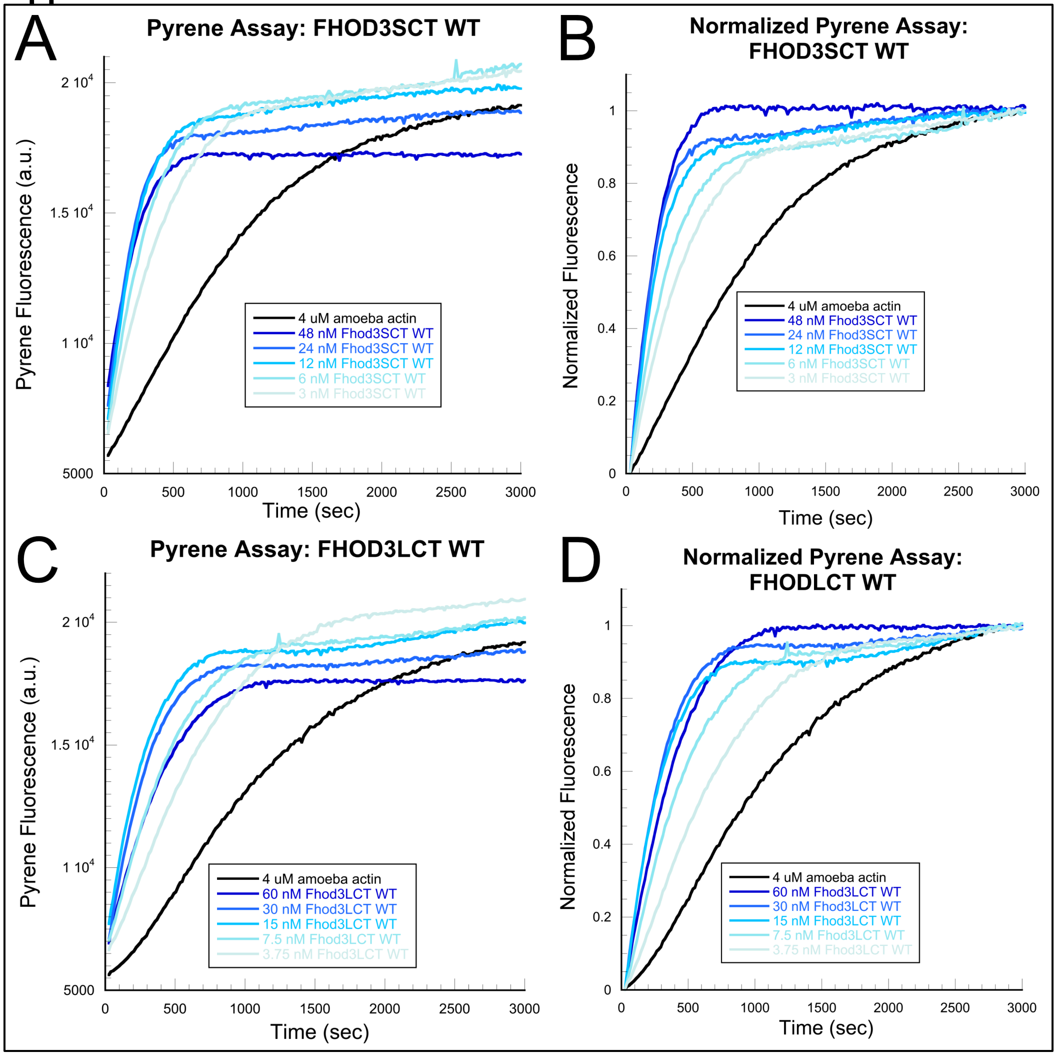

**Figure 2-21** – *FHOD3S/L-CT WT nucleate Acanthamoeba actin more potently than RSA.*

(**A**) Assembly of 4 μM *Acanthamoeba* actin (5% pyrene-labeled) and the indicated concentrations of FHOD3S-CT WT from a 2-fold dilution series. (**B**) Normalization of (**A**). (**C**) Conditions as in (**A**) with FHOD3L-CT WT. (**D**) Normalization of (**C**).

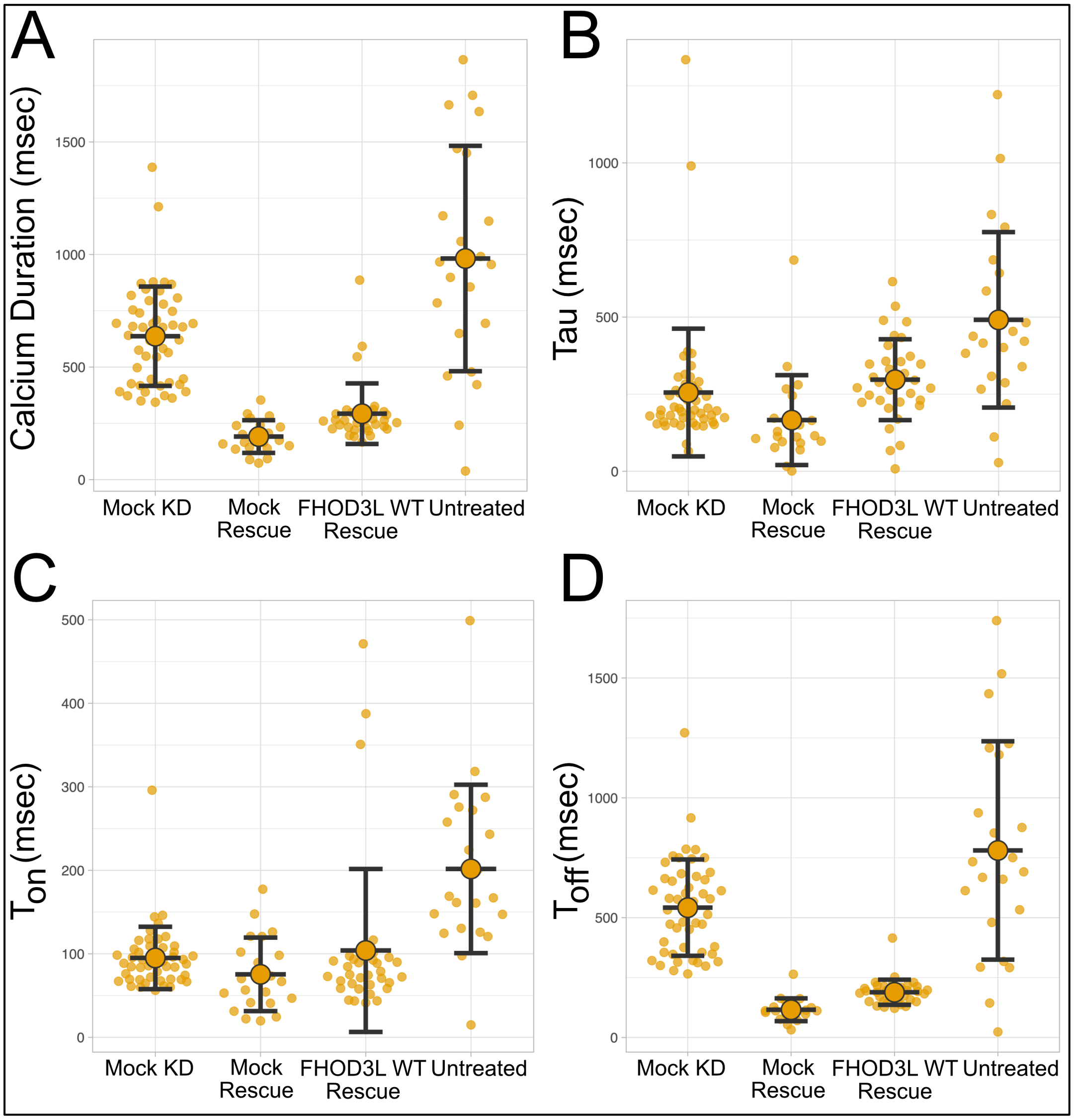

**Figure 2-22** – *Exogenous FHOD3L alters calcium transients in NRVMs.* (**A**) Quantification of calcium transient durations for mock KD, mock rescue, FHOD3L WT rescue, and untreated NRVMs. (1 biological replicate; mean ± SD.) (**B**) Quantification of tau time constant for conditions as in (**A**). (1 biological replicate; mean ± SD.) (**C**) Quantification of time to peak calcium transient for conditions as in (**A**). (1 biological replicate; mean ± SD.) (**D**) Quantification of time to decay for calcium transients for conditions as in (**A**). (1 biological replicate; mean ± SD.)

# Chapter 3: Methylation and phosphorylation of formin homology domain proteins (FHOD1 and FHOD3) by protein arginine methyltransferase 7 (PRMT7) and Rho Kinase (ROCK1)

The work from this chapter is from a collaboration between the Steven G. Clarke and Quinlan labs at UCLA that expands upon a manuscript under review in JBC. Related work not discussed explicitly in this chapter can be viewed in Troy Lowe's dissertation from 2024.

## Introduction

### *Autoinhibition of FHOD-family formins*

As noted in Chapter 1, FHOD-family formins can be autoinhibited when the N-terminal DID binds to the C-terminal DAD (Gould et al., 2011). The C-terminal DAD of formins is located within their tails, which electrostatically interact with actin monomers to help nucleate actin and help the formin stay processively bound to the barbed-ends of filaments (Bremer et al., 2024; Gould et al., 2011; Vizcarra et al., 2014). Within the DAD of FHOD-family formins, ROCK1 has been shown to phosphorylate several residues (S1589, S1595, and T1599, specifically, for FHOD3L) to relieve this autoinhibitory state (Iskratsch et al., 2013). However, it has long been unknown if autoinhibition of formins is an "all-or-nothing" phenomenon or if they can be partially activated in cells by some undetermined mechanism to allow for more precise tuning of formin activity. The data presented in Chapter 2 thoroughly characterized FHOD3S/L's ability to nucleate, elongate, cap, and bundle muscle actin filaments *in vitro*. However, FHOD3S/L's ability to be autoinhibited by N-terminal constructs *in trans* with C-terminal actin assembly constructs had not been tested to date. Additionally, phosphomimetic C-terminal constructs have not been used for FHOD3 to evaluate relief of autoinhibition.

### *Protein arginine methyltransferases*

Proteins can be acetylated, phosphorylated, ubiquitinated, glycosylated, or methylated post-translationally to regulate their functions for specific cellular processes, including muscle regeneration and metabolic homeostasis, among many others (Bedford & Clarke, 2009; Huang et al., 2019; Ramazi et al., 2020; Santos & Lindner, 2017; Wu et al., 2021). Interestingly, post-translational modifications can promote protein misfolding and aggregation and even lead to heart failure in some cases (Del Monte & Agnetti, 2014). Specifically, protein arginine methylation is performed by the family of enzymes known as protein arginine methyltransferases (PRMTs) (Bedford & Clarke, 2009). In eukaryotes, three primary forms of methylarginines are observed: mono-methylarginine (MMA), asymmetric dimethylarginine (ADMA), and symmetric dimethylarginine (SDMA) (Bedford, 2007). There are three categories of PRMTs based on the specific methylarginines they catalyze on proteins (Bedford & Clarke, 2009). Type I PRMTs, such as PRMT1-4, PRMT6, and PRMT8 catalyze ADMA, while type II PRMTs (PRMT5 and PRMT9) mediate the formation of SDMA (Blanc & Richard, 2017; Stouth et al., 2017). PRMT7, however, is a type III enzyme that exclusively catalyzes MMA (Feng et al., 2013). These enzymes tend to recognize glycine and arginine rich (GAR) motifs for methylation, but PRMT7 exclusively recognizes RXR motifs (Feng et al., 2013; Najbauer et al., 1993).

### *Importance of PRMT7 in muscle function*

PRMT7 has been found to be crucial in maintaining skeletal muscle function as *Prmt7*-/- mice exhibit decreased oxidative metabolism and notably reduced endurance exercise capabilities (Blanc et al., 2016; Jeong et al., 2016; So et al., 2021). Moreover, Prmt7 has been shown to promote muscle differentiation through MyoD, a primary regulator of muscle-specific gene expression and differentiation (Jeong et al., 2020). Additionally, there have even been reports implicating Prmt7 in cardiac hypertrophy and sex-specific cardiomyopathy (Ahn et al., 2022, 2024; Blanc et al., 2016, 2017; Jeong et al., 2016). Further, Prmt7 has also been shown to primarily localize in the cytoplasm, suggesting that most of its substrates should, therefore, be cytosolic (Herrmann et al., 2009). Taken together, there is sufficient evidence for FHOD3L and other cytoplasmic actin nucleators to be potentially unidentified substrates for Prmt7 within cardiomyocytes, given FHOD3's recently identified RXR motifs.

In this collaboration, we identified a methylation motif for the methyltransferase, PRMT7, in human FHOD3 and FHOD1 formins within the DAD domain. This methylation motif includes S1589, which is one of the three serine residues that gets phosphorylated by ROCK1 to become activated and prevent DID-DAD dimerization, suggesting that methylation by PRMT7 can play a role in regulating FHOD formin activity in cells (Blanc & Richard, 2017; Gould et al., 2011; Iskratsch et al., 2013). The submitted manuscript characterized the interplay between PRMT7-mediated methylation and ROCK1-mediated phosphorylation at proximal sites on FHOD3 peptides. Surprisingly, we found that human PRMT7 activity was almost completely inhibited in the presence of phosphoserine 1589 on FHOD3 peptides, yet, in stark contrast, ROCK1-mediated phosphorylation was essentially unchanged in the presence of methylated FHOD3 peptides. However, cell-based assays in NRVMs to assess the physiological relevance of PRMT7 and its link to FHOD3L in cardiomyocytes are currently inconclusive.

## Results

### *Characterization of Prmt7 in NRVMs*

We first asked the question if Prmt7 activity is important for structural formation of the sarcomere in NRVMs. To answer this, we performed a siRNA knockdown targeted against Prmt7 in NRVMs via reverse transfection and then fixed and stained the NRVMs four days later for $\alpha$-actinin to assess any structural abnormalities in the sarcomeres. As a result, we did not visually observe a noticeable difference in sarcomere integrity compared to the NRVMs treated with scrambled siRNA (**Fig.3-1A**). We asked if the absence of a detectable phenotype in the Z-lines of sarcomeres was due to insufficient knockdown efficiency at the mRNA level. To answer this, we performed qPCR to quantify the relative reduction in *Prmt7* mRNA from the siRNA knockdown against *Prmt7* in NRVMs. We found that *Prmt7* mRNA was only ~40% reduced compared to negative control-treated NRVMs (**Fig.3-1B**). Despite this, quantifying the sarcomere

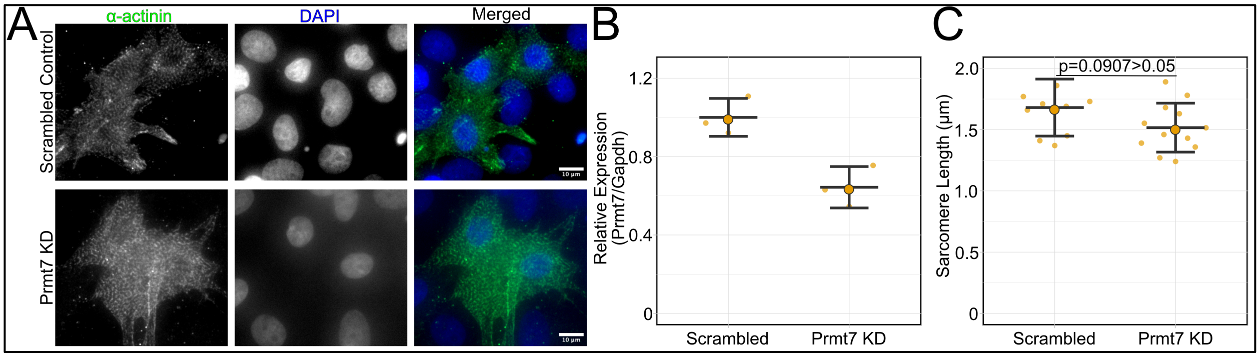

**Figure 3-1** – *Prmt7 knockdown in NRVMs minimally hinders sarcomere structure*

(**A**) Epifluorescent micrographs of NRVMs stained for $\alpha$-actinin (green) and DAPI (blue) and knocked down for Prmt7 (below) or not (top). (**B**) Quantification of knockdown efficiency via qPCR normalized to GAPDH expression. (1 biological replicate, mean $\pm$ SD.) (**C**) Quantification of sarcomere lengths from these conditions. (1 biological replicate, mean $\pm$ SD, p-value by student’s two-sample, unpaired t-test.)

lengths in a small sample of these Prmt7-depleted NRVMs showed a slight, but non-significant reduction compared to the control NRVMs (**Fig.3-1C**). Moreover, the protein stability of Prmt7 and its turnover in muscle cells is not currently known, but it is possible that the NRVMs need to be cultured longer after the initial siRNA knockdown to allow for increased protein degradation of Prmt7, thus increasing the potential severity of the phenotype we observed.

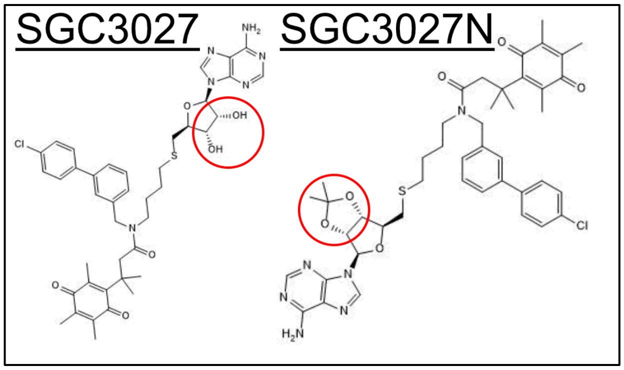

**Figure 3-2** – *Structures of small molecule inhibitors against PRMT7*

Red circle indicates altered functional groups between the primary (left) and control (right) inhibitors.

We asked if inhibiting Prmt7 pharmacologically to bypass the potential protein stability of Prmt7 would result in a stronger phenotype in NRVMs. To evaluate this, we directly inhibited Prmt7 with a small molecule inhibitor, SGC3027, and used a structurally similar inhibitor that does not inhibit Prmt7, SGC3027N, as a negative control (**Fig.3-2**). We tested both inhibitors at 12.5 μM and 25 μM based on a reported IC50 value of 2.4 μM for Prmt7 in HEK293 for methylation of HSP70 (Szewczyk et al., 2020). When categorizing NRVMs into three different classes based on defined sarcomere integrity criteria, we found no notable difference with SGC3027-treated NRVMs compared to the SGC3027N-treated NRVM's (**Fig. 3-3A,B**). Therefore, both SGC3027 and SGC3027N reduce sarcomere integrity to similar extents at higher concentrations, suggesting the presence of off-target effects for both molecules.

Since both siRNA knockdown and pharmacological inhibition of Prmt7 were unsuccessful in producing a noticeable phenotype, we took a different approach to

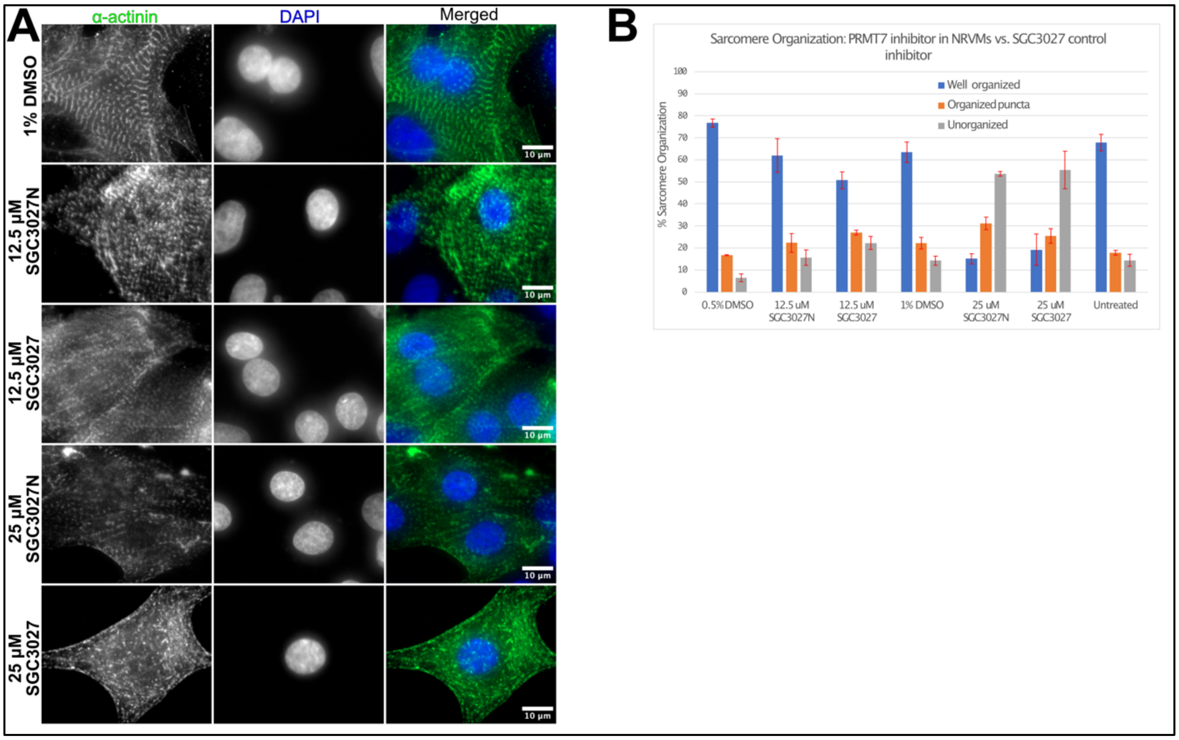

**Figure 3-3** – *Pharmacological inhibition of Prmt7 in NRVMs has off-target effects on sarcomere organization*

(**A**) Epifluorescent micrographs of NRVMs stained for $\alpha$-actinin (green) and DAPI (blue) and treated with the indicated concentrations of either SGC3027 or SGC3027N control. (**B**) Categorization of sarcomere organization for Prmt7-inhibited NRVMs into 3 classes. (1 biological replicate, mean ± SEM.)

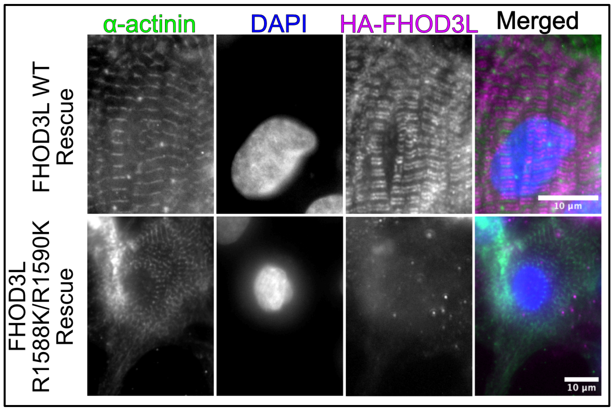

**Figure 3-4** – *Non-methylated FHOD3L rescues sarcomere integrity, but fails to localize to sarcomeres*

Epifluorescent micrographs showing NRVMs from FHOD3L WT or non-methylatable mutant rescues stained for $\alpha$-actinin (green), DAPI (blue), and exogenous HA-FHOD3L (magenta).

determine using rescue experiments in NRVMs with the established protocol from Chapter 2 with an adenovirus driving the expression of a non-methylatable human FHOD3L protein followed by staining the NRVMs for $\alpha$-actinin to assess sarcomere integrity. This approach has the advantage to specifically identify the impact that non-methylated FHOD3L has on sarcomere formation, if any. No major defects in Z-line formation were observed via IF (**Fig.3-4**). However, there has been a large genetic screen performed in *Drosophila melanogaster* in which Dart7, the ortholog of Prmt7, was one of the top hits, in which disruptions to the M-line were observed despite no notable defects in Z-lines (Boulanger et al., 2004; Schnorrer et al., 2010). Interestingly, there was no clear localization of the non-methylatable FHOD3L in NRVMs, in contrast to most other mutants tested in Chapter 2 showing localization along the length of the sarcomeres (**Fig.3-4**). This suggests that somehow preventing Prmt7-mediated methylation of FHOD3L in NRVMs disrupts interactions with cMyBP-C to ultimately prevent it from localizing to sarcomeres, suggesting a higher rate of turnover for non-methylated FHOD3L similar to the R637P HCM-causative mutant in Chapter 2 (Matsuyama et al., 2018). Moreover, this may be due to increased autoinhibition of FHOD3L, thus leading to reduced phosphorylation by casein kinase 2 (CK2) and more binding by p62 at the autophagosomes, as was observed in NRVMs with FHOD3S that can’t be phosphorylated by CK2 (Iskratsch et al., 2010).

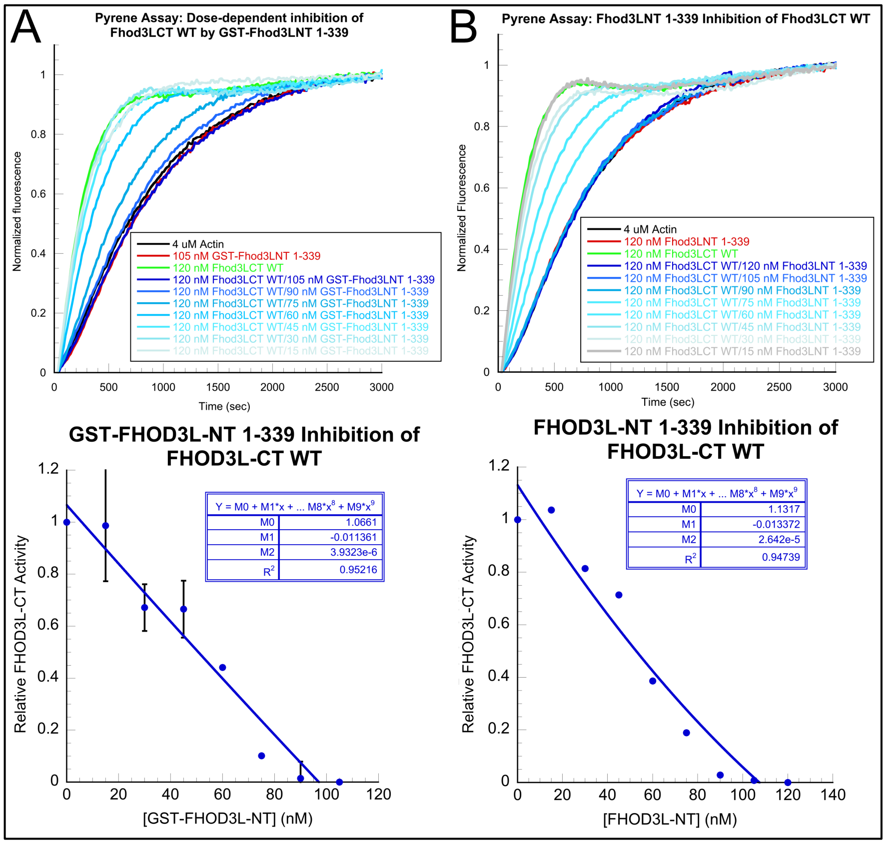

**Figure 3-5** – *FHOD3L-NT 1-339 inhibits FHOD3L-CT WT actin assembly activity*

(**A**) Assembly of 4 µM *Acanthamoeba* actin (5% pyrene-labeled) with 120 nM FHOD3L-CT WT and increasing dose of GST-FHOD3L-NT 1-339 (blue). Quantification of inhibition below (2 biological replicates, mean ± SD.) (**B**) Conditions as in (**A**) with FHOD3L-NT 1-339. Quantification below as in (**A**) with 1 biological replicate.

### *In vitro autoinhibition of FHOD3L*

Although we could not detect phosphorylated FHOD3 peptides via Western blots or dot blots, we determined that the presence of nearby methylarginines does not noticeably effect ROCK1's phosphorylation ability for FHOD3 via mass spectrometry analysis. Despite this, it's still not currently known whether the presence of methylarginines alone in the DAD of FHOD3L measurably affects its ability to form an intramolecular interaction with the DID for autoinhibition. To begin to elucidate this, we first tested the baseline ability for FHOD3L-CT wild-type to be autoinhibited by GST-tagged and untagged FHOD3L-NT 1-339, which has previously been shown to be sufficient for binding the C-terminal half of FHOD3L (Iskratsch et al., 2013). Indeed, we found that the tested FHOD3L-NT constructs similarly inhibited actin assembly activity of FHOD3L-CT wild-type in a dose-dependent manner (**Fig.3-5A,B**). To quantify the relative activity of C-terminal FHOD3L activity with increasing dose of FHOD3L-NT 1-339, we measured the slopes at the $t_{1/8}$ as done in Chapter 2 for each condition with FHOD3L-CT WT as a measure of nucleation strength. We normalized these results to FHOD3L-CT WT nucleation strength in the absence of N-terminal inhibition. After fitting this data to a quadratic binding curve, the inhibition constants ($K_i$) for GST-tagged (55.24 ± 9.12 nM) and untagged FHOD3L-NT 1-339 (53.57 nM) on FHOD3L-CT WT were very similar (**Fig. 3-5A,B**). Therefore, the N-terminal GST tag does not notably interfere with inhibiting FHOD3L-CT wild-type activity.

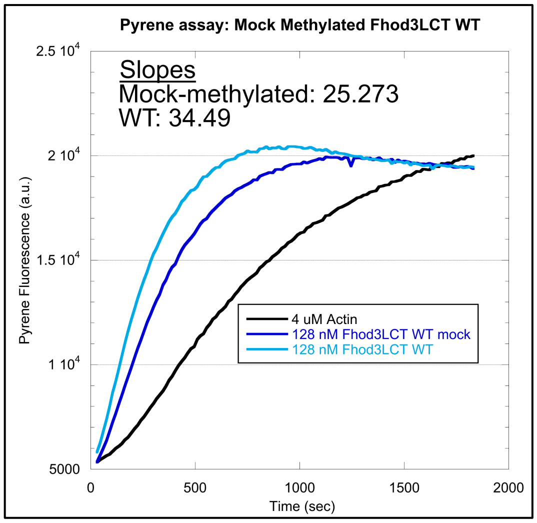

**Figure 3-6** – *Mock methylated FHOD3L-CT WT retains 75% of its activity*

Assembly of 4 μM *Acanthamoeba* actin (5% pyrene-labeled) with 128 nM FHOD3L-CT WT mock-methylated or not. Slopes at $t_{1/8}$ indicated at top of plot (units=a.u./s)

After confirming inhibition of actin assembly activity of FHOD3L-CT WT by its N-terminus, we then wanted to ask how much FHOD3L-CT WT activity is retained after incubating it in a mock *in vitro* methylation assay. To do this, we incubated FHOD3L-CT WT in methylation buffer overnight at 4°C, mimicking the conditions used for *in vitro* methylation assays with PRMT7, and then assessed its activity in a bulk pyrene-actin assembly assay afterwards, with a freshly thawed aliquot of protein used as a positive control (**Fig.3-6**). Surprisingly, we found that FHOD3L-CT WT retained ~75% of its actin assembly activity based on slope measurements at the $t_{1/8}$ to quantify nucleation strengths (**Fig.3-6**). Therefore, it's feasible to methylate FHOD3L-CT WT with PRMT7 *in vitro* for use in downstream actin assembly assays, such as pyrene assays with or without increasing doses of FHOD3L-NT to determine if the $K_i$ changes in the presence of methylation.

## Discussion

### *The role of Prmt7 in cardiomyocytes*

In this chapter, we present evidence that Prmt7 potentially plays an important role in cardiomyocytes at the neonatal stage of development. Most of the work done to understand Prmt7 in muscle to date has been in skeletal muscle, but, interestingly, there have been some reports implicating Prmt7 in cardiac hypertrophy and sex-specific cardiomyopathy (Ahn et al., 2022, 2024; Blanc et al., 2016, 2017; Jeong et al., 2016). More ubiquitously expressed substrates of Prmt7, such as HSP70 and histone H2B, could be contributing to the observed phenotypes from siRNA knockdown and pharmacological inhibition of Prmt7 in NRVMs (Feng et al., 2014; Ramazi et al., 2020; Szewczyk et al., 2020). However, given that FHOD3L is a newly identified substrate for PRMT7 *in vitro* and known to be crucial for sarcomerogenesis in cardiomyocytes, it’s plausible that Prmt7-mediated methylation of FHOD3L contributes to this process (Taniguchi et al., 2009). This would suggest that the stoichiometry of methylation is naturally too low on FHOD3L in NRVMs or the specific effects of non-methylated FHOD3L in NRVMs may not contribute to a strong phenotype in the 48 hours of treatment tested here. Additionally, to determine the turnover of Prmt7 in NRVMs within this treatment time, we can perform a Western blot with commercially available antibodies against Prmt7. Interestingly, one group found FMNL formins to share a novel methyl-binding domain, suggesting that other formins may also interact with methylated substrates, providing an additional role for formins in the context of methyltransferases (Casanova et al., 2024).

Strikingly, we did not observe clear sarcomere localization of exogenous FHOD3L R1588K R1590K from rescue experiments in NRVMs, despite only the N-terminal region of FHOD3L being reported to interact with cMyBP-C to be delivered to the sarcomeres (Matsuyama et al., 2018). Assuming expression levels for this mutant are similar to wild-type, it's possible that a lack of Prmt7-mediated methylation of FHOD3L increases its tendency to be autoinhibited. This lack of localization could potentially reduce phosphorylation by CK2 as well as cMyBP-C's ability to interact with FHOD3L, thus causing it to localize more frequently to autophagosomes (Iskratsch et al., 2010; Matsuyama et al., 2018). Moreover, the lack of localization of FHOD3L to sarcomeres may be consistent with the high prevalence of cMyBP-C mutations implicated in HCM and suggest that a lack of methylated FHOD3L may indirectly contribute to cardiomyopathies on a longer time scale (Ehlermann et al., 2008; Matsuyama et al., 2018).

Despite not observing a clear difference in sarcomere integrity via $\alpha$-actinin staining, sarcomere lengths and Z-line lengths (sarcomere widths) still need to be quantified as done for other rescue experiments in Chapter 2. Moreover, staining for the M-line or thin actin filaments may also reveal more clear phenotypes from these FHOD3L R1588K R1590K-rescued NRVMs similar to what was found in a broad genetic screen in *Drosophila melanogaster*, in which Dart7 was one of the top hits (Schnorrer et al., 2010). Specifically, Dart7 could be knocked down in flies via shRNA driven by the established UAS-gal4 system to then observe any changes to muscle structure after dissection and IF. Overall, the rescue experiment workflow established in NRVMs from Chapter 2 can be more thoroughly applied for non-methylatable FHOD3L such that functional contractility can be assessed alongside quantified sarcomere metrics and then compared to the FHOD3L WT rescue in NRVMs.

### *N-terminal FHOD3L inhibits FHOD3L-CT WT*

We showed that FHOD3L-NT 1-339 can inhibit actin assembly activity of FHOD3L-CT WT in a dose-dependent manner. Although preliminary, we observed an unusual shape of the relative FHOD3L-CT WT activity data in the presence of both GST-tagged and untagged FHOD3L-NT 1-339 when specifically calculating inhibition of nucleation strengths early in the pyrene assay. The lack of a great quadratic fit to this binding curve could simply be a result of not using higher concentrations of FHOD3L-NT 1-339 that would lead to a larger plateau. However, it’s possible that FHOD3L-CT WT’s bundling and capping abilities confound this data set, assuming FHOD3L-CT WT can still bundle or cap actin filaments to some extent even in the presence of FHOD3L-NT 1-339. We can incubate both N-terminal and C-terminal FHOD3L together in different ratios and then phalloidin-stabilize the filaments with fluorescently-labeled phalloidin to observe bundle formation via TIRF microscopy. Similarly, we can perform TIRF seeded elongation assays with varying ratios of N-terminal and C-terminal FHOD3L to observe capping of filaments with fluorescently-labeled actin monomers, as done in Chapter 2. Further, *Acanthamoeba* actin was used in this preliminary work, but given some actin isoform specificity for both FHOD1 and FHOD3, rabbit skeletal muscle actin can be used in the future to compare differences and be more physiologically relevant to cardiomyocytes (Patel et al., 2018). Moreover, it will be interesting to see how the $K_i$ between N-terminal and C-terminal FHOD3S constructs differ given the notable actin assembly differences we observed between FHOD3L-CT WT and FHOD3S-CT WT in Chapter 2.

To better characterize the effect of ROCK1-mediated phosphorylation on autoinhibition relief of FHOD3L-CT, phosphomimetic FHOD3L-CT constructs can be cloned, expressed, and purified to then be used in these pyrene assays similar to this chapter. FHOD3L-CT S1589D, FHOD3L-CT S1595D, FHOD3L-CT T1599D and the combined triple mutant can be used in these pyrene assays to determine if one of these ROCK1 phosphorylation sites reduce autoinhibition more significantly than the other (Iskratsch et al., 2013; Takeya et al., 2008).

Similar to phosphomimetics, but not as widely validated, methylation mimic FHOD3L-CT R1588F R1590F can be cloned, expressed, and purified to ask whether Prmt7-mediated methylation has a significant effect on autoinhibition *in vitro*, despite essentially no observed change in subsequent ROCK1-mediated phosphorylation in the presence of proximal methylarginines (Mostaqul Huq et al., 2006). In this chapter, we began to optimize the experiments needed to validate a methyl mimic and performed experiments suggesting that *in vitro* methylation assays by Prmt7 with FHOD3L-CT WT are feasible to subsequently perform actin assembly assays to observe any potential changes due to methylation in the DAD. The major drawback to *in vitro* methylation of FHOD3L-CT WT is that it would likely be incomplete, in contrast to a homogenous solution of methyl mimic FHOD3L-CT. Tandem mass spectrometry (LC-MS/MS) could be performed after *in vitro* methylation of FHOD3L-CT WT to determine relative proportions of methylated formin. A methyl mimic would not be necessary if a majority of FHOD3L-CT WT in solution is indeed methylated, such that any phenotypes we observe *in vitro* are directly the result of methylated FHOD3L-CT WT and not due to a mixture including non-methylated formin.

Overall, the importance of regulating FHOD3L's actin assembly activity in cardiomyocytes remains elusive. Notably, most of the FHOD3L mutations implicated in HCM are in the N-terminal regulatory regions, with one near the methylation site, V1576G, suggesting that disrupting regulation of FHOD3L could contribute to this disease (**Fig.1-3**) (Ochoa et al., 2018). Moreover, if a methylation mimic FHOD3L-CT R1588F R1590F is validated via *in vitro* ROCK1 phosphorylation assays and similarly results in minimal enhancement of phosphorylation as doubly MMA peptides did, then a full-length methylation mimic could be cloned and used for adenoviral generation to perform rescue experiments in NRVMs with this mimic. By doing this, we can ask the question of whether fully methylated FHOD3L in NRVMs results in any changes to sarcomere integrity or contractile function, assuming that endogenous FHOD3L is not already completely methylated in NRVMs, otherwise we would expect the results to mimic a FHOD3L WT rescue.

## Materials and Methods

### *DNA Constructs*

pGEX-FHOD3L-NT 1-339 was cloned via Gibson Assembly using pCS2+-3xHA-FHOD3L WT and pGEX-FHOD3L-CT WT 963-1622 as templates. pGEX-FHOD3L-CT

WT 963-1622 cloned as described in Chapter 2. pCS2+-3xHA-FHOD3L R1588K/R1590K was generated via site-directed mutagenesis (Liu & Naismith, 2008) from pCS2+-3xHA-FHOD3L WT as a template for adenoviral cloning and generation by VectorBuilder.

### *Protein expression, purification, and labeling*

pGEX-FHOD3L-NT 1-339 was transformed and expressed similarly as described in Chapter 2. Cell pellets expressing GST-FHOD3L-NT 1-339 from *E. coli* were resuspended in extraction buffer (PBS pH 7.4, 1 mM DTT) with 1 mM PMSF and 2 μg/mL DNaseI. All subsequent steps were performed on ice or at 4°C. The cells were lysed by microfluidizing, cleared by centrifugation at 20,000 x g for 20 minutes, and the resulting clarified lysate was incubated with equilibrated glutathione resin for 1 hr, 4°C, nutating. Flow through was collected off the gravity column. Resin was washed with 25 mL extraction buffer and eluted with 15 mL glutathione elution buffer (50mM Tris pH 8.0, 150mM NaCl, 10mM reduced glutathione). The two most concentrated elution fractions were dialyzed into 20 mM Tris pH 8, 150 mM NaCl, 1 mM DTT overnight to be centrifuged at 4°C for 48,000 rpm for 20 minutes, and further purified on a MonoQ anion exchange column (GE Life Sciences) with a gradient of 0.15–0.65 M NaCl over 50 column volumes after 1 column volume of washing at 0.15 M NaCl. Peak fractions were exchanged into storage buffer (10 mM Tris pH 8, 150 mM NaCl, 20% glycerol, 1 mM DTT), then flash frozen in liquid nitrogen and stored at -80°C. FHOD3L-NT 1-339 was purified similarly, but cleaved during dialysis overnight, and then filtered through glutathione resin. The resulting flowthrough was exchanged into storage buffer (10 mM

Tris pH 8, 150 mM NaCl, 20% glycerol, 1 mM DTT), then flash frozen in liquid nitrogen and stored at -80°C.

For this chapter, protein concentrations for C-terminal and N-terminal FHOD3L constructs were calculated using Beer's law: A= $\varepsilon$bc where A is the absorbance at 280 nm, $\varepsilon$ is the extinction coefficient, b is the path length (1 cm), and c is the concentration. GST-FHOD3L-NT 1-339 concentration was determined above with extinction coefficient 68,760 $M^{-1}$ $cm^{-1}$. Fhod3L NT 1-339 was determined as above with extinction coefficient 25,900 $M^{-1}$ $cm^{-1}$. FHOD3L-CT WT 963-1622 concentration was determined above with extinction coefficient 55,920 $M^{-1}$ $cm^{-1}$. All concentrations reported as dimer concentrations.

*Acanthamoeba castellani* actin was purified and labeled with pyrene iodoacetamide (Thermo Scientific) as described with modifications (Sun et al., 2018; Zuchero, 2007).

### *Pyrene Assays*

Pyrene assays were performed as described in Chapter 2. Quantification of relative inhibition was calculated by taking the slopes at $t_{1/8}$ as done in Chapter 2, but subtracting the slope of the highest FHOD3L-NT concentration tested from the FHOD3L-CT WT alone slope (no NT) before normalizing to the FHOD3L-CT WT slope such that values range from 0 – 1.

### *Adenoviral generation, purification, and infection*

Crude adenovirus containing pAV-CMV-{3xHA-FHOD3L R1588K R1590K}:SV40 pA-CMV-mCherry was commercially generated and purchased from VectorBuilder. Purification and titer determination for this virus was performed as described in Chapter 2.

*Neonatal rat ventricular myocyte seeding, siRNA knockdown, and rescue*

Reverse transfection of Prmt7 and Fhod3 siRNA were performed as described in Chapter 2. Prmt7-specific siRNA (Qiagen, Rn_LOC361402_1 Flexitube siRNA) was used in NRVMs. Rescue experiments were performed as described in Chapter 2.

*Small molecule inhibition of Prmt7*

Working stocks of SGC3027 and SGC3027N small molecule inhibitors of Prmt7 (Sigma) were diluted in DMSO (Sigma) as a vehicle and further diluted in media for treatment in NRVMs for 48 hours. Media used as described in Chapter 2.

*Immunofluorescence and image analysis*

NRVMs were fixed and stained as described in Chapter 2 without Wheat Germ Agglutinin (WGA) TMR (Thermo Fisher). 16-bit images were acquired on an AXIO Imager.D1 fluorescence phase contrast microscope (Zeiss) using an EC Plan-Neofluar 40x M27 (0.75 NA) objective lens or Plan-Apochromat oil DIC M27 63x (1.4 NA) objective lens with an AxioCam MRm camera (Zeiss). Sarcomere analysis was performed manually in a single-blind manner as described in Chapter 2.

*Western blot and dot blots*

4-20% Tris-Glycine gradient gels (Thermo Fisher, XP04205BOX) were used to resolve purified FHOD3L-CT WT protein and FHOD3 peptides (Lowe et al., 2024) after *in vitro* ROCK1 phosphorylation assays as described (Lowe et al., 2024). Western blots were otherwise performed similarly as described in Chapter 2, blotted with phosphoserine/threonine polyclonal rabbit antibody (ECM Biosciences) diluted 1:1000 in low-salt TBST, rotating in 4°C overnight.

Dot blots were performed by dotting 10 uL of samples used in the Western blot after *in vitro* ROCK1 phosphorylation on equilibrated PVDF membrane rinsed in low-salt TBST (20 mM Tris pH 7.6, 150 mM NaCl, 0.05% Tween-20, 0.01% sodium azide). PVDF membrane was left out at room temperature above a piece of filter paper equilibrated in low salt TBST that was on top of a dry piece of filter paper to fix the proteins onto the membrane before primary antibody incubation overnight at 4°C. Washes and secondary antibody incubation were performed similarly as described in Chapter 2. Dot blots that were Coomassie-stained were stained after protein fixation.

### *Statistical analysis*

Student’s two-sample t-test was used in Fig.3-1C as both treatments were normally distributed based on the Shapiro-Wilk test.

## References

Ahn, B.-Y., Jeong, M.-H., Pyun, J.-H., Jeong, H.-J., Vuong, T. A., Bae, J.-H., An, S., Kim, S. W., Kim, Y. K., Ryu, D., Kim, H.-J., Cho, H., Bae, G.-U., & Kang, J.-S. (2022). PRMT7 ablation in cardiomyocytes causes cardiac hypertrophy and fibrosis through β-catenin dysregulation. *Cellular and Molecular Life Sciences*, *79*(2), 99. https://doi.org/10.1007/s00018-021-04097-x

Ahn, B.-Y., Zhang, Y., Wei, S., Jeong, Y., Park, D.-H., Lee, S.-J., Leem, Y.-E., & Kang, J.-S. (2024). Prmt7 regulates the JAK/STAT/Socs3 signaling pathway in postmenopausal cardiomyopathy. *Experimental & Molecular Medicine*, *56*(3), 711–720. https://doi.org/10.1038/s12276-024-01193-3

Bedford, M. T. (2007). Arginine methylation at a glance. *Journal of Cell Science*, *120*(24), 4243–4246. https://doi.org/10.1242/jcs.019885

Bedford, M. T., & Clarke, S. G. (2009). Protein Arginine Methylation in Mammals: Who, What, and Why. *Molecular Cell*, *33*(1), 1–13. https://doi.org/10.1016/j.molcel.2008.12.013

Blanc, R. S., & Richard, S. (2017). Regenerating muscle with arginine methylation. *Transcription*, *8*(3), 175–178. https://doi.org/10.1080/21541264.2017.1291083

Blanc, R. S., Vogel, G., Chen, T., Crist, C., & Richard, S. (2016). PRMT7 Preserves Satellite Cell Regenerative Capacity. *Cell Reports*, *14*(6), 1528–1539. https://doi.org/10.1016/j.celrep.2016.01.022

Blanc, R. S., Vogel, G., Li, X., Yu, Z., Li, S., & Richard, S. (2017). Arginine Methylation by PRMT1 Regulates Muscle Stem Cell Fate. *Molecular and Cellular Biology*, *37*(3), e00457-16. https://doi.org/10.1128/MCB.00457-16

Boulanger, M.-C., Miranda, T. B., Clarke, S., Di Fruscio, M., Suter, B., Lasko, P., & Richard, S. (2004). Characterization of the Drosophila protein arginine methyltransferases DART1 and DART4. *The Biochemical Journal*, *379*(Pt 2), 283–289. https://doi.org/10.1042/BJ20031176

Bremer, K. V., Wu, C., Patel, A. A., He, K. L., Grunfeld, A. M., Chanfreau, G. F., & Quinlan, M. E. (2024). Formin tails act as a switch, inhibiting or enhancing processive actin elongation. *The Journal of Biological Chemistry*, *300*(1), 105557. https://doi.org/10.1016/j.jbc.2023.105557

Casanova, A. G., Roth, G. S., Hausmann, S., Lu, X., Bischoff, L. J. M., Froeliger, E. M., Belmudes, L., Bourova-Flin, E., Flores, N. M., Benitez, A. M., Chasan, T., Caporicci, M., Vayr, J., Blanchet, S., Ielasi, F., Rousseaux, S., Hainaut, P., Gozani, O., Le Romancer, M., … Reynoird, N. (2024). Cytoskeleton remodeling induced by SMYD2 methyltransferase drives breast cancer metastasis. *Cell Discovery*, *10*(1), 1–22. https://doi.org/10.1038/s41421-023-00644-x

Del Monte, F., & Agnetti, G. (2014). Protein post-translational modifications and misfolding: New concepts in heart failure. *Proteomics. Clinical Applications*, *8*(7–8), 534–542. https://doi.org/10.1002/prca.201400037

Ehlermann, P., Weichenhan, D., Zehelein, J., Steen, H., Pribe, R., Zeller, R., Lehrke, S., Zugck, C., Ivandic, B. T., & Katus, H. A. (2008). Adverse events in families with hypertrophic or dilated cardiomyopathy and mutations in the MYBPC3gene. *BMC Medical Genetics*, *9*(1), 95. https://doi.org/10.1186/1471-2350-9-95

Feng, Y., Hadjikyriacou, A., & Clarke, S. G. (2014). Substrate Specificity of Human Protein Arginine Methyltransferase 7 (PRMT7). *The Journal of Biological Chemistry*, *289*(47), 32604–32616. https://doi.org/10.1074/jbc.M114.609271

Feng, Y., Maity, R., Whitelegge, J. P., Hadjikyriacou, A., Li, Z., Zurita-Lopez, C., Al-Hadid, Q., Clark, A. T., Bedford, M. T., Masson, J.-Y., & Clarke, S. G. (2013). Mammalian Protein Arginine Methyltransferase 7 (PRMT7) Specifically Targets RXR Sites in Lysine- and Arginine-rich Regions. *The Journal of Biological Chemistry*, *288*(52), 37010–37025. https://doi.org/10.1074/jbc.M113.525345

Gould, C. J., Maiti, S., Michelot, A., Graziano, B. R., Blanchoin, L., & Goode, B. L. (2011). The Formin DAD Domain Plays Dual Roles in Autoinhibition and Actin Nucleation. *Current Biology*, *21*(5), 384–390. https://doi.org/10.1016/j.cub.2011.01.047

Herrmann, F., Pably, P., Eckerich, C., Bedford, M. T., & Fackelmayer, F. O. (2009). Human protein arginine methyltransferases in vivo—Distinct properties of eight canonical members of the PRMT family. *Journal of Cell Science*, *122*(Pt 5), 667–677. https://doi.org/10.1242/jcs.039933

Huang, K.-Y., Lee, T.-Y., Kao, H.-J., Ma, C.-T., Lee, C.-C., Lin, T.-H., Chang, W.-C., & Huang, H.-D. (2019). dbPTM in 2019: Exploring disease association and cross-talk of post-translational modifications. *Nucleic Acids Research*, *47*(Database issue), D298–D308. https://doi.org/10.1093/nar/gky1074

Iskratsch, T., Lange, S., Dwyer, J., Kho, A. L., Remedios, C. dos, & Ehler, E. (2010). Formin follows function: A muscle-specific isoform of FHOD3 is regulated by CK2 phosphorylation and promotes myofibril maintenance. *Journal of Cell Biology*, *191*(6), 1159–1172. https://doi.org/10.1083/jcb.201005060

Iskratsch, T., Reijntjes, S., Dwyer, J., Toselli, P., Dégano, I. R., Dominguez, I., & Ehler, E. (2013). Two distinct phosphorylation events govern the function of muscle FHOD3. *Cellular and Molecular Life Sciences : CMLS*, *70*(5), 893–908. https://doi.org/10.1007/s00018-012-1154-7

Jeong, H.-J., Lee, H.-J., Vuong, T. A., Choi, K.-S., Choi, D., Koo, S.-H., Cho, S. C., Cho, H., & Kang, J.-S. (2016). Prmt7 Deficiency Causes Reduced Skeletal Muscle Oxidative Metabolism and Age-Related Obesity. *Diabetes*, *65*(7), 1868–1882. https://doi.org/10.2337/db15-1500

Jeong, H.-J., Lee, S.-J., Lee, H.-J., Kim, H.-B., Anh Vuong, T., Cho, H., Bae, G.-U., & Kang, J.-S. (2020). Prmt7 promotes myoblast differentiation via methylation of p38MAPK on arginine residue 70. *Cell Death & Differentiation*, *27*(2), 573–586. https://doi.org/10.1038/s41418-019-0373-y

Liu, H., & Naismith, J. H. (2008). An efficient one-step site-directed deletion, insertion, single and multiple-site plasmid mutagenesis protocol. *BMC Biotechnology*, *8*, 91. https://doi.org/10.1186/1472-6750-8-91

Matsuyama, S., Kage, Y., Fujimoto, N., Ushijima, T., Tsuruda, T., Kitamura, K., Shiose, A., Asada, Y., Sumimoto, H., & Takeya, R. (2018). Interaction between cardiac myosin-binding protein C and formin Fhod3. *Proceedings of the National Academy of Sciences*, *115*(19), E4386–E4395. https://doi.org/10.1073/pnas.1716498115

Mostaqul Huq, M. D., Gupta, P., Tsai, N.-P., White, R., Parker, M. G., & Wei, L.-N. (2006). Suppression of receptor interacting protein 140 repressive activity by protein arginine methylation. *The EMBO Journal*, *25*(21), 5094–5104. https://doi.org/10.1038/sj.emboj.7601389

Najbauer, J., Johnson, B. A., Young, A. L., & Aswad, D. W. (1993). Peptides with sequences similar to glycine, arginine-rich motifs in proteins interacting with RNA are efficiently recognized by methyltransferase(s) modifying arginine in numerous proteins. *Journal of Biological Chemistry*, *268*(14), 10501–10509. https://doi.org/10.1016/S0021-9258(18)82227-X

Ochoa, J. P., Sabater-Molina, M., García-Pinilla, J. M., Mogensen, J., Restrepo-Córdoba, A., Palomino-Doza, J., Villacorta, E., Martinez-Moreno, M., Ramos-Maqueda, J., Zorio, E., Peña-Peña, M. L., García-Granja, P. E., Rodríguez-Palomares, J. F., Cárdenas-Reyes, I. J., de la Torre-Carpente, M. M., Bautista-Pavés, A., Akhtar, M. M., Cicerchia, M. N., Bilbao-Quesada, R., … Monserrat, L. (2018). Formin Homology 2 Domain Containing 3 (FHOD3) Is a Genetic Basis for Hypertrophic Cardiomyopathy. *Journal of the American College of Cardiology*, *72*(20), 2457–2467. https://doi.org/10.1016/j.jacc.2018.10.001

Patel, A. A., Oztug Durer, Z. A., van Loon, A. P., Bremer, K. V., & Quinlan, M. E. (2018). Drosophila and human FHOD family formin proteins nucleate actin filaments. *The Journal of Biological Chemistry*, *293*(2), 532–540. https://doi.org/10.1074/jbc.M117.800888

Ramazi, S., Allahverdi, A., & Zahiri, J. (2020). Evaluation of post-translational modifications in histone proteins: A review on histone modification defects in developmental and neurological disorders. *Journal of Biosciences*, *45*(1), 135. https://doi.org/10.1007/s12038-020-00099-2

Santos, A. L., & Lindner, A. B. (2017). Protein Posttranslational Modifications: Roles in Aging and Age-Related Disease. *Oxidative Medicine and Cellular Longevity*, *2017*, 5716409. https://doi.org/10.1155/2017/5716409

Schnorrer, F., Schönbauer, C., Langer, C. C. H., Dietzl, G., Novatchkova, M., Schernhuber, K., Fellner, M., Azaryan, A., Radolf, M., Stark, A., Keleman, K., & Dickson, B. J. (2010). Systematic genetic analysis of muscle morphogenesis and function in Drosophila. *Nature*, *464*(7286), 287–291. https://doi.org/10.1038/nature08799

So, H.-K., Kim, S., Kang, J.-S., & Lee, S.-J. (2021). Role of Protein Arginine Methyltransferases and Inflammation in Muscle Pathophysiology. *Frontiers in Physiology*, *12*. https://doi.org/10.3389/fphys.2021.712389

Stouth, D. W., vanLieshout, T. L., Shen, N. Y., & Ljubicic, V. (2017). Regulation of Skeletal Muscle Plasticity by Protein Arginine Methyltransferases and Their Potential Roles in Neuromuscular Disorders. *Frontiers in Physiology*, *8*. https://doi.org/10.3389/fphys.2017.00870

Sun, H., Luo, Y., & Miao, Y. (2018). Purification of Globular Actin from Rabbit Muscle and Pyrene Fluorescent Assays to Investigate Actin Dynamics in vitro. *Bio-Protocol*, *8*(23), e3102. https://doi.org/10.21769/BioProtoc.3102

Szewczyk, M. M., Ishikawa, Y., Organ, S., Sakai, N., Li, F., Halabelian, L., Ackloo, S., Couzens, A. L., Eram, M., Dilworth, D., Fukushi, H., Harding, R., dela Seña, C. C., Sugo, T., Hayashi, K., McLeod, D., Zepeda, C., Aman, A., Sánchez-Osuna, M., … Barsyte-Lovejoy, D. (2020). Pharmacological inhibition of PRMT7 links arginine monomethylation to the cellular stress response. *Nature Communications*, *11*(1), 1–15. https://doi.org/10.1038/s41467-020-16271-z

Takeya, R., Taniguchi, K., Narumiya, S., & Sumimoto, H. (2008). The mammalian formin FHOD1 is activated through phosphorylation by ROCK and mediates thrombin-induced stress fibre formation in endothelial cells. *The EMBO Journal*, *27*(4), 618–628. https://doi.org/10.1038/emboj.2008.7

Taniguchi, K., Takeya, R., Suetsugu, S., Kan-o, M., Narusawa, M., Shiose, A., Tominaga, R., & Sumimoto, H. (2009). Mammalian formin Fhod3 regulates actin assembly and sarcomere organization in striated muscles. *Journal of Biological Chemistry*, *284*(43), 29873–29881. https://doi.org/10.1074/jbc.M109.059303

Vizcarra, C. L., Bor, B., & Quinlan, M. E. (2014). The Role of Formin Tails in Actin Nucleation, Processive Elongation, and Filament Bundling. *The Journal of Biological Chemistry*, *289*(44), 30602–30613. https://doi.org/10.1074/jbc.M114.588368

Wu, Q., Schapira, M., Arrowsmith, C. H., & Barsyte-Lovejoy, D. (2021). Protein arginine methylation: From enigmatic functions to therapeutic targeting. *Nature Reviews. Drug Discovery*, *20*(7), 509–530. https://doi.org/10.1038/s41573-021-00159-8

Zuchero, J. B. (2007). In Vitro Actin Assembly Assays and Purification From Acanthamoeba. In A. S. Coutts (Ed.), *Adhesion Protein Protocols* (pp. 213–226). Humana Press. https://doi.org/10.1007/978-1-59745-353-0_15

## Appendix

### *Detecting ROCK1-mediated phosphorylation of FHOD3L*

We asked if FHOD3L's lack of localization in NRVMs was linked to its phosphorylation and autoinhibition. The goal that we set out to accomplish was to optimize detection of phosphorylated FHOD3 peptides such that *in vitro* methylation assays can be performed prior to *in vitro* phosphorylation assays to identify any possible inhibition or enhancement of ROCK1-mediated phosphorylation in the presence of nearby methylarginines before ordering doubly MMA peptides of FHOD3. To determine this, we first performed *in vitro* ROCK1 phosphorylation assays with MBP-tagged FHOD3L tail as previously done (Lowe et al., 2024) (Iskratsch et al., 2013). We confirmed successful ROCK1-mediated phosphorylation of MBP-FHOD3L tail via Western blot, but did not detect commercially available phosphorylated FHOD3 peptides due to peptides passing through the PVDF membrane, running off the polyacrylamide gel, or not interacting with primary antibody (**Fig.3-7A**).

To potentially solve these issues, we asked if directly aliquoting a solution containing phosphorylated FHOD3 peptides directly onto equilibrated PVDF membrane could be detected via Western blot. As a result, we still did not detect phosphorylated FHOD3 peptides, but did detect phosphorylated FHOD3L-CT wild-type and ROCK1 itself (**Fig.3-7B**). To confirm if the peptides were being washed out from the PVDF membrane during the antibody incubations and washes, we repeated this dot blot of peptides, but Coomassie-stained the membrane instead. We found the same result of detectable FHOD3L-CT wild-type and undetected FHOD3 peptides from the Coomassie-stained membrane (**Fig.3-7C**). Therefore, the peptides are not being retained on PVDF membrane after any washes in TBST before staining.

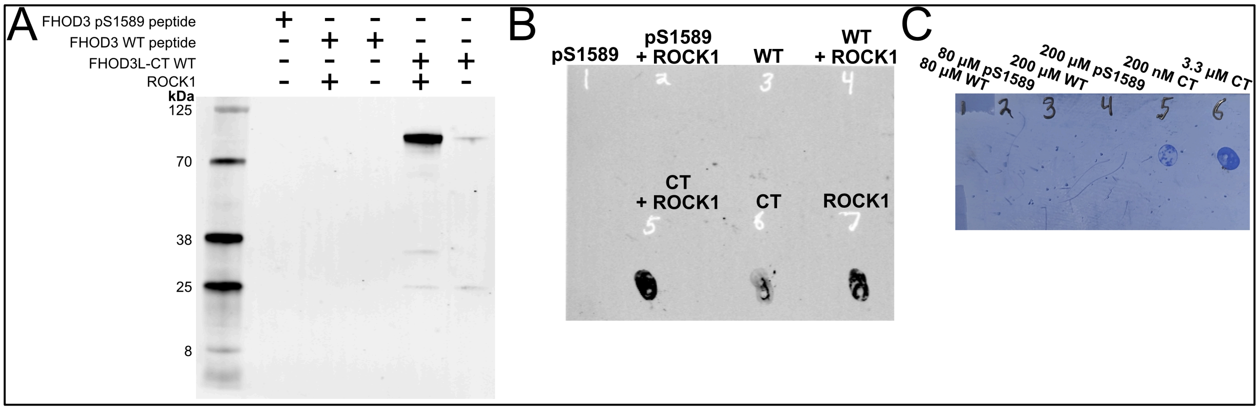

**Figure 3-7** – *Phosphorylated FHOD3 peptides are not retained on PVDF membranes*

(**A**) Western blot for $\alpha$-pS/T after an *in vitro* ROCK1 phosphorylation assay with FHOD3L-CT WT and peptides. (**B**) Dot blot of peptides (pS1589=FHOD3 pS1589, WT=FHOD3 peptide) and FHOD3L-CT WT (CT) in the presence or absence of ROCK1-mediated phosphorylation. (**C**) Coomassie-stained PVDF membrane after dotting either FHOD3L-CT WT or peptides.

# Chapter 4: Optimizing the sarcApp Output for NRVMs

## Introduction

### *Sarcomere measurement programs*

As shown in previous chapters, the sarcomere is the fundamental contractile unit for all striated muscle cells, such as cardiomyocytes (A. F. Huxley & Niedergerke, 1954; H. Huxley & Hanson, 1954; Palmer et al., 2020). Myofibrillogenesis begins near the cell edge with formation of pre-myofibrils composed of less mature Z-bodies, which eventually merge to form more mature Z-lines in developed sarcomeres (Fenix et al., 2018). Sarcomeres are highly organized and composed of thin actin filaments that interdigitate the thick myosin filaments, where the thin actin filaments are bound to the proteinaceous Z-lines made up of $\alpha$-actinin, among other proteins (**Fig.1-3**) (Pirani et al., 2006). In order to understand how certain treatments alter this contractile structure, many labs have used various different programs or methods, such as SarcTrack or ImageJ's DDecon plugin, to measure thin filament length, sarcomere length, and other sarcomere metrics in a semi-autonomous manner, or more typically, manually analyzing sarcomeres on imageJ (Littlefield & Fowler, 2002; Toepfer et al., 2019). These methods, while fairly accurate, are low-throughput, making measurements of many sarcomeres and cells an extremely daunting task to approach any statistical significance. A new, high-throughput, user-friendly, and unbiased sarcomere measuring program, known as sarcApp, was developed by the Burnette lab and trained on stem cell-derived cardiomyocytes (Neininger-Castro et al., 2023).

To properly use sarcApp, users must acquire a high-quality confocal image of cardiomyocytes stained for either $\alpha$-actinin, titin, or myomesin, and then perform mathematical deconvolution (the Burnette lab uses a commercially available

Microvolution software), followed by running this processed image through a deep-learning yoU-NET binarization program to output an 8-bit prediction map of the image. This 8-bit prediction map can then be easily thresholded on imageJ to ensure all the features of interest are in the foreground, but all images should be thresholded similarly for fair comparisons. Once a true binary image has been produced by these methods, the binarized image can then be input into sarcApp using their python-based graphical user interface (GUI). SarcApp then computes the number of Z-bodies per cell, number of Z-lines per cell, sarcomere length, numbers of myofibrils per cell, among many other metrics, based off the indicated spatial resolution and provides an overlay of the identified Z-lines and Z-bodies from the binary image.

Although sarcApp sounds attractive and functionally useful for efficient research, it seems to exclusively work for sparsely plated cardiomyocytes and was not trained on more mature NRVMs either, but rather trained on the human induced pluripotent stem cell-derived cardiomyocytes (hiCMs). To attempt to make sarcApp more broadly useful, we merged Python code from Cellpose and sarcApp to allow it to iteratively measure multiple single cell segments in a single image, as opposed to exclusively working with single cell images.

## Results

### *Merged Cellpose & sarcApp code*

To assess sarcApp's accuracy in identifying Z-lines and myofibrils within NRVMs, we first wanted to input an epifluorescent micrograph of NRVM's with organized sarcomeres from the FHOD3L wild-type rescue, as seen throughout Chapter 2. After specifically inputting the $\alpha$-actinin channel from an image of FHOD3L wild-type rescued-NRVMs into the default version of sarcApp, we found that the yoU-Net deep learning binarization model removes most of the background from the image, compared to standard Otsu thresholding on imageJ (**Fig.4-1**). However, we found that the resulting quantification and identification of Z-lines and myofibrils by sarcApp has a fairly high false negative rate, in addition to some false positives (**Fig.4-1**). In addition to this, the built-in cell segmentation code within sarcApp did not work for confluent NRVMs, as the output data registered the entire image as one cardiomyocyte, thus invalidating the “per cardiomyocyte” metrics that sarcApp generates.

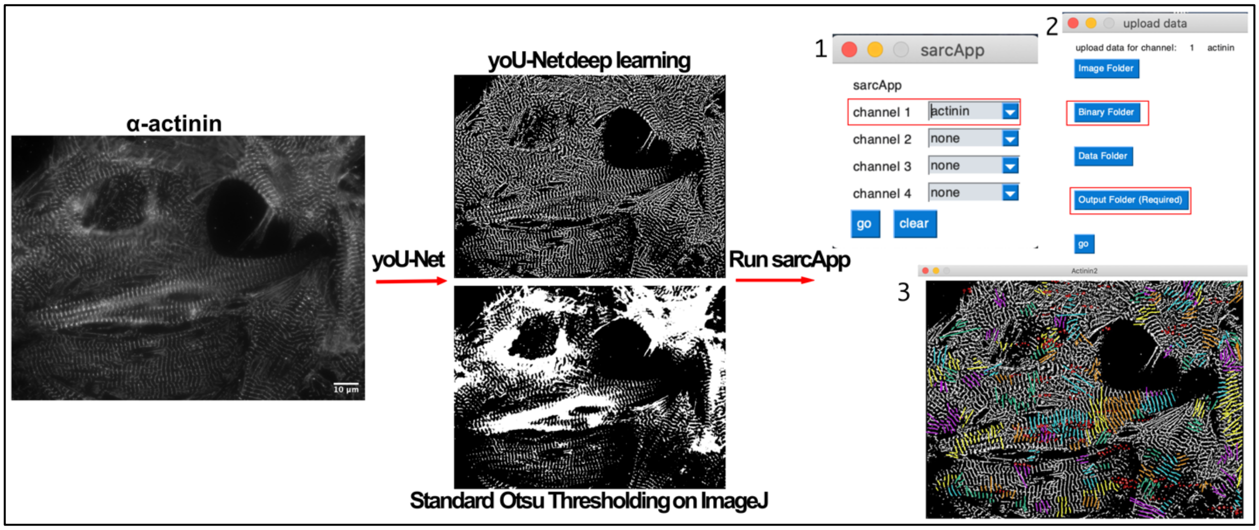

channel 1 actinin
channel 2 none
channel 3 none
channel 4 none

upload data for channel: 1 actinin

**Figure 4-1** – *Overview of sarcApp with NRVMs.*

The raw $\alpha$-actinin image is on the left, and then processed with either yoU-Net deep learning binarization (top) or Otsu thresholding on imageJ (bottom) and then the resulting binary image is input into sarcApp for automated, unbiased sarcomere measurements. Z-lines are color-coded by identified myofibrils (bottom right).

To attempt to resolve this, we merged the Cellpose single cell segmentation code with the sarcApp code (Stringer et al., 2021). This task required adding the NPY file from Cellpose as an argument in a new function within sarcApp’s edge detection code to identify each single cell outline as a pickle object in Python, which is compatible with sarcApp (see Methods for more details and link to GitHub branch). Moreover, we wanted to maintain the cell segmentation numbering by Cellpose to ensure that it correlates with the single cell data output by sarcApp so that we can revisit specific cardiomyocytes or compare if needed. We found that small cell segment artifacts erroneously generated by Cellpose resulted in identified pickle objects, albeit not true cardiomyocytes. We resolved this issue by setting a minimum size limit for each cell segment within the newly revised edge detection code. Therefore, we developed a new addition to the Python-based code in sarcApp to allow single cell segmentation outputs by Cellpose to be compatible with sarcApp.

To enhance the throughput for this merged Cellpose and sarcApp code, we wrote several imageJ macros. First, an imageJ macro can be used to save the single desired channel from an entire folder of CZI images, such as $\alpha$-actinin for example (see Methods). Next, yoU-Net binarization can be performed in bulk as described in the sarcApp GitHub (Neininger-Castro et al., 2023). Since yoU-Net binarization causes the images scaling factor in the metadata to be lost and it's required for proper measurements by sarcApp, another imageJ macro can be used to regenerate the scaling factor for binary images in bulk (see Methods). Next, the newly revised edge detection code can be run via ipython in the terminal to then generate an individual pickle object per every reasonably sized cell segment. Finally, one last imageJ macro can be run to threshold the binary image and quantify the particles within each cell segment and iterate over each image in a given folder (see Methods). The newly generated CSV files corresponding to each single cell segment can be used in parallel with the pickle objects as inputs in the data folder for sarcApp (**Fig.4-1**). Overall, these imageJ macros help increase the throughput for sarcApp while maintaining the merged code compatible with Cellpose.

### *Optimization of image acquisition for sarcApp*

After optimizing the sarcApp code and making it compatible with confluent patches of cells using Cellpose, we wanted to evaluate the accuracy of sarcApp's unbiased quantification of sarcomeres and myofibrils. To determine this, we applied our new code described above to FHOD3 knockdown NRVMs and FHOD3L wild-type-rescued NRVMs to compare the quantified sarcomere metrics from both extremes of sarcomere organization to what we visually observed via IF. As a result, we found that sarcApp's identification of sarcomeres and myofibrils was not consistent with our manually analyzed results, where sarcApp failed to identify many sarcomeres in the FHOD3L wild-type images (**Fig.4-2A,B**). Conversely, the FHOD3 knockdown NRVMs with visually fewer sarcomeres per NRVM are more accurately processed via sarcApp

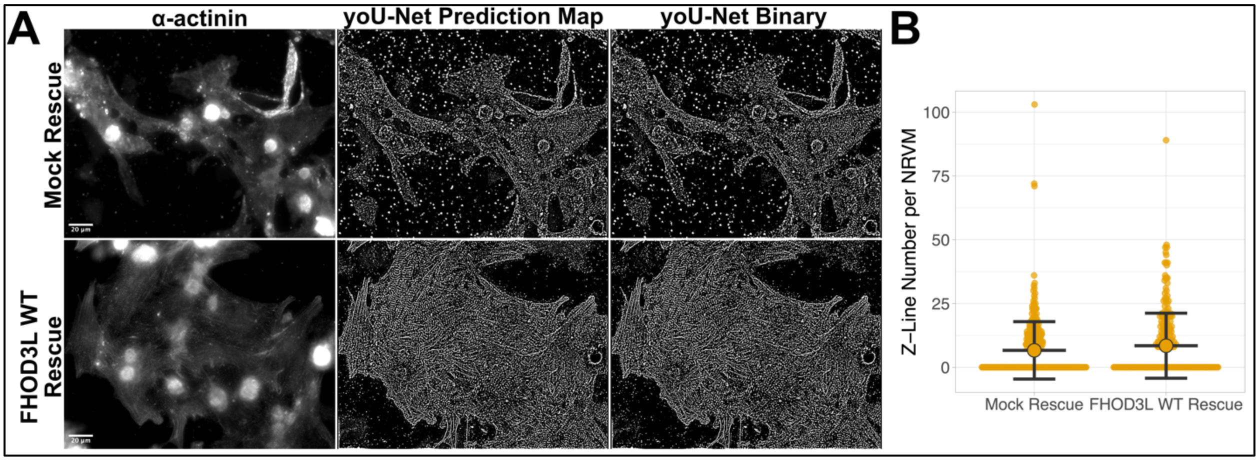

**Figure 4-2** – *sarcApp Z-line identification is not consistent with IF of NRVMs.*

(**A**) Raw $\alpha$-actinin image (left), 8-bit prediction map from yoU-Net (middle), and binarized image (right) from either mock rescued or FHOD3L wild-type-rescued NRVMs. (**B**) Quantification by sarcApp of Z-Line number per NRVM from binarized images as in (**A**). (Mock: n= 311;WT: n=246;mean ± SD; 1 biological replicate.)

than the FHOD3L wild-type-rescued NRVMs that contain more sarcomeres (**Fig.4-2A,B**). Therefore, the binarized images acquired on the widefield microscope are not sufficiently resolved to allow for accurate identification of Z-lines with confluent NRVMs, despite utilizing Cellpose.

We then wanted to compare the quantification from sarcApp to what we manually measured from the NRVM rescue experiments and controls in Chapter 2. It's important to note that we cannot make a direct comparison between sarcApp's average Z-line number per NRVM measurement compared to our manual sarcomere number per NRVM measurements due to varying numbers of sarcomeres being in parallel or in series with each other. Despite this, we found that average Z-line number per NRVM is noticeably lower by sarcApp quantification (8 ± 13 Z-lines) than manual measurements (19 ± 14 sarcomeres) for FHOD3L wild-type-rescued NRVMs (**Fig.4-2B**). However, we found that the sarcApp quantification of average Z-line number per NRVM (7 ± 11 Z-lines) was fairly similar to the manual measurements of average Z-line number per NRVM for FHOD3-depleted NRVMs (3 ± 6 sarcomeres) (**Fig.4-2B**). This discrepancy between Z-line number per NRVM in the presence of NRVM's with high numbers of sarcomeres is consistent with sarcApp's false negative and false positive hits that were qualitatively identified (**Fig.4-1**).

When we compared the Z-line length and sarcomere length measurements that were manually measured in Chapter 2 to those measured by sarcApp, there was noticeably more agreement (**Fig.4-3A,B**). We observed that FHOD3L wild-type rescued NRVMs have sarcomere lengths of 1.48 ± 0.36 µm when measured by sarcApp, but 1.72 ± 0.18 µm when manually measured, showing an ~15% difference between measurement methods (**Fig.4-3A**). Conversely, we found that FHOD3L-depleted NRVMs have sarcomere lengths of 1.50 ± 0.31 μm when measured by sarcApp and 1.46 ± 0.37 μm when manually measured, showing a much better agreement (**Fig.4-3A**). Finally, for manual Z-line length measurements we found FHOD3L-depleted NRVMs had 1.38 ± 0.46 μm Z-lines and FHOD3L wild-type-rescued NRVMs had 1.70 ± 0.46 μm (**Fig.2-7G**). In stark contrast to this, we found sarcApp to measure 2.28 ± 0.32 μm Z-lines in FHOD3L-depleted NRVMs and 2.29 ± 0.30 μm Z-lines in FHOD3L wild-type-rescued NRVMs, resulting in loss of the observed trend between these two conditions compared to the manual measurement method, in addition to a 25-40% deviation between these methods (**Fig.4-3B**). Therefore, sarcApp quantification results in notable deviations from the manual measurements of sarcomeres made in Chapter 2, likely due to the false negative and false positive rate of sarcApp.

**Figure 4-3** – *Sarcomere metrics show no difference between FHOD3 knockdown and wild-type rescue via sarcApp.*

(**A**) Quantification of average sarcomere length per NRVM by sarcApp for mock rescued and wild-type-rescued NRVMs. (Mock: n= 124;WT: n=106;mean ± SD; 1 biological replicate each.) (**B**) Quantification of average Z-Line length per NRVM by sarcApp similar to (**A**). (Mock: n= 124;WT: n=106;mean ± SD; 1 biological replicate each.)

We reasoned from this discrepancy in measurements that either the spatial resolution of our images required optimization or the yoU-Net deep-learning model for binarization is not sufficient for NRVMs. To improve the spatial resolution we tried using a spinning disk confocal microscope at different magnifications as that was specifically used by the Burnette lab (Neininger-Castro et al., 2023). Qualitatively, we found that at 40x, 63x, and 100x magnification on the spinning disk that there were still false positives and false negatives, although noticeably fewer false negatives were observed at 100x magnification than the lower magnification images tested (**Fig.4-4, Fig.4-5**). By looking more closely at these images, we concluded that the spinning disk laser was

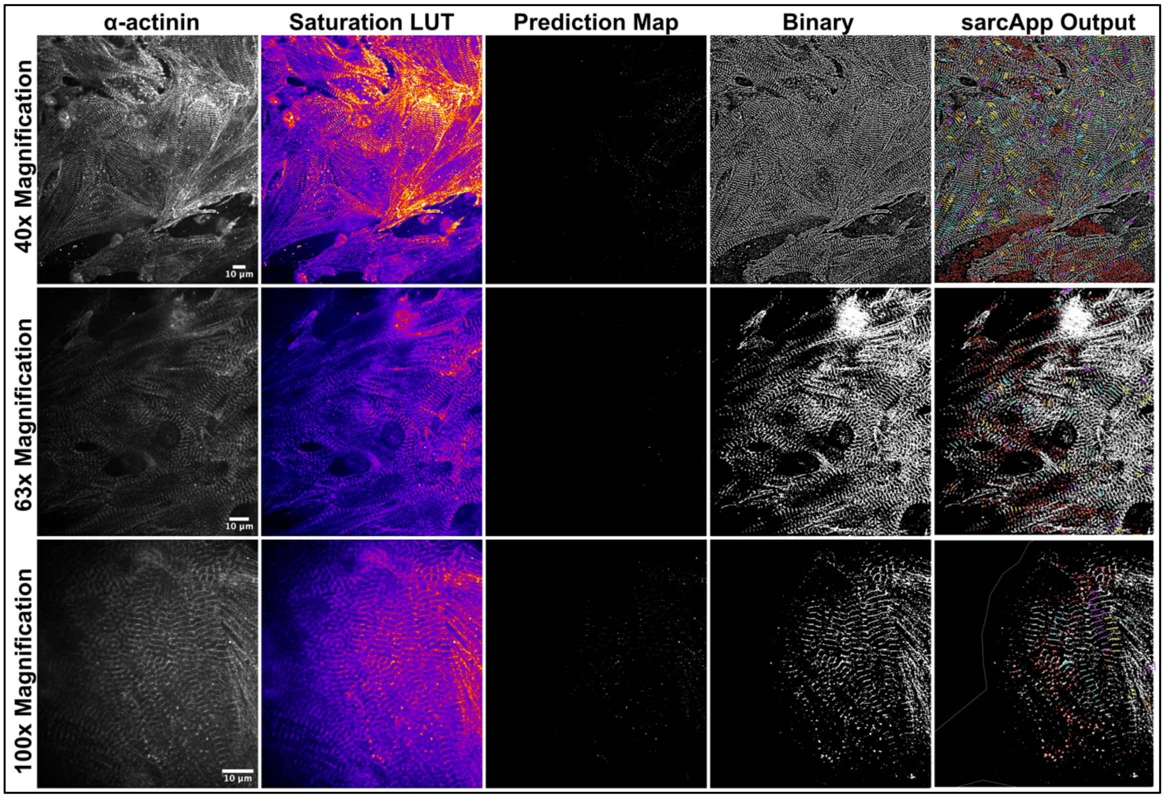

**Figure 4-4** – *SarcApp accuracy slightly improves with higher spatial resolution for FHOD3L wild-type-rescued NRVMs.*

Spinning disk confocal micrographs of FHOD3L wild-type-rescued NRVMs at 40x (top), 63x (middle), and 100x magnification (bottom). The second column shows oversaturated pixels in red. The sarcApp output identifies Z-lines by myofibrils in different colors and Z-bodies (red circles).

misaligned, leading to uneven fluorescence intensity across each of the images taken (**Fig.4-4, Fig.4-5**).

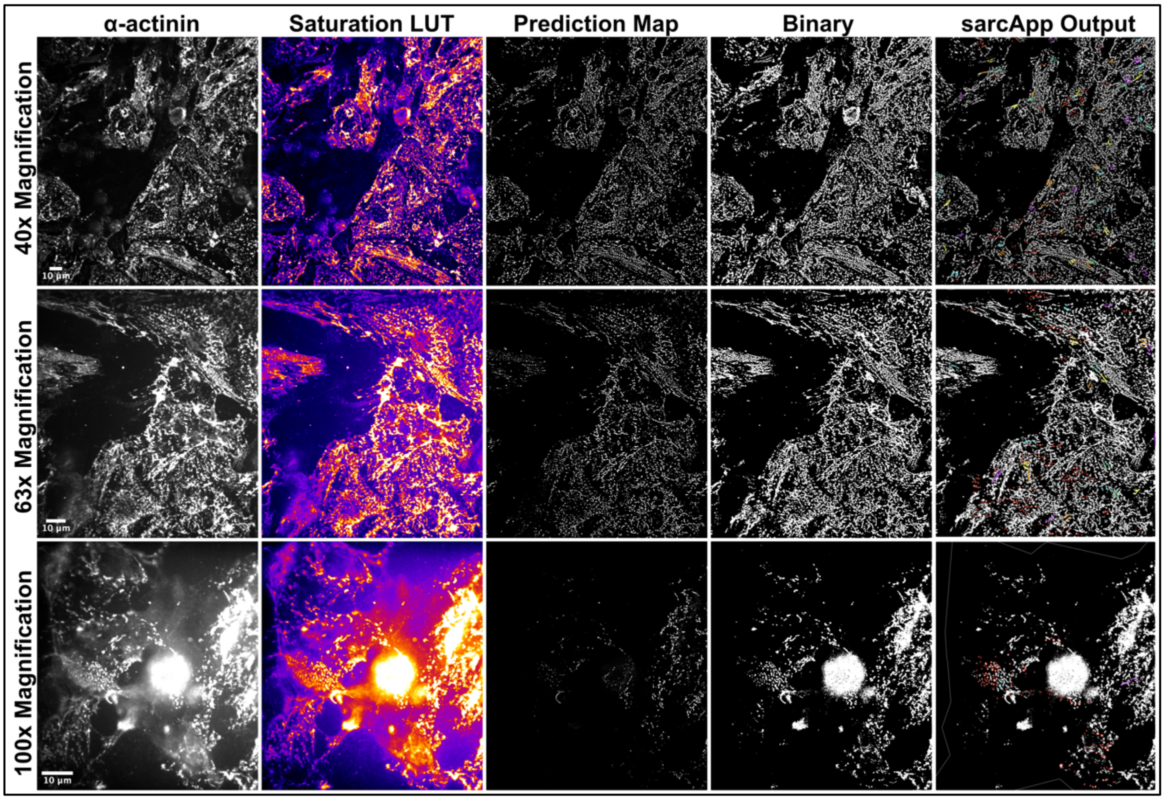

**Figure 4-5** – *yoU-Net does not binarize α-actinin puncta well in FHOD3-depleted NRVMs.*

Spinning disk confocal micrographs of FHOD3-depleted NRVMs at 40x (top), 63x (middle), and 100x magnification (bottom). The second column shows oversaturated pixels in red. The sarcApp output identifies Z-lines by myofibrils in different colors and Z-bodies (red circles).

Although we did not acquire more images on the spinning disk confocal after its laser was properly realigned, we next asked if the post-processing method of image deconvolution to artificially remove background will improve sarcApp's quantification accuracy. To do this, we acquired images on the THUNDER widefield microscope that has built-in capabilities to remove out of focus light with the proprietary THUNDER processing method in addition to deconvolution. As a result, we found that taking Z-stacks and generating maximum intensity projections for subsequent THUNDER and deconvolution post-processing resulted in notable background reduction compared to the original projection (**Fig.4-6**). After acquiring much cleaner images of NRVMs, we then wanted to run sarcApp to evaluate its accuracy with these deconvoluted images. As a result, we observed minimal improvements to the false negative and false positive rate by sarcApp (**Fig.4-7**). Further, we observed that there seems to be some computational limit in sarcApp in identifying Z-bodies in which the program identifies many Z-bodies in an "hourglass-shaped" fashion, and then times out for the rest of the image, although this does not happen when Cellpose segmentations are used (**Fig.4-7**). Moreover, using a demo of a licensed deconvolution program called Microvolution that is

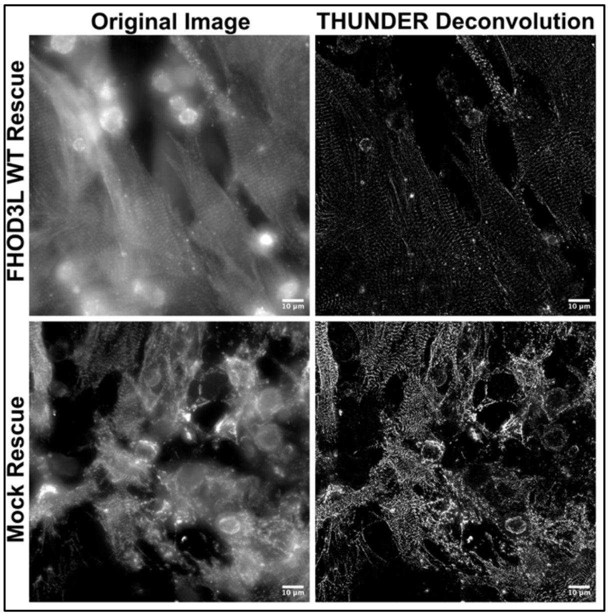

**Figure 4-6** – *THUNDER deconvolution greatly reduces background fluorescence in NRVMs.*

Max intensity projections of 21 Z-slices for FHOD3L wild-type-rescued (top) and mock rescued-NRVMs (bottom).

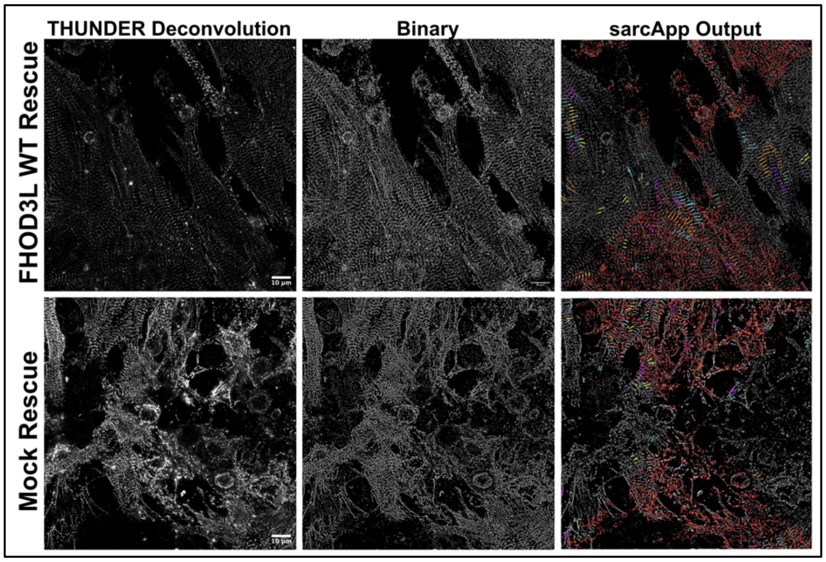

**Figure 4-7** – *THUNDER deconvolution negligibly improves sarcApp false negative rate.*

yoU-Net binarized images from Fig.4-6 input into sarcApp. The sarcApp output identifies Z-lines by myofibrils in different colors and Z-bodies (red circles). The sarcApp output identifies Z-lines by myofibrils in different colors and Z-bodies (red circles).

used by the Burnette lab, we found notable improvements to image resolution, thus improving the accuracy of sarcApp (**Fig.4-8**). Therefore, image deconvolution by Microvolution improves accuracy of the sarcApp output more than THUNDER and deconvolution post-processing from widefield images.

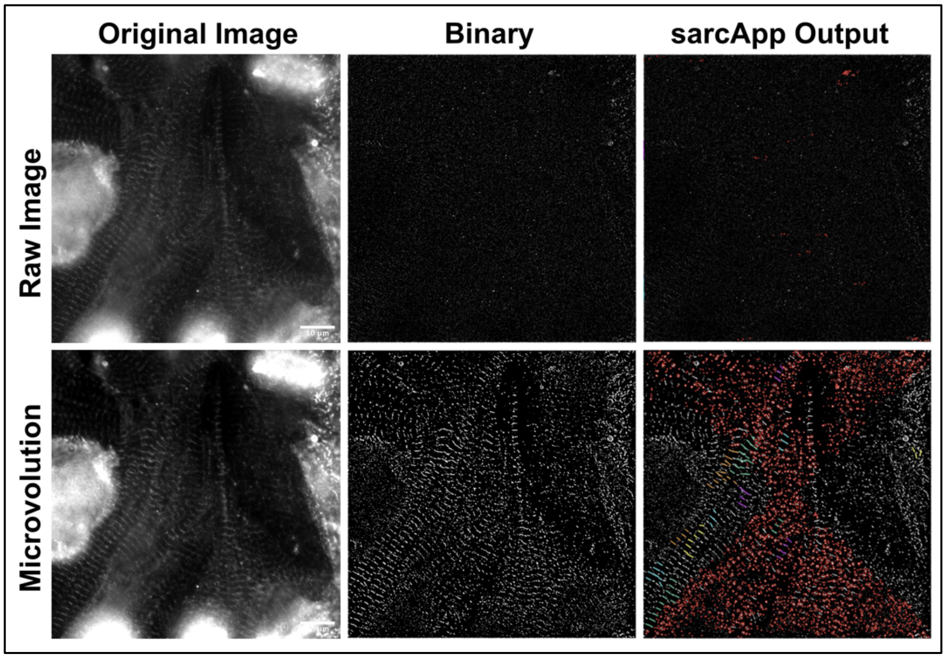

**Figure 4-8** – *Microvolution deconvolution noticeably improves sarcApp accuracy.*

100x magnification widefield micrographs acquired on the THUNDER microscope of FHOD3L wild-type-rescued NRVMs with (bottom) or without Microvolution deconvolution (top). The sarcApp output identifies Z-lines by myofibrils in different colors and Z-bodies (red circles).

## Discussion

### *Critical assessment of sarcApp*

In this chapter, we critically evaluated the accuracy of sarcApp's automated and unbiased identification and measurements of Z-bodies and Z-lines in NRVMs for the first time as it was exclusively used previously with hiCMs (Neininger-Castro et al., 2023). The potential amount of analysis time that can be saved by using sarcApp in lieu of single-blinded, manual analysis of sarcomeres is a very enticing concept that unfortunately is restricted to extremely high-quality images of cardiomyocytes. This lower image quality may be partially due to the increase in autofluorescence as cardiomyocytes become more mature, which can make background correction and deconvolution even more difficult in NRVMs or adult cardiomyocytes compared to embryonic cardiomyocytes, such as the hiCMs (Chorvat et al., 2005; Larcher et al., 2018). More importantly, the Burnette lab utilizes a replating strategy with the proliferative hiCMs where they trypsinize the cells after they are already seeded the first time to then observe sarcomere reformation over time (Fenix et al., 2018). This same protocol cannot be performed with NRVMs or adult cardiomyocytes as they cannot endure trypsinization and replating.

Given that we wanted to observe functional contractility of the NRVMs after FHOD3L rescue experiments in Chapter 2, we needed to seed the wells at sufficient confluency to allow for proper calcium signaling between the cardiomyocytes, thus leading to the need for Cellpose segmentation. Further, replating the hiCMs at low confluency likely allows for more cell spreading than more confluent NRVMs, which would possibly contribute to more sarcomeres being partially in multiple Z planes in

NRVMs, thus making proper measurements of myofibrils more difficult without 3D reconstructions. Despite this, the licensed Microvolution software allowed for notable improvements to the identification of Z-lines by sarcApp when compared to the same non-processed, single plane widefield image (**Fig.4-8**). Z-stacks of NRVMs stained for $\alpha$-actinin can be input into the Microvolution program for likely much better results compared to single plane images.

We tested sarcApp's accuracy with three different microscopes and seven different objective lenses. Given that the Burnette lab used a 100x magnification objective lens on a spinning disk confocal, we reasoned that a similar setup could be optimal. We found that our spinning disk confocal had laser alignment issues and a portion of sarcApp's false negative rate likely arose from that and can easily be resolved, at least in part, with a properly aligned laser on that same system. Moreover, with Leica's newly developed AI-based image analysis software, Aivia, another deep learning model could potentially be trained for NRVMs, specifically, despite binarization by the yoU-Net of the images of NRVMs working well. Additionally, Aivia can identify Z-lines and measure their lengths and subsequently, the sarcomere lengths in a semi-autonomous manner. In the last decade, there has been an exponential growth of scientific advancements in the field of AI and there are sure to be more significant improvements for machine learning and AI in the future that can further enhance the capabilities of sarcApp.

To currently begin to improve sarcApp to become more broadly useful across cardiomyocytes at various stages of development and confluency, we wrote a Python-based code that incorporates single-cell segmentations from Cellpose in place of sarcApp’s default edge detection script (see Methods for GitHub link). This newly written code, in addition to some simple imageJ macros that were written, will help improve the throughput rate for sarcomere analysis of cardiomyocytes by sarcApp. We hope that the cardiovascular community will begin to build off the foundation that sarcApp established with the goal of making this program more widely accessible for a range of image qualities and developmental stages of cardiomyocytes.

## Materials and Methods

### *Adenoviral generation, purification, and infection*

Adenoviruses purchased and generated as described in Chapter 2.

### *Neonatal rat ventricular myocyte seeding, siRNA knockdown, and rescue*

Rescue experiments in NRVMs performed as described in Chapter 2.

### *Immunofluorescence and image analysis*

NRVMs were fixed and stained as described in Chapter 2. 16-bit images in Fig.4-1 were acquired on an AXIO Imager.D1 fluorescence phase contrast microscope (Zeiss) using a Plan-Apochromat oil DIC M27 63x (1.4 NA) objective lens (Zeiss), while Fig.4-2 16-bit images were acquired on an EC Plan-Neofluar 40x M27 (0.75 NA) objective lens (Zeiss) both with an AxioCam MRm camera (Zeiss). 16-bit images in Fig.4-4 and Fig.4-5 were acquired on a Leica SD AF Spinning Disc system using a HCX PL APO 40x (0.85 NA) oil objective lens (Leica), HC PL APO 63x (1.4 NA) oil objective lens (Leica), and a HC PL APO 100x (1.4 NA) objective lens (Leica) with an ORCA-Flash4.0 LT C11440 camera (Hamamatsu). 16-bit images in Fig.4-6 were acquired on a Leica DMI8 THUNDER system using a HCX PL FLUOTAR L 63x (0.7 NA) oil objective lens, while images in Fig.4-7 were acquired with a HC PL APO 100x (1.47 NA) oil objective lens both with an ORCA-Flash4.0 V3 C13440 camera (Hamamatsu). Fig.4-8 used a demo of Microvolution (BioVision Technologies, Inc.) for deconvolution of images. Both the default version of sarcApp and our own modified version of sarcApp were used in this chapter. The modified sarcApp code can be found as a branch to the original sarcApp code on GitHub:

https://github.com/davalencia0914/sarcApp_Cellpose_Merge

## References

Chorvat, D., Kirchnerova, J., Cagalinec, M., Smolka, J., Mateasik, A., & Chorvatova, A. (2005). Spectral Unmixing of Flavin Autofluorescence Components in Cardiac Myocytes. *Biophysical Journal*, *89*(6), L55–L57. https://doi.org/10.1529/biophysj.105.073866

Fenix, A. M., Neininger, A. C., Taneja, N., Hyde, K., Visetsouk, M. R., Garde, R. J., & Burnette, D. T. (2018). Muscle-specific stress fibers give rise to sarcomeres in cardiomyocytes. *eLife*, *7*, e42144. https://doi.org/10.7554/eLife.42144

Huxley, A. F., & Niedergerke, R. (1954). Structural Changes in Muscle During Contraction: Interference Microscopy of Living Muscle Fibers. *Nature*, *173*(4412), 971–973. https://doi.org/10.1038/173971a0

Huxley, H., & Hanson, J. (1954). Changes in the Cross-Striations of Muscle during Contraction and Stretch and their Structural Interpretation. *Nature*, *173*(4412), 973–976. https://doi.org/10.1038/173973a0

Larcher, V., Kunderfranco, P., Vacchiano, M., Carullo, P., Erreni, M., Salamon, I., Colombo, F. S., Lugli, E., Mazzola, M., Anselmo, A., & Condorelli, G. (2018). An autofluorescence-based method for the isolation of highly purified ventricular cardiomyocytes. *Cardiovascular Research*, *114*(3), 409–416. https://doi.org/10.1093/cvr/cvx239

Littlefield, R., & Fowler, V. M. (2002). Measurement of Thin Filament Lengths by Distributed Deconvolution Analysis of Fluorescence Images. *Biophysical Journal*, *82*(5), 2548–2564. https://doi.org/10.1016/S0006-3495(02)75598-7

Neininger-Castro, A. C., Jr, J. B. H., Sanchez, Z. C., Taneja, N., Fenix, A. M., Moparthi, S., Vassilopoulos, S., & Burnette, D. T. (2023). Independent regulation of Z-lines and M-lines during sarcomere assembly in cardiac myocytes revealed by the automatic image analysis software sarcApp. *eLife*, *12*. https://doi.org/10.7554/eLife.87065.2

Palmer, B. M., Swank, D. M., Miller, M. S., Tanner, B. C. W., Meyer, M., & LeWinter, M. M. (2020). Enhancing diastolic function by strain-dependent detachment of cardiac myosin crossbridges. *Journal of General Physiology*, *152*(4), e201912484. https://doi.org/10.1085/jgp.201912484

Pirani, A., Vinogradova, M. V., Curmi, P. M. G., King, W. A., Fletterick, R. J., Craig, R., Tobacman, L. S., Xu, C., Hatch, V., & Lehman, W. (2006). An Atomic Model of the Thin Filament in the Relaxed and $Ca^{2+}$-Activated States. *Journal of Molecular Biology*, *357*(3), 707–717. https://doi.org/10.1016/j.jmb.2005.12.050

Stringer, C., Wang, T., Michaelos, M., & Pachitariu, M. (2021). Cellpose: A generalist algorithm for cellular segmentation. *Nature Methods*, *18*(1), Article 1. https://doi.org/10.1038/s41592-020-01018-x

Toepfer, C. N., Sharma, A., Cicconet, M., Garfinkel, A. C., Mücke, M., Neyazi, M., Willcox, J. A. L., Agarwal, R., Schmid, M., Rao, J., Ewoldt, J., Pourquié, O., Chopra, A., Chen, C. S., Seidman, J. G., & Seidman, C. E. (2019). SarcTrack. *Circulation Research*, *124*(8), 1172–1183. https://doi.org/10.1161/CIRCRESAHA.118.314505

# Chapter 5: FHOD3 in Cardiomyocytes

## Discussion

The mammalian formin FHOD3L has been known to be important for sarcomere formation for over a decade (Taniguchi et al., 2009). However, its specific actin assembly activities that contributed to this process were not thoroughly characterized until now (Chapter 2). In Chapter 2, we established through rescue experiments in NRVMs and *in vitro* biochemical actin assembly assays that elongation activity by FHOD3L is necessary for proper sarcomere formation. This rescue experiment methodology in NRVMs has the potential to answer many other questions that arose throughout this research or remain unanswered. Moreover, the role of PRMT7-mediated methylation in the C-terminal DAD of FHOD3L in cardiomyocytes remains unknown despite implications for PRMT7 in cardiac hypertrophy and sex-specific cardiomyopathy (Chapter 3) (Ahn et al., 2022, 2024). Insights into these phenomena in cardiomyocytes can be accelerated with improvements to AI-based programs that quantify sarcomere metrics, such as sarcApp (Chapter 4).

We tested two different FHOD3L mutants implicated in HCM: R1386Q in the FH2 domain and R637P in the N-terminal putative coiled-coil domain, which is a mutational hotspot (Chapter 2) (Ochoa et al., 2018). We were able to characterize the actin assembly activity of FHOD3L-CT R1386Q, but unable to assess how the R637P mutation affects FHOD3L activity due to purification difficulties of a longer N-terminal construct (Chapter 2). The likely degradation of FHOD3L R637P in NRVMs is consistent with protein instability of these longer, coiled-coil domain-containing N-terminal constructs *in vitro* (Chapter 2). In addition to these two mutations, there are a plethora of other FHOD3L mutations implicated in HCM that remain to be biochemically characterized (**Fig.1-3**) (Ochoa et al., 2018). Further, more physiologically relevant promoters can be used in the rescue experiments in NRVMs for these HCM mutants, such as ß-MHC promoters instead of general CMV promoters, which can be inserted into adenoviral vectors via helper-dependent adenovirus cloning methods (Zhang et al., 2023). To improve the physiological relevance of these experiments, each of these HCM-causative FHOD3L mutants can be conditionally knocked in using the Cre/lox system in mice (Song & Palmiter, 2018). Specifically, a heterozygous state of these HCM mutants can be induced at the neonatal stage and driven by a cardiac-specific $\alpha$-MHC promoter, which is more typical of what would be observed in patients (Garfinkel et al., 2018; Ochoa et al., 2018).

Most of the work described here focused on FHOD3L at the protein level, but how upstream gene expression of cardiac markers in NRVMs is affected by overexpressing FHOD3L, if at all, remains unclear. The potential mechanism by which this can occur can be indirectly due to sarcomere formation as developed Z-lines are necessary for proper microtubule-based transport of mRNA's in muscle, in addition to subsequent force generation in the presence of FHOD3L above endogenous levels (Denes et al., 2021; Fulton & Alftine, 1997; Mei et al., 2020; Nishimura et al., 2021; Perozo et al., 2002). These hypotheses can be tested in the future via qPCR, FISH, single-cell RNA-sequencing, and ChIP-Seq, among other genomic methods (Denes et al., 2021; Göttgens et al., 2018; Jia et al., 2018). Further, strand-specific RNA-sequencing (ssRNA-seq) can distinguish alternatively spliced mRNA isoforms of FHOD3L and FHOD3S, allowing us to better understand the relative levels of each isoform in cardiomyocytes (Zhao et al., 2015).

Substrates are still being discovered and characterized for the novel PRMT7, which is now known to methylate human histone H2B, FHOD1, and FHOD3 *in vitro*. Despite extensive characterization *in vitro* showing that ROCK1-mediated phosphorylation inhibits PRMT7-mediated methylation of FHOD3 in Chapter 3, the potential interaction for PRMT7 and FHOD3L in cardiomyocytes and the consequence of such interaction is currently unknown. In Chapter 3, we began to establish a methyl mimic to observe the effect of C-terminal methylation, if any, on FHOD3L's autoinhibition ability via pyrene assays in the presence of FHOD3L-NT. Given that methylation does not notably enhance ROCK1-mediated phosphorylation in the DAD of FHOD3L suggests that PRMT7's roles is more complex in regulating FHOD3L in cardiomyocytes, potentially playing a role in protein stability. Alternatively, FHOD3L may recognize other methylated proteins or be able to be recognized by other cardiac-specific proteins in cardiomyocytes when methylated by PRMT7, similar to what was recently observed for FMNL formins (Casanova et al., 2024).

Overall, many cell types require higher-order actin structures for proper cellular functions, such as podosomes, filopodia, or sarcomeres, among many others that are regulated by numerous actin-binding proteins (Ahmed et al., 2022; Jaiswal et al., 2013; Masters & Buss, 2017; Sit et al., 2020; Murphy & Courtneidge, 2011; Taniguchi et al., 2009). The significant insights we have found for sarcomere formation by FHOD3L will continue to inform us how other formins and actin nucleators help build these higher-order structures in cells. Ongoing research that interrogates how FHOD3L mechanistically assembles sarcomeres with the help of other actin-binding proteins in proximity will offer valuable insights across cardiovascular biology.

## References

Ahmed, R. E., Tokuyama, T., Anzai, T., Chanthra, N., & Uosaki, H. (2022). Sarcomere maturation: Function acquisition, molecular mechanism, and interplay with other organelles. *Philosophical Transactions of the Royal Society B: Biological Sciences*, *377*(1864). https://doi.org/10.1098/rstb.2021.0325

Ahn, B.-Y., Jeong, M.-H., Pyun, J.-H., Jeong, H.-J., Vuong, T. A., Bae, J.-H., An, S., Kim, S. W., Kim, Y. K., Ryu, D., Kim, H.-J., Cho, H., Bae, G.-U., & Kang, J.-S. (2022). PRMT7 ablation in cardiomyocytes causes cardiac hypertrophy and fibrosis through β-catenin dysregulation. *Cellular and Molecular Life Sciences*, *79*(2), 99. https://doi.org/10.1007/s00018-021-04097-x

Ahn, B.-Y., Zhang, Y., Wei, S., Jeong, Y., Park, D.-H., Lee, S.-J., Leem, Y.-E., & Kang, J.-S. (2024). Prmt7 regulates the JAK/STAT/Socs3 signaling pathway in postmenopausal cardiomyopathy. *Experimental & Molecular Medicine*, *56*(3), 711–720. https://doi.org/10.1038/s12276-024-01193-3

Casanova, A. G., Roth, G. S., Hausmann, S., Lu, X., Bischoff, L. J. M., Froeliger, E. M., Belmudes, L., Bourova-Flin, E., Flores, N. M., Benitez, A. M., Chasan, T., Caporicci, M., Vayr, J., Blanchet, S., Ielasi, F., Rousseaux, S., Hainaut, P., Gozani, O., Le Romancer, M., … Reynoird, N. (2024). Cytoskeleton remodeling induced by SMYD2 methyltransferase drives breast cancer metastasis. *Cell Discovery*, *10*(1), 1–22. https://doi.org/10.1038/s41421-023-00644-x

Denes, L. T., Kelley, C. P., & Wang, E. T. (2021). Microtubule-based transport is essential to distribute RNA and nascent protein in skeletal muscle. *Nature Communications*, *12*(1), 6079. https://doi.org/10.1038/s41467-021-26383-9

Fulton, A. B., & Alftine, C. (1997). Organization of protein and mRNA for titin and other myofibril components during myofibrillogenesis in cultured chicken skeletal muscle. *Cell Structure and Function*, *22*(1), 51–58. https://doi.org/10.1247/csf.22.51

Garfinkel, A. C., Seidman, J. G., & Seidman, C. E. (2018). Genetic Pathogenesis of Hypertrophic and Dilated Cardiomyopathy. *Heart Failure Clinics*, *14*(2), 139–146. https://doi.org/10.1016/j.hfc.2017.12.004

Göttgens, B., Paulissen, C., Dubois, C., Wang, X., Gargouri, S., Lin, X., Sànchez-Dànes, A., Swedlund, B., Blanpain, C., Kinston, S., Moignard, V., & Lescroart, F. (2018). Defining the earliest step of cardiovascular lineage segregation by single-cell RNA-seq. *Science*, *359*(6380), 1177–1181. https://doi.org/10.1126/science.aao4174

Jaiswal, R., Breitsprecher, D., Collins, A., Corrêa, I. R., Xu, M. Q., & Goode, B. L. (2013). The formin daam1 and fascin directly collaborate to promote filopodia formation. *Current Biology*, *23*(14), 1373–1379. https://doi.org/10.1016/j.cub.2013.06.013

Jia, G., Preussner, J., Chen, X., Guenther, S., Yuan, X., Yekelchyk, M., Kuenne, C., Looso, M., Zhou, Y., Teichmann, S., & Braun, T. (2018). Single cell RNA-seq and ATAC-seq analysis of cardiac progenitor cell transition states and lineage settlement. *Nature Communications*, *9*(1). https://doi.org/10.1038/s41467-018-07307-6

Masters, T. A., & Buss, F. (2017). Filopodia formation and endosome clustering induced by mutant plus-end–directed myosin VI. *Proceedings of the National Academy of Sciences*, *114*(7), 1595–1600. https://doi.org/10.1073/pnas.1616941114

Sit, B., Feng, Z., Xanthis, I., Marhuenda, E., Zingaro, S., Shanahan, C., Jones, G. E., Yu, C., & Iskratsch, T. (2020). Matrix stiffness and blood pressure together regulate vascular smooth muscle cell phenotype switching and cofilin dependent podosome formation. *Biorxiv*. https://doi.org/10.1101/2020.12.27.424498

Mei, L., de los Reyes, S. E., Reynolds, M. J., Leicher, R., Liu, S., & Alushin, G. M. (2020). Molecular mechanism for direct actin force-sensing by α-catenin. *eLife*, *9*, 1–30. https://doi.org/10.7554/ELIFE.62514

Murphy, D. A., & Courtneidge, S. A. (2011). The “ins” and “outs” of podosomes and invadopodia: Characteristics, formation and function. *Nature Reviews. Molecular Cell Biology*, *12*(7), 413–426. https://doi.org/10.1038/nrm3141

Nishimura, Y., Shi, S., Li, Q., Bershadsky, A. D., & Viasnoff, V. (2021). Crosstalk between myosin II and formin functions in the regulation of force generation and actomyosin dynamics in stress fibers. *Cells & Development*, 203736. https://doi.org/10.1016/j.cdev.2021.203736

Ochoa, J. P., Sabater-Molina, M., Garcia-Pinilla, J. M., Mogensen, J., Restrepo-Cordoba, A., Palomino-Doza, J., Villacorta, E., Martinez-Moreno, M., Ramos-Maqueda, J., Zorio, E., Peña-Peña, M. L., García-Granja, P. E., Rodríguez-Palomares, J. F., Cárdenas-Reyes, I. J., de la Torre-Carpente, M. M., Bautista-Pavés, A., Akhtar, M. M., Cicerchia, M. N., Bilbao-Quesada, R., … Monserrat, L. (2018). Formin Homology 2 Domain Containing 3 (FHOD3) Is a Genetic Basis for Hypertrophic Cardiomyopathy. *Journal of the American College of Cardiology*, 72(20), 2457-2467. https://doi.org/10.1016/j.jacc.2018.10.001

Perozo, E., Kloda, A., Cortes, D. M., & Martinac, B. (2002). Physical principles underlying the transduction of bilayer deformation forces during mechanosensitive channel gating. *Nature Structural Biology*, *9*(9), 696–703. https://doi.org/10.1038/nsb827

Song, A. J., & Palmiter, R. D. (2018). Detecting and Avoiding Problems When Using the Cre/lox System. *Trends in Genetics : TIG*, *34*(5), 333–340. https://doi.org/10.1016/j.tig.2017.12.008

Taniguchi, K., Takeya, R., Suetsugu, S., Kan-o, M., Narusawa, M., Shiose, A., Tominaga, R., & Sumimoto, H. (2009). Mammalian formin Fhod3 regulates actin assembly and sarcomere organization in striated muscles. *Journal of Biological Chemistry*, *284*(43), 29873–29881. https://doi.org/10.1074/jbc.M109.059303

Zhang, H., Wang, H., An, Y., & Chen, Z. (2023). Construction and application of adenoviral vectors. *Molecular Therapy. Nucleic Acids*, *34*, 102027. https://doi.org/10.1016/j.omtn.2023.09.004

Zhao, S., Zhang, Y., Gordon, W., Quan, J., Xi, H., Du, S., von Schack, D., & Zhang, B. (2015). Comparison of stranded and non-stranded RNA-seq transcriptome profiling and investigation of gene overlap. *BMC Genomics*, *16*(1), 675. https://doi.org/10.1186/s12864-015-1876-7